SINGLE-MOLECULE DIFFUSION MEASUREMENTS FOR MATERIAL CHARACTERIZATION IN ONE-DIMENSIONAL NANOSTRUCTURED POLYMER FILMS

by

KHANH-HOA TRAN-BA

B.S., Justus-Liebig University Giessen, 2008

AN ABSTRACT OF A DISSERTATION

submitted in partial fulfillment of the requirements for the degree

DOCTOR OF PHILOSOPHY

Department of Chemistry
College of Arts and Sciences

KANSAS STATE UNIVERSITY
Manhattan, Kansas

2015

Abstract

This dissertation describes single-molecule tracking (SMT) measurements for the quantitative characterization of one-dimensional (1D) nanostructures in 200 nm-thick surfactant-templated mesoporous silica (STMS) and cylinder-forming polystyrene-poly(ethylene oxide) diblock copolymer (CF-PS-*b*-PEO) films with a μm-scale thickness. SMT is advantageous for the characterization of nanomaterials over conventional methods because it permits the simultaneous and quantitative assessment of the nanoscale and microscale morphologies, and mass-transport properties of the materials with a high nanometer-scale resolution under ambient conditions. It offers a unique means for the assessment and evaluation of the μm-scale nanostructure alignment in polymer films induced by vertical spin-coating (for STMS films), directional solution flow and solvent-vapor penetration (SVP) methods (both for CF-PS-*b*-PEO films), highly crucial for many potential technological applications using the materials. Through this work, we have identified suitable sample preparation conditions (e.g. solvent, temperature or solution flow rate) for obtaining highly-ordered mesoporous and microdomain structures over a long-range (> 5 μm). For the quantitative assessment of the 1D SMT data, orthogonal regression analysis was employed, providing assessment of the in-plane orientation and size of individual nanostructures with nanometer-scale precision. The analysis of the 1D trajectory data allowed the radius (*ca.* 11 nm) of cylindrical PEO microdomains to be estimated, yielding results consistent with the AFM results (*ca.* 14 nm). The distribution of the trajectory angles offered the estimation of the average orientation and order of the nanostructures in domains/grains for a μm-wide region of the polymer films, revealing the higher efficiency of SVP in the nanostructure alignment as compared to the spin coating and solution flow approaches. Systematic SMT measurements across the film depth and along lateral mm-scale distances afforded valuable insights into the shear- and solvent-evaporation-based alignment mechanisms induced by solution flow and SVP/spin coating approaches, respectively. Fluorescence recovery after photobleaching (FRAP) measurements in a SVP-aligned CF-PS-*b*-PEO film permitted the longer-range mass-transport properties to be probed, reflecting the effective continuity of the aligned cylindrical nanostructures over > 100 μm in length. In this dissertation, FRAP and more importantly SMT methods have provided a unique and useful means for the in-depth characterization of morphology and mass-transport characteristics in thin polymer films under ambient conditions, in confined spaces, and with a nanometer-scale resolution.

SINGLE-MOLECULE DIFFUSION MEASUREMENTS
FOR MATERIAL CHARACTERIZATION
IN ONE-DIMENSIONAL NANOSTRUCTURED POLYMER FILMS

by

KHANH-HOA TRAN-BA

B.S., Justus-Liebig University Giessen, 2008

A DISSERTATION

submitted in partial fulfillment of the requirements for the degree

DOCTOR OF PHILOSOPHY

Department of Chemistry
College of Arts and Sciences

KANSAS STATE UNIVERSITY
Manhattan, Kansas

2015

Approved by:

Major Professor
Dr. Takashi Ito

Copyright

Abstract

This dissertation describes single-molecule tracking (SMT) measurements for the quantitative characterization of one-dimensional (1D) nanostructures in 200 nm-thick surfactant-templated mesoporous silica (STMS) and cylinder-forming polystyrene-poly(ethylene oxide) diblock copolymer (CF-PS-*b*-PEO) films with a μm-scale thickness. SMT is advantageous for the characterization of nanomaterials over conventional methods because it permits the simultaneous and quantitative assessment of the nanoscale and microscale morphologies, and mass-transport properties of the materials with a high nanometer-scale resolution under ambient conditions. It offers a unique means for the assessment and evaluation of the μm-scale nanostructure alignment in polymer films induced by vertical spin-coating (for STMS films), directional solution flow and solvent-vapor penetration (SVP) methods (both for CF-PS-*b*-PEO films), highly crucial for many potential technological applications using the materials. Through this work, we have identified suitable sample preparation conditions (e.g. solvent, temperature or solution flow rate) for obtaining highly-ordered mesoporous and microdomain structures over a long-range (> 5 μm). For the quantitative assessment of the 1D SMT data, orthogonal regression analysis was employed, providing assessment of the in-plane orientation and size of individual nanostructures with nanometer-scale precision. The analysis of the 1D trajectory data allowed the radius (*ca.* 11 nm) of cylindrical PEO microdomains to be estimated, yielding results consistent with the AFM results (*ca.* 14 nm). The distribution of the trajectory angles offered the estimation of the average orientation and order of the nanostructures in domains/grains for a μm-wide region of the polymer films, revealing the higher efficiency of SVP in the nanostructure alignment as compared to the spin coating and solution flow approaches. Systematic SMT measurements across the film depth and along lateral mm-scale distances afforded valuable insights into the shear- and solvent-evaporation-based alignment mechanisms induced by solution flow and SVP/spin coating approaches, respectively. Fluorescence recovery after photobleaching (FRAP) measurements in a SVP-aligned CF-PS-*b*-PEO film permitted the longer-range mass-transport properties to be probed, reflecting the effective continuity of the aligned cylindrical nanostructures over > 100 μm in length. In this dissertation, FRAP and more importantly SMT methods have provided a unique and useful means for the in-depth characterization of morphology and mass-transport characteristics in thin polymer films under ambient conditions, in confined spaces, and with a nanometer-scale resolution.

Table of Contents

List of Figures

List of Tables

Acknowledgements

First of all, I would like to thank my major professor and research advisor Dr. Takashi Ito for his constant guidance, valuable suggestions and endless encouragements during the last wonderful and productive seven years as exchange and graduate student at Kansas State University. I highly appreciate the endless hours he spent for revision of my paper drafts, seminar abstracts or written proposals. I am so thankful for having him as a research advisor and for being a member of his multi-cultural research group in the Department of Chemistry at Kansas State University.

I also would like to greatly thank my co-advisor Dr. Dan Higgins for bringing me closer to the exciting field of single molecule spectroscopy and microscopy. Without his great help it would be very difficult for me to make a gradual progress in the experimental research and subsequent data analysis using computer programs and macros developed and written by him.

I am also very blessed to have such a wonderful PhD committee consisting of Dr. Chris Sorenson, Dr. Christine Aikens and Dr. Paul Smith. Thank you all for being a member of my committee at the preliminary examinations and PhD defense. A special thank also goes to Dr. Sorensen for teaching me dynamic light scattering and for allowing me doing the experiment in his laboratory at the Department of Physics. Dr. Paul Smith's willingness to serve as a committee member at my defense upon a short notice is also greatly appreciated. I apologize at Dr. Aikens for not be able to set my defense earlier so she could have been in my committee. I also acknowledge Dr. Peter Pfromm for his services as a chair at my PhD defense and examination.

A special thank also goes to several current and past students of the Higgins and Ito group: Dr. Tom Everett, Kevin Robben, Seok-Chan Park and Dr. Shaida Ibrahim. Dr. Everett is acknowledged for teaching me how to use the confocal and widefield fluorescence microscope in the beginning of graduate school career. Without him, I could not have made such a fast and continuous progress in the STMS project. Kevin Robben is also thanked for providing the TPG analysis routine for the analysis of the 1D SMT data. My friend Seok-Chan Park is thanked for his help on the analysis of the SMT data using Igor or Matlab. I also appreciate his time spending on discussing interesting research and other daily topics. Dr. Shaida Ibrahim is greatly thanked for her help and teaching on the conductivity and fluorescence experiments using the phase-separated BCPs.

I also acknowledge all other current and past members of the Ito research group I have met and worked with: Dr. Yongxin Li, Dr. Nelunie Perera, Dr. Feng Li, Dr. Bipin Pandey, Chrishani De Silva, Dol-Raj Sapkota, Govinda Ghimire, Herman Coceancigh and Zeinab Harandizadeh. I have learnt a lot from you as a scientist and special individual. It was also fun to have you guys around as friendly labmates. I also recognize undergraduate student researchers who have worked with and for me such as Jason Finley, Freya Bunga and Chris Cox. Your help and contributions to the experiments and the outcome are greatly appreciated.

I also express my deepest gratitude at the faculty and staff of the Department of Chemistry at Kansas State University. I am very thankful your support and assistance from the beginning of my graduate school career. In particular, Jim Hodgson and Ron Jackson are thanked for providing the glass substrates and film-sandwiching equipment, respectively. I also greatly appreciate Dr. John Desper's and Dr. Chris Culbertson's assistance with the X-ray diffraction (XRD) and profilometry measurements, respectively. I also acknowledge the funding societies, councils and agencies for providing travel funding and stipends for the last five years as graduate research assistant: Graduate Student Council at Kansas State University, College of Arts and Sciences, Phi Lambda Upsilon, Department of Chemistry and Department of Energy.

Last but not least, I thank my wonderful family for their patience, understanding and encouragement during the entire PhD program. I'm really blessed for having them in here and there. Without their constant support, Graduate School would not be such an exciting and learning experience!

Dedication

To my loving wife Thanh-Hien, my caring brother Nam-Hai and especially my proud parents Hung & Hoa.

Acronyms and Definitions

1D/2D/3D	One/Two/Three dimensional
AAO	Anodic aluminum oxide
AFM	Atomic force microscopy
BCP	Block copolymer
CTAB	Cetyltrimethylammonium bromine
FRAP	Fluorescence recovery after photobleaching
NMR	Nuclear magnetic resonance
CF-PS-*b*-PEO	Cylinder-forming polystyrene-poly(ethylene oxide) diblock copolymer
SAM	Self-assembled monolayers
SAXS	Small angle X-ray scattering
SBS	Polystyrene-*b*-poly(ethylene/butylene)-*b*-polystyrene
SEM	Scanning electron microscopy
SMT	Single-molecule tracking
S/N	Signal-to-noise
SPT	Single-particle tracking
STMS	Surfactant-templated mesoporous silica
SVA	Solvent vapor annealing
SVP	Solvent vapor penetration
TEM	Transmission electron microscopy
TIRF	Total internal reflection fluorescence
TPG	Trajectory profile guided
XRD	X-ray diffraction

Chapter 1 - General Introduction[1]

Nanostructured materials are a new class of chemically and physically distinct nanofeatures including pores, domains or molecular assembly with characteristic dimensions of 1-100 nm. These materials can be either prepared from the self-assembly of their atomic or molecular constituents (known as bottom-up) or by down-sizing the existing bulk microstructures (known as top-down).[2] In general, both approaches have offered nanostructured materials with well-defined shape, tunable size and well-controlled morphology by adjusting the experimental conditions during synthesis such as pH, temperature, organic solvent, composition or applied external fields.[3-7] Among the large variety of nanomaterials, cylinder-shaped nanostructures are especially attractive for fundamental research and technological applications because of their simple, cylindrical shape that have lead to interesting and theoretically-predictable materials properties.[2,8] This has been a topic of extensive study for a long time with the goal to integrate these nanomaterials into novel technological applications including chemical sensing[9] and separation,[10] heterogeneous catalysis,[11] drug delivery,[12] energy storage and conversion.[13] However, before any of the goals can be reached; much more effort is needed to fully understand the origin of these unique material properties. One promising route to this goal involves the detailed quantitative characterization of their nanoscale structures and morphologies with a high nm-scale resolution.

Conventionally, the physical properties and morphologies of 1D nanostructured materials have been widely assessed by X-ray scattering (XS), electron microscopy (EM) and atomic force microscopy (AFM).[2,14,15] These methods commonly offer complementary information on the material characteristics from a nanometer- to micrometer length scale and from a nano-to-macrostructure-basis. For example, XS assesses the spatially-averaged information of the nanostructure properties including spacing, orientation and order within a macroscopic (< 1 mm) sample region.[2,8] In contrast, AFM and EM image the high resolution material characteristics for a small microscopic area, allowing the local morphologies including diameter and orientation to be assessed with nanometer-scale precision.[2,8] It is thus quite challenging to discuss longer-range (>10 μm) orientation and organization of the nanostructures from such measurements. XS probes the material characteristics across the sample thickness, whereas AFM and scanning electron microscopy (SEM) provide the topography and structures on the surface, and transmission electron microscopy (TEM) measures the morphology of thin (< 100 nm) slices of the materials.[2,8] The high-resolution images offered by EM reflect solvent-free material properties under ultra-high

vacuum, whereas XS and AFM can probe the material characteristics under various environments, matching conditions employed in real applications. Unfortunately, none of the methods provide information on mass-transport characteristics of the materials. Addressing this limitation, flux measurements have been employed to reveal the overall continuity and accessibility of the cylindrical nanopores materials for small molecule and relatively large proteins, along with the measurement of the overall transport rates and selectivity.[7] Nuclear magnetic resonance (NMR) primarily assess the dynamical information of probe molecules within the nanopores and also provide evidence on the long-range structure orientation.[16] However, the information obtained using these methods commonly reflects the spatially-averaged mass-transport characteristics of many molecules over the entire sample. Neither method can be used to assess the spatial and temporal heterogeneities of material and mass-transport properties within local, μm-scale sample regions, highly essential for their in-depth characterization and understanding.

In recent years, single-molecule tracking (SMT) has provided a unique means to overcome the limitations of conventional methods by monitoring the diffusion dynamics of individual fluorescent probe molecules within 1D nanostructures with a high, nm-scale spatial precision, yielding single-molecule trajectories of confined molecular pathways in the materials.[17,18] The trajectory data have revealed the local mass-transport and material properties of 1D nanostructures .[19] In fact, SMT measurements have provided visual evidence on the local continuity and accessibility of the nanostructures for relatively large molecules, the presence of material heterogeneities (e.g defects) and *qualitative* discussions on the sizes, orientation and order of the organized domains or grains[20] This information has primarily afforded a qualitative picture of the mass-transport and material characteristics of 1D nanostructures. Much more can, however, be learned from such studies, particularly through a detailed quantitative assessment of the single-molecule trajectory data. The results provide clear evidence on the macroscopic alignment of the 1D nanostructures but also quantitative measures of material order, nanostructure sizes and continuity. These parameters are especially crucial for nanomaterials prepared to exhibit such properties.[8,21] An improved characterization of the nanostructures will allow the materials to be engineered, integrated and optimized for future applications in a well-controlled and efficient way.

1.1 Objective and Motivation of the Present Research

In the present dissertation, SMT was used to probe and more importantly quantitatively assess the nanoscale morphology and mass-transport characteristics of 1D nanostructures in

200nm-thick surfactant-templated mesoporous silica (STMS) and cylinder-forming polystyrene-poly(ethylene oxide) (CF-PS-*b*-PEO) films (*ca.* 5-50 μm in thickness). SMT offered a unique means for characterization of the 1D nanostructured materials based on its ability to detect, observe and measure the diffusion dynamics of single molecules within the cylindrical nanopores and microdomains with high spatial (ca. 50 nm) resolution, thus reflecting the properties of confined nanoscale morphologies and structures. Importantly, the single molecule diffusion trajectories afforded a wealth of information from the quantitative assessment of the molecular transport. The information includes the local in-plane orientation and sizes of individual nanostructures, in addition to their order in μm-scale sample regions. The detailed characterization of 1D mesopores and microdomains in STMS[22] and CF-PS-*b*-PEO[1,23,24] films is highly essential for their potential utility and optimization in technological applications. In particular, the long-range nanostructure alignment is crucial and was systematically investigated by SMT in this work. Films containing aligned nanostructures were prepared by vertical spin-coating (STMS), directional solution flow and solvent-vapor-penetration (both for CF-PS-*b*-PEO) approaches as previously demonstrated for similar polymer materials and characterized using conventional methods.[25,26] Here, SMT permitted nanoscale characterization of nanostructures within confined spaces (e.g. sandwiched film between glass substrates) and across the μm-scale film depth, providing insight into the impact of various experimental conditions (e.g. flow rate, polymer concentration, drying temperature and organic solvents) on local morphology in polymer films. The results were used to evaluate the efficacy of different methods for the preparation of organized 1D nanostructures aligned in one direction. The integration of fluorescence recovery after photobleaching (FRAP) into the wide-field fluorescence microscope as employed for SMT measurements permitted the assessment of the longer-range (> 10 μm) nanostructure connectivity, by monitoring the fluorescence recovery kinetics in photobleached regions in the material, reflecting molecular transport in wider μm-scale sample regions. In addition, the setup also afforded valuable complementary information on the mass-transport and material properties from a series of FRAP and SMT measurements in identical sample areas.

1.2 Outline of the Present Dissertation

The present dissertation consists of nine chapters and an appendix. It begins with a general introduction of the present research, along with the research objectives, motivations and an outline

of the dissertation (Chapter 1). Chapter 2 describes 1D nanostructured films of STMS and CF-PS-*b*-PEO, employed in this work, including their synthesis, properties and relevant applications. In Chapter 3, conventional and fluorescence-based methods used for quantitative assessment of the physical properties and mass-transport characteristics of 1D nanostructured materials are introduced. The conventional methods include XS, AFM and SEM/TEM, whereas fluorescence-based methods consist of flux measurements, SMT and FRAP. Chapter 4 describes the orthogonal regression analysis method, representing a useful platform for the quantitative assessment of all 1D SMT data in the present work.[22] The analysis has been initially demonstrated for 1D SMT data recorded in cetyltrimethylammonium bromide (CTAB)-templated mesoporous silica films comprising organized mesopore domains. In Chapter 5 and 6, SMT was used to probe and quantitatively assess the flow- and SVP induced microdomain alignment in CF-PS-*b*-PEO films, respectively.[23,24] Systematic SMT measurement across the film depth and along millimeter-scale lateral distances revealed the effects of shear and solvent-selectivity on the PEO microdomain alignment. Careful analysis of the trajectory data permitted the PEO microdomain radius (*ca.* 11 nm) to be precisely estimated. The result was found to be consistent with the results of AFM measurements. Chapter 7 describes the assessment of the longer-range molecular transport within aligned PEO microdomains using FRAP, providing estimates on the effective microdomain connectivity. Complementary information on the mass-transport characteristics were obtained for a series of FRAP and SMT measurements at identical sample areas of the same film.[1] In Chapter 8, all achievements and results of the present research are summarized. Possible future directions of the present research are also proposed. In Chapter 9, a list of all references cited this dissertation is given. The appendix contains additional information on the data analysis and the original Matlab codes employed for quantitative analysis of the FRAP data.

Chapter 2 - 1D Nanostructured Polymer Materials

This chapter describes a class of novel materials comprising one-dimensional (1D) nanofeatures (pore, domains or molecular assembly). These materials have characteristic dimensions of 1-100 nm and have attracted considerable interest due to their potential utility in technological applications and fundamental research.[27-29] They have been primarily synthesized using well-established top-down and bottom-up.[27]

In the top-down approach, larger bulk materials or microstructures are physically down-sized into smaller features with a nanometer scale characteristics.[30] One typical example includes the fabrication of track-etched polymer membranes in which cylindrical nanopores were prepared by irradiation of the membrane with high-energy fission particles and subsequent chemical etching of the damaged tracks.[3] The locations of the pores are random through the bombardment of particles. Importantly, the pore density is relatively low ($\leq$ 10 pores/μm^2) which often limits the utility of these membranes for technological applications. A nanoporous anodic aluminum oxide (AAO) membrane can also be prepared using the top-down approach from a bulk aluminum block through a selective electrochemical etching process.[4] This process frequently leads to formation of nanopores of better defined shapes and higher density (up to 10^3 pores/μm^2) as compared to the former. As a result, there currently exists a larger number of applications for AAO than for PCTE membranes.[31]

In the bottom-up approach, 1D nanostructures are prepared by the directed self-assembly of constituent atom or molecules to form larger nanoscale structures.[32-35] This approach is quite popular in the material science community for several reasons. First, the fabricated nanostructures commonly exhibit a small number of defects because their final structure is close to the thermodynamic equilibrium structure (as represented by the lowest free energy).[35] Furthermore, this approach is technologically simple and can lead to preparation of technologically-relevant materials at a minimum cost.[5] As a result, a large number of 1D nanostructures have been synthesized using this approach. Relevant materials include self-assembled monolayers (SAMs),[36] phase-separated block copolymers (BCPs)[5,37] and surfactant-templated mesoporous silica (STMS) materials[32] just to name a few. In particular, BCPs and STMS are attractive for many science and engineering disciplines because they commonly offer unique and useful nanoscale material characteristics for many potential technological applications.[8,27] The rest of this chapter will be

devoted to describing the attributes that make these fascinating nanostructures materials so unique for these applications and why a detailed characterization of these materials on a single-molecule level is essential before they can be employed in technological applications in the future.

2.1 Surfactant-Templated Mesoporous Silica (STMS) Materials

2.1.1 Introduction

Surfactant-templated mesoporous silica (STMS) materials of interest in this dissertation form a unique class of nanostructured materials comprising nanoscale cylindrical pores with a characteristic dimensions of 2-50 nm.[38,39] They have been commonly prepared using a well-established sol-gel-process in which amphiphilic surfactant molecules (e.g. cetyltrimethylammonium bromide, CTAB) are used as structure directing agents.[40] A schematic of the two-step synthesis process is shown in **Figure 2.1**. In the first step, alkoxysilane precursors such as tetramethoxysilane (TMOS) or tetramethoxysilane (TEOS) undergo a hydrolysis with the aqueous phase in the presence of a catalyst (acid or base) upon mixing the reagents to form a sol. Subsequently, a rigid silica-gel is formed upon cross-linking the hydrolyzed silica precursors in a condensation reaction (**Figure 2.1**).[41] While this process is often run alone, producing a dense nonporous material, it can also be run in the presence of structure-directing surfactant micelles. Importantly, the final structure, the morphology and porosity of the silica gel are determined by several parameters such as silica-precursor-water ratio, nature and concentration of catalyst and any subsequent processing conditions such as drying and calcination.[41] These parameters allow mesoporous silica materials to be tuned and optimized in a flexible and controlled manner. For example, an acid catalyzed sol-gel-process commonly offers silica networks with relative low porosity, whereas based-catalyzed reaction in general produces xerogels with intrinsic higher porosity.[41] Thin STMS films can be prepared by simple spin-coating[42] or dip-coating procedures.[40] The first was employed in the current study for preparation of STMS films containing well-organized mesopore structures. These structures were characterized by SMT, quantifying the orientation of single mesopores and also order with µm-scale domains.

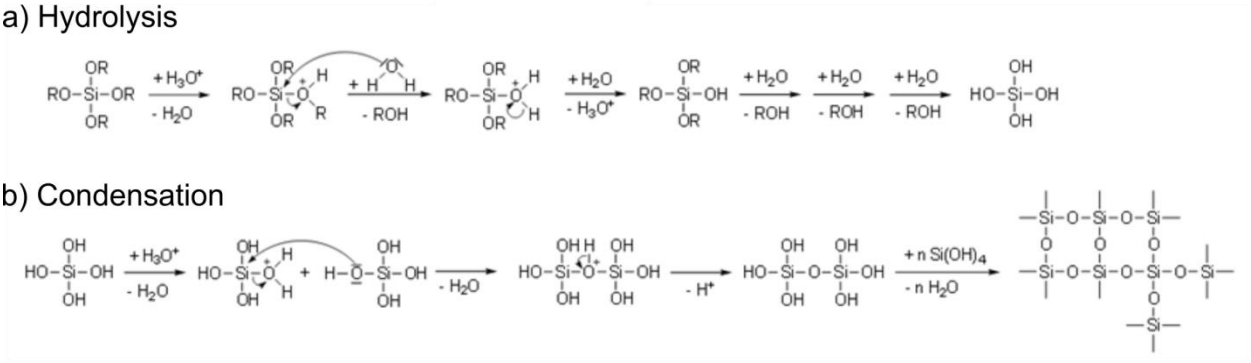

Figure 2.1. Acid-catalyzed two-step synthesis of mesoporous silica materials: a) Hydrolysis and b) condensation of silica precursors.[41] Adapted with permission from Ref (39). Copyright 1990 The American Chemical Society.

2.1.2 Properties of STMS films

In the present study, thin CTAB-templated mesoporous silica films exhibiting hexagonally-packed cylindrical morphology hve been prepared by spin coating a small amount (ca. 200 µL) of the aged sol.[22] Spin coating is a simple, straightforward method for preparation of a thin film with defined thickness. Conceptually, the approach relies on the controlled removal of solvent which in turn leads to the formation of phase-separated colloidal structures in the presence of templating surfactants. Nucleated features then gradually grow into ordered structures of macroscopic sizes.[32]

Sol-gel-derived STMS materials have recently gained popularity for industrial applications for several reasons. First, STMS materials commonly comprise nanoscale pores with a tunable pore size and a narrow pore size distribution.[43] These materials can be prepared using relatively simple and time-efficient procedures at low cost.[44] They can also be easily modified with well-established chemistries, thus offering valuable means for their optimization in potential applications.[43] Furthermore, the reaction conditions are mild, commonly occurring at room temperature, which also favor the incorporation of many reagents (enzymes, catalyst or receptors) without degradation of their activity and reactivity.[45]

2.1.3 Applications of STMS Materials

STMS materials prepared using the sol-gel-process have been recently employed as membranes for chemical separations[46] and sensing,[47] as substrates for catalysis,[46] materials for nonlinear optics[48] and solid-state electrochemical devices.[13] In all cases, the presence of uniform and well-defined mesoporous structure has played an important role in the selectivity and efficiency of the applications.[9] In fact, the separation performances of mesoporous silica materials have been shown to be directly defined by the morphology of the nanostructures. For example, chromatographic band broadening is linked to the presence of strong adsorption sites on the nanostructure surfaces. The defects often lead to adsorption and desorption events of molecules at the surface in a statistically random process.[49,50]

For all described applications, it is essential to use mesoporous silica materials with pores aligned along a predefined direction over a long-range (> μm). Randomly oriented mesopores in such materials are frequently formed during synthesis, which will lead to suboptimal performance characteristics in the applications of these materials. Thus, mesopore alignment methods have been employed for several years to prepare a macroscopic material containing well-organized mesopore structures aligned along one defined direction, as described in the next section.

2.1.4 Mesopore Alignment in STMS Materials

In recent years, several methods have been developed for preparation of aligned cylindrical mesopores in STMS materials. These techniques include magnetic[51] and electric fields,[52] substrate modifications[53] and patterning[54] and also using directional flow of the surfactant-containing sol in confined geometries.[55-57] For example, Chmelka and coworkers pioneered the use of strong magnetic fields for the mesopore alignment in STMS films.[51] By applying a magnetic field during gelation, highly-ordered mesopore structures with long-range continuity have been prepared. External electric fields also have been used by the Walcarius group for fabrication of vertically-aligned mesopores on an underlying electrode.[52] However, it is challenging to obtain longer-range alignment by this approach because of the limited electric field strength that can be applied without risking degradation of the materials. Mesopore alignment can be also induced by exploiting surface interactions with the underlying substrate. In fact, it has been shown that aligned STMS mesopores can be prepared upon rubbing a small amount of surfactant-containing sol on a

polyimide film.[53] The simplest approach, however, involves the flow or injection of sol solution into microfluidic channels,[56] glass capillaries[58] and AAO membranes.[59] Here, long-range mesopore alignment is primarily induced by shear forces acting during the directional flow into the confined structures. Importantly the long-axis of the mesopores have been found to be oriented parallel to the channel long-axis. This free-standing monolithic silica is particularly useful for chemical separation technologies.[10]

In the present work, we employed an even simpler approach for alignment of the cylindrical mesopores in STMS films using the so-called vertical-spin-coating approach, in which the sol was spun along an axis parallel to the film plane.[22] In the common spin-coating method, STMS films could also be prepared by spinning the underlying substrate along a rotation axis perpendicular to the film-plane.[42] Such an approach is predicted to produce tangentially aligned mesopores due to the radial shear forces acting during spin coating. In contrast, we expect to observe mesopore alignment along one direction, primarily defined by the directional flow of the sol during vertical-spin coating.

For the assessment of local mesopore orientation and order, SMT methods were employed. SMT has several important advantages over conventional XS or electron microscopy (EM) methods because it can assess the temporal and spatial heterogeneities of mass-transport and material characteristics on a single-nanostructure and single-molecule level.[17] SMT methods can be also used to assess the local morphology and structures, and their ability to guide and support mass-transport. Additional details on these advantages and relevant previous works will be discussed in chapter 3.

2.2 Phase-Separated Block Copolymers (BCPs)

2.2.1 Introduction and History of BCPs

BCPs are macromolecules comprising two or more chemically-distinct polymer segments (also called blocks) which are connected with each other via a covalent bond. Based on the number of blocks and the molecular arrangement (e.g. linear or branched), BCPs can be classified into subgroups. For example, an AB type diblock or ABC type triblock copolymer consist of two or three chemically distinct fragments. Furthermore, BCPs can also be classified based on their structural arrangements including linear, looped (end-to-end) or a star-shaped structures.[60] Most of the BCPs synthesized so far are linearly-structured AB type BCPs including the PS-*b*-PEO used in this study. Its chemical structure is shown in **Figure 2.2a**.

In general, BCPs contain thermodynamically incompatible polymer segments which frequently lead to a microphase-separation of their structures, similar to oil in water, but yet on a much smaller length scale, due to the presence of a covalent bond between the distinct polymer fragments. Microphase-separation commonly leads to self-assembly of various BCP morphologies with a characteristic length scale of 5 – 50 nm.[5,61,62] Under thermodynamic equilibrium, a linear AB diblock copolymer self-assembles into morphologies with distinct spherical (S, S'), cylindrical (C, C'), gyroidal (G, G') and lamellar (L) structures (**Figure 2.2b**).[5] These morphologies have been theoretically predicted and experimentally observed in numerous studies (**Figure 2.2c**). For BCPs with three or more blocks, the phase diagram is more complex due to a larger number of possible distinct and unique morphologies.[5] The phase-separated domain size has been reported to be dependent on the molar masses and the incompatibility of the copolymer fragments.[60] More importantly, the theoretically-predicted and experimentally-confirmed bulk morphology, periodicity and microdomain dimension at equilibrium is largely determined by the volume fraction of a block (f_A), the polymerization degree (N) and the chemical incompatibility as represented by a Flory-Huggins interaction parameter (χ).[5,60] These parameters offer valuable means for controlling the fabrication of various architectures being used in technological applications. Importantly phase-separation occurs on a nanoscale dimension because of the presence of a covalent bond connecting each of the copolymer fragments, preventing macroscale phase separation as observed for a polymer blend.[5]

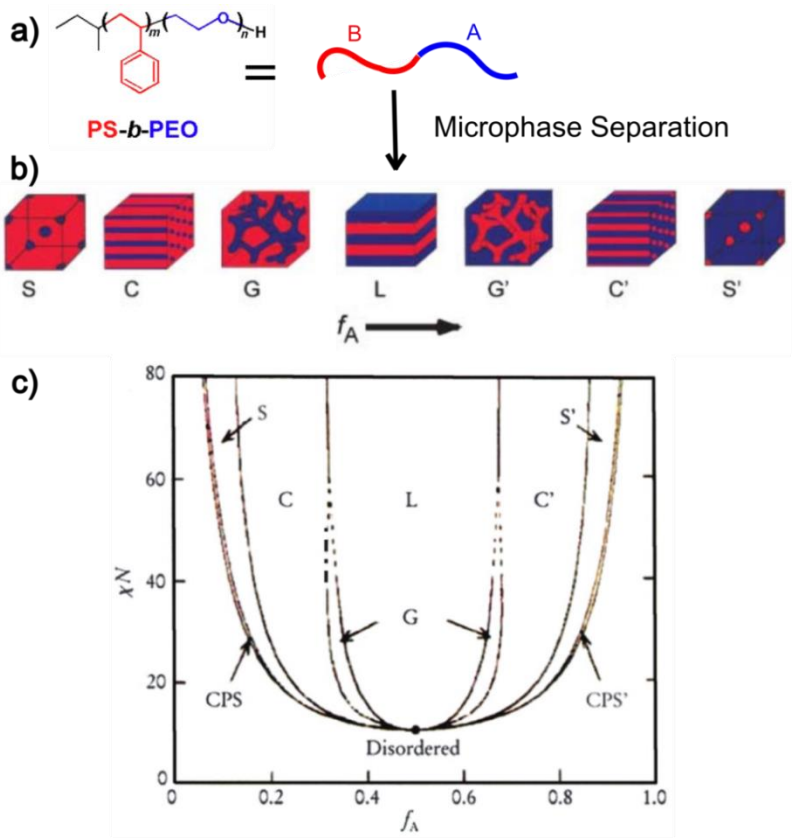

Figure 2.2. (a) Chemical structure of PS-*b*-PEO. (b) Upon microphase separation, equilibrium microdomain morphologies of an linear AB diblock copolymer are present: spheres (S, S'), cylinder (C, C'), gyroid (G, G') and lamellar (L). (c) Theoretical phase diagram of a linear AB diblock copolymer calculated using self-consistent mean-field methods.[5] Adapted with permission from Ref (5). Copyright 1999 American Institute of Physics.

In 1956, Szwarc and coworkers reported the first successful synthesis of a BCP using anionic polymerization technique.[63] Using the method, BCP materials have been synthesized with small polydispersity (PDI) (M_n/M_w <1.05), thus being one of the more industrially-relevant techniques. In fact, technologically-important BCPs such as polystyrene-polybutadiene-polystyrene triblock copolymer (SBS), poly(oxyethylene)-b-poly(propylene)-poly(oxyethylene) (also known as Pluronics) as well as our PS-*b*-PEO have been synthesized using the method. However, it is technically relatively demanding, requiring a high-vacuum level and high purity of the starting reagents in order to prevent uncontrolled chain-termination processes.[64] More recently, BCPs have also been synthesized using controlled/living radical polymerization, which is more tolerant of

impurities and allows for a wider range of functional groups, making it currently the leading technique for polymer synthesis on an industrial scale.[64]

To date, a large variety of BCPs with different block constituents (e.g. styrene, isoprene, butadiene, vinyl, methylmethacrylate, etc.) have been synthesized using either one of the aforementioned techniques. Importantly, these well-established techniques have allowed the synthesis of BCPs with well-controlled compositions (chain length and volume fraction) and a narrow compositional distribution (small polydispersity index), which in turn defined the resulting well-defined phase-separated morphology (size, shape and structure of microdomain).[60] The ability tune the BCP morphology in a controlled and efficient manner is thought to be a major reason for the popularity of BCPs and their derived nanoporous materials for technological applications and fundamental research.[65-67] Possible applications include templates for material synthesis,[68] photolithographic masks,[69,70] separator membranes for energy conversion and storage,[71,72] as well as media for sensing[73,74] and separations.[75] It should be noted that the majority of applications utilize nanoporous membranes and media derived from BCP precursors rather than using the original phase-separated BCP morphologies.[65] However, before nanoporous materials can be derived from their precursors, such BCP microdomain structures need to be well understood and characterized first.

Among the large variety of BCPs, cylinder-forming polystyrene-poly(ethylene oxide) diblock copolymer (CF-PS-*b*-PEO) has recently attracted considerable attention in science and technology because of its unique material properties which make it suitable for many potential applications such as precursors for fabrication of nanoporous membranes,[76] as templates for nanoscale quantum dots and for nanotubules synthesis,[77,78] substrates for nanoelectrode arrays[79] and as polymer electrolytes for lithium-ion batteries.[71,72] In the next few sections, the origin of the unique properties of CF-PS-*b*-PEO will be described, along with more detail description on several important applications of CF-PS-*b*-PEO. Furthermore, the challenges of using CF-PS-*b*-PEO will be highlighted.

2.2.2 Properties of CF-PS-b-PEO

The CF-PS-*b*-PEO used in the present study comprises a glassy major (80% v/v) block of PS and a rubbery minor (20% v/v) block of PEO. Its chemical structure is depicted in **Figure 2-2a**.

CF-PS-*b*-PEO is observed to self-assemble into hexagonally-packed cylindrical morphology in which PEO forms the cylindrical microdomains and PS the supporting matrix. This process is thermodynamically driven by the immiscibility between the more hydrophobic PS and the more hydrophilic PEO.

The physical properties of the microdomains and the supporting matrix of CF-PS-*b*-PEO at room temperature are directly defined by the properties of the PS and PEO fragments: PS is a relatively hard, glassy polymer at room temperature with high glass transition (*ca.* 103 ºC)[80] and melting temperature (*ca.* 200 ºC).[80] In contrast, PEO is commonly in a rubbery state at room temperature because its glass transition temperature (*ca.* - 61 ºC)[80] is significantly below room temperature. These values were provided by the manufacturer (Polymer Source) for the identical CF-PS-*b*-PEO used in this study.[80] The unique properties of each of the homopolymers have led to the hybrid nature of PS-*b*-PEO, providing both flexibility and mechanical stability in one material. As a consequence, microdomains in CF-PS-*b*-PEO and their BCP-derived membranes have attracted significant interest for several possible future applications as summarized in the next section.

2.2.3 Applications of CF-PS-b-PEO

In recent years, CF-PS-*b*-PEO has been used for fabrication of nanoporous films and membranes comprising uniform cylinder-shape pores of tuneable size and well controlled orientation.[21] These materials can be fabricated by a relatively simple two-step procedure. First, solvent evaporation induces phase separation and self-assembly of cylindrical nanoscale domains of the minor component(s).[65,81-83] Subsequent selective etching of the cylindrical domains via a hydriodic acid mediated cleavage of the aliphatic ether linkage leads to the formation of nanoporous monoliths. [76,84,85] More recently, a wealth of different cleavable PS-*b*-PEO BCPs have been synthesized and employed for the fabrication of a nanoporous BCP materials through a chemical[68,69] or photochemical procedure[86,87]. These nanoporous materials have been employed as synthesis templates for nanomaterials including gold nanotubules,[85] silicon and silicon dioxide dots[78,88] but also as membranes for chemical separations[89] and water purification.[90,91] In some applications, the native CF-PS-*b*-PEO microdomain structure has also been used as a synthesis

template for titania nanoparticles[92] and more importantly as a good model system for lithium-ion-battery research.[72]

Conceptually, nanomaterials synthesis using nanoporous CF-PS-*b*-PEO as a template relie on the incorporation of nanomaterial precursors into the open voids, followed by subsequent growth of the nanomaterials and finally by removal of the nanoporous template by dissolution of the polymer.[88] The remaining nanoparticles and tubes form well-ordered arrays of nanoscale features adapted from the arrangement of the vertically aligned cylindrical nanopores. In contrast, Sun and coworkers have reported the synthesis of titania nanoparticles array using a phase-separated CF-PS-*b*-PEO film instead.[92] Here, sol-gel-precursors were spin cast on a phase-separated BCP film having vertically aligned microdomains supported on an underlying substrate. Due to the hydrophilic nature of the precursors, an enhanced segregation in the PEO microdomains was observed. Thus, upon calcination of the composite materials at a high temperature (*ca.* 600 ºC) which selectively decomposed the CF-PS-*b*-PEO template, highly ordered arrays of titania nanoparticles could be obtained.[92]

Nanoporous CF-PS-*b*-PEO membranes have also been extensively explored as a result of their potential applications in chemical separation and water purification.[89-91] In both cases, separation is primarily based on the size-exclusion properties of the nanoscale pores, allowing only analytes to permeate through the membranes if their size is sufficiently small compared to the nanopore diameter. In particular, the work of Li et al. showed that upon embedding a small fraction of a hydrophilic homopolymer such as poly(acrylic acid) within the cylindrical microdomains and subsequent selective removal, well-aligned cylindrical nanopores could be created.[89] This system has been shown to be capable for separation of small molecules. The Peinemann and Abetz groups employed the fabrication of integral-asymmetric membranes using CF-PS-*b*-PEO as a template.[90,91] These type of nanoporous membranes were prepared by a two-step procedure involving the solution-casting of the phase-separated BCP membranes before nanopores could be formed through a solvent-nonsolvent exchange process also known as phase-inversion. [90,91] The nanoscale pores exhibited a highly-ordered hexagonal structure with the long-axis oriented perpendicular to the membrane as required for a filtration membrane (**Figure 2.3a**). Importantly, the water flux across the membrane was observed to be time-dependent due to the swelling of PEO-layers on the nanopore surface, which allowed the flux to be controlled by the swelling kinetics of PEO (**Figure 2.3b**).[91]

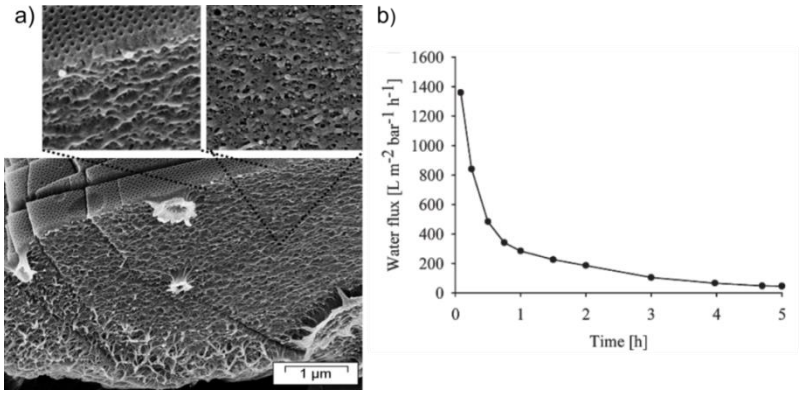

Figure 2.3. (a) Cross-sectional SEM images of a filtration membrane derived from CF-PS-*b*-PEO using phase-inversion approach. (b) Flux across the membrane as a function of time.[91] Adapted with permission from Ref (91). Copyright 2012 Wiley Periodicals Inc.

More importantly, CF-PS-*b*-PEO has been extensively studied because of its ability to conduct ionic current (e.g. Li^+) along the cylindrical PEO microdomains. These works are aimed to develop PEO-containing BCPs to be used as a second-generation polymer electrolyte in lithium-ion batteries.[71,72,93] PEO is well-known to exhibit a high ionic conductivity at room temperature mainly due to its relatively low glass transition temperature which allowed ions to be transported by intrinsic chain motions.[93] Combining PEO with a second major (large volume fraction) block with higher glass transition temperature afforded the material higher mechanical stability, crucial for many potential applications but particularly important for energy storage and conversion. In several studies of the Balsara and Epps groups, the ionic conductivity was investigated as a function of salt concentration and type, morphology, molecular weight and in the presence of defects and grains.[71,72] Charge transport in PEO has been shown to be strongly determined by such parameters. However, a much deeper knowledge of these processes is essential before CF-PS-*b*-PEO can be integrated in future versions of lithium-ion batteries.

For many of these applications, monolithic materials comprising closely-packed, highly-aligned anisotropic (*i.e.*, cylindrical and lamellar) microdomains over a macroscopic size are desired. However, it is often challenging to align the cylindrical domains in CF-BCP monoliths along one direction.[94] Poor alignment of the domains (and nanopores) leads to sub-optimal performance in their technological applications. In particular, BCP monoliths often consist of µm-scale 'grains' formed from highly-ordered cylindrical or lamellar microdomains.[95,96] Such grain

formation often limits the continuity of microdomains to μm length scales due to different microdomain orientations in adjacent grains. To overcome such limitations, solvent annealing,[84,97-101] surface modification/patterning,[100,102] salt complexation[78,103] and homopolymer additives[83,89,98] have been used to induce a longer-range PEO microdomain alignment in CF-PS-*b*-PEO films. The next section begins with reviewing previous approaches for aligning cylindrical microdomains of BCP in general over a long distance, followed by highlighting the works on CF-PS-*b*-PEO.

2.2.4 Alignment of CF-PS-b-PEO Microdomains[23,24]

Improving, controlling and understanding the microdomain orientation in BCP materials and their mechanisms have been an active research field for several years.[21,104] Improved alignment in thin CF-BCP films has been attained previously by application of magnetic[105] and electric fields[106] during thermal annealing, and also by use of interfacial interactions,[107,108] flow[109] or solvent evaporation/permeation.[97,101,110-114] These often involve application of external fields during microphase separation.[21] Among them, shear-based and solvent-based approaches have been widely explored for several decades.[21,94] These approaches are simple, applicable to large sample volumes and suitable for various BCP systems as solid-state structures or in melt and solution.[115] In addition, shear-based approaches also provide metastable microdomain morphologies different from thermodynamic nanostructures in equilibrium.[116]

Flow-Based Microdomain Alignment. Flow-based approaches are one of the earliest developed methods for microdomain alignment of BCPs. In pioneering work from 1970, Keller et al. successfully prepared a millimeter-scale, monolithic plug with well-ordered microdomains via the extrusion of molten SBS triblock copolymer through a circular die.[117] SAXS measurements of the resulting plug revealed arrays of cylindrical PS microdomains exhibiting near-crystalline order. In a later study, Albalak and Thomas reported the fabrication of millimeter-thick SBS films comprising highly-oriented PS microdomains over macroscopic length scales by using a roll-casting approach.[118] The formation of well-ordered cylindrical and lamellar PS microdomains aligned along the rotation direction was revealed by SAXS and TEM, and explained by the hydrodynamic flow and gradual drying of a SBS solution between two rotating cylinders. As

compared to a polymer melt, microdomain formation/alignment from a polymer solution takes place in a more complex manner due to the complicated phase behavior and significant volume change of the BCP solution due to solvent evaporation.[118,119] These pioneering works demonstrated the fabrication of well-aligned BCP microdomains by shear flow of a melt or solution within a confined space. Shear flow has also been used to align other nanostructures such as nanowires[8,120] and to elongate/align cylindrical micelles[55-57,121,122] within microfluidic channels. However, flow-induced alignment does not always offer macroscopically uniform BCP monoliths with perfectly aligned microdomains. Instead, a randomly-distributed mixture of μm-scale grains consisting of microdomains aligned and misaligned in the flow direction is often obtained, as previously observed in polystyrene-polyisoprene diblock copolymer films using polarized optical microscopy.[95]

Solvent-Based Microdomain Alignment. The solvent-based approaches, including solvent vapor annealing (SVA) and solvent vapor permeation (SVP), have also been widely employed because they are relatively simple, time-efficient and applicable for samples of large lateral area.[66,111] Domain alignment can be attained by exposing CF-BCP films to an organic solvent vapor in a closed container. A variety of organic solvents and solvent mixtures can be used to optimize domain morphologies, by controlling the solvent affinity to the polymer fragments and the solvent evaporation/permeation rate.[114] SVA has been employed to obtain improved alignment of cylindrical domains in thin films of various CF-BCPs,[110] including CF-PS-*b*-PEO.[97,101,113] In fact, Kim and coworkers pioneered the PEO microdomain alignment in CF-PS-*b*-PEO film (ca. 250 nm thick) based on SVA with benzene.[97] This approach exploits the directional solvent evaporation perpendicular to the film surface to form highly-ordered cylindrical nanostructures with a diameter of ca. 24 nm. However, SVA can only induce alignment over relatively short distances (< 1 μm) because of incomplete solvent removal from deeper film regions.[97] In subsequent work, the Russell group studied the effects of humidity,[84] homopolymer[98] and salt complexation[103] on the PEO microdomain orientation, but it remains challenging to align the nanostructures across the entire film thickness. More recently, Osuji pioneered the SVP approach for achieving long-range alignment in CF-BCPs (see **Figure 2.4a)**.[25] In SVP, aligned cylindrical domains are produced on the basis of solvent permeation from one end of a monolith to the other. This method has offered domain alignment over a significantly longer scale.[25,111] For example,

pressure-driven penetration of tetrahydrofuran (THF) vapor was employed to attain sub-millimeter alignment of the microdomains in a SBS film.[25]

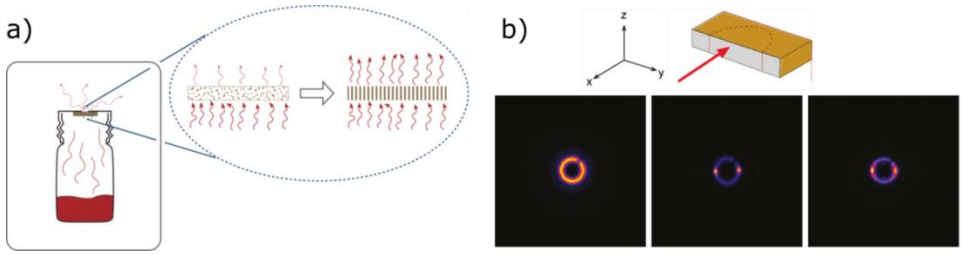

Figure 2.4. (a) Experimental setup for SVP of a SBS membrane, producing a long-range microdomain orientation in the SVP-direction. (b) SAXS measurements revealed the macroscopic microdomain alignment of SBS as represented by anisotropic scattering intensity (middle, right) as compared to isotropic case (left) before SVP.[25] Adapted with permission from Ref (25). Copyright 2010 American Chemical Society.

Based on the previously reported work, we sought to align the cylindrical PEO microdomains in a CF-PS-*b*-PEO film using the flow and SVP-approaches.[23,24] Using the directional flow of PS-*b*-PEO solution, we explored different conditions and their impact on the microdomain alignment. This allowed the best condition to be found and more importantly to reveal the possible mechanism behind the microdomain alignment process.[24] In the latter approach, we assessed the microdomain alignment induced by SVP with three different organic solvents having different selectivity for each of the blocks.[23] As compared to the previous works which employed SAXS, SEM/TEM and AFM for characterization of the morphology, we probed the PEO alignment using SMT. The major advantage of SMT is its capability to assess the local microdomain orientation and size, as well as domain order of CF-PS-*b*-PEO films under ambient conditions and with a high spatial precision. Furthermore, SMT offered assessment of the mass-transport characteristics of the microdomains. In Chapter 3, SMT is introduced as a tool for characterization of 1D nanostructures, along with its instrumentation and previous applications. We also discuss the advantages/limitations of SMT as compared to conventional methods.

Chapter 3 - Methods for Characterization of 1D Nanostructured Materials

This chapter describes conventional and fluorescence-based methods for the characterization of nanostructured materials comprising cylindrical nanopores and domains. Conventionally, the nanoscale morphologies of the nanostructured materials have been probed by x-ray scattering (SAXS, XRD), atomic force microscopy (AFM) and electron microscopy (SEM/TEM). These methods offer complementary information on the macroscopic (mm-scale) or local (nm-scale) morphology. They measure the diameter, spacing and orientation of the pores and domains under various conditions (e.g. ambient air, solution or vacuum). However, such information in general reflects physical properties of the nanostructures with limited information on mass-transport properties of the materials. It is not generally known if the nanostructures observed by these methods are accessible and continuous for molecules. Their roles in guiding, restricting and supporting the molecular mass-transport therein are also poorly understood at present. These questions have been recently addressed by fluorescence-based methods, including flux measurements, SMT and FRAP. Flux measurements and FRAP provide ensemble-averaged mass-transport characteristics of the materials for the entire film or membrane or of a small region of the sample. In contrast, SMT probes the local diffusion dynamics of molecules along μm-scale distances with high spatial resolution. These data have revealed the ability of nanostructures for facilitating molecular mass-transport within their confined geometries, characterizing the nanoscale materials therein. The results have demonstrated the usefulness of fluorescence methods and in particular SMT for the in-depth characterization of mass-transport and materials with a high spatial precision under ambient environments.

3.1 Conventional Methods

3.1.1 X-Ray Scattering Methods (SAXS/XRD)

The morphology of the cylindrical nanostructures in a macroscopic area of BCP and STMS films and monoliths has been commonly assessed by small angle X-ray scattering (SAXS)[25,84,97,112] and X-ray diffraction (XRD) techniques,[123,124] respectively. Both methods offer information on average domain and nanopore structures, spacing and orientation over macroscopic sample regions (often mm or larger) and throughout the entire thickness of the bulk materials. SAXS/XRD can be used to probe domain orientations/morphologies under ambient conditions (e.g. in air and in the present of organic solvents) or under vacuum, matching the conditions often employed in technological applications.

In the general, a X-ray scattering instrument consists of two major components: a X-ray source (e.g. X-ray tube) and a detector (2D or 1D). The morphology of the nanoscale structure is probed by irradiating the sample with a broad (mm-scale) X-ray beam and by simultaneous recording the elastic scattering intensity of the X-ray from the sample. In SAXS, a 2D detector is often used to image the scattering pattern at very small angles ($2\theta < 2^o$), whereas XRD data are collected by recording the scattering intensity at different larger scattering angles ($2\theta > 2^o$) as compared to SAXS (see **Figure 3.1**). Importantly, the scattering angle (θ) is directly governed by the spacing/distance (d) between the periodic structures (domains or pores) given by Bragg's law (**Figure 3.1**).

$$2dsin\theta = n\lambda \qquad \text{(Eq. 3.1)}$$

where λ is the wavelength of the X-ray (0.154 nm) and n the order of the scattering peak. This equation predicts the angles at which the scattering intensity is greatest due to the constructive interference (n_{con} = 1, 2, 3,…) of scattered intensities from the two neighboring structures such as domain or pores. Thus, the scattered intensity offers valuable information on the periodicity and average morphology of the materials across the entire thickness for a macroscopic sample region.

However, X-ray scattering is not suitable for revealing the local structure and morphology as well as sample heterogeneities (e.g. defects) in the materials because it spatially averages the information in a macroscopic (< 0.1 mm in width or less) sample area (**Table 3.1)**. In addition, the samples require a sufficiently large volume or thickness for obtaining sufficiently large scattering intensities. Most importantly, SAXS/XRD cannot offer information on the ability of

the nanostructures to facilitate molecular mass-transport, highly important for technological applications such as chemical sensing or separations.

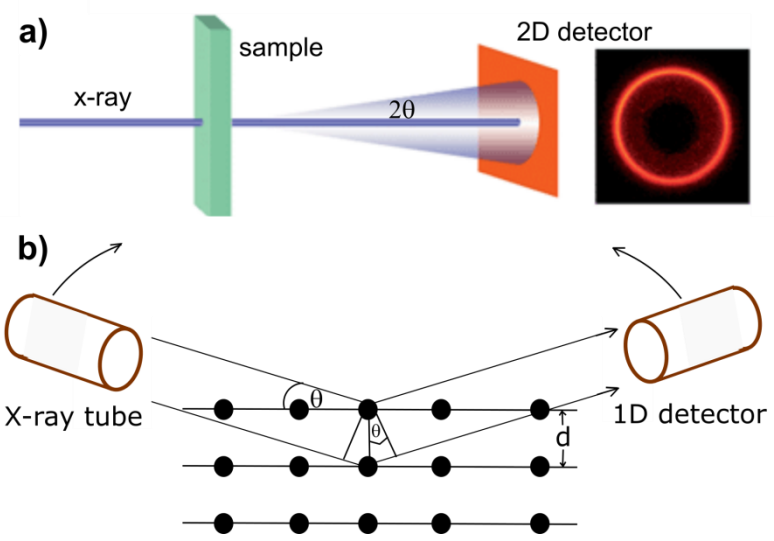

Figure 3.1. Schematic of a (a) SAXS instrument with its major components: a X-ray source, sample and a 2D detector. The SAXS data are collected simultaneously for small scattering angles (2θ) in a stationary mode.[125] (b) In contrast, the XRD instrument collects diffraction data of STMS films at different larger 2θ (compared to SAXS) using a moveable X-ray tube and 1D detector. The Bragg's Law can be derived by considering the interference of two neighboring X-ray beams being scattered from two periodic structures (e.g. pores) separated by a spacing *d*. Adapted with permission from ref (125). Copyright 2009, The Royal Society of Chemistry.

3.1.2 Atomic Force Microscopy (AFM)

Atomic force microscopy (AFM) also has been widely employed for assessment of the morphology of the nanostructures.[84,97,101,110-114] It can directly image the surface topography and exposed nanoscale structures of the materials with a high lateral (*ca.* 2 - 10 nm) resolution in a μm-scale sample area.[126] AFM measures the local surface information of the nanostructure under various environments: ambient air, controlled atmosphere, in solution or ultrahigh vacuum.[127] As with SAXS, AFM is also a useful method for characterization of non-conductive materials such as polymers without any pretreatment (e.g. thin metal layer coating) as compared to SEM/TEM.[127]

The main components of an AFM comprise a very sharp tip (with a typical radius of 2 -10 nm) made of Si or Si_3N_4, a cantilever, a laser, a photodiode detector and a piezo-electric scanner (**Figure 3.2**).[127] The measurement is performed by approaching the tip very close (*ca.* 1 nm in non-contact mode) or onto the sample surface, resulting in a weak interaction force (10^{-12} – 10^{-7} N) between the tip and the sample surface. The force might originate from adhesion, electrostatic, van der Waals, capillary or repulsive interactions and is measured as the deflection of laser light from the µm-size cantilever containing the tip at its end.[127] For probing the local surface morphology over a µm-scale wide sample region, the tip is raster-scanned over the sample surface by moving the samples underneath the tip using a piezo-electric device with sub-nm precision (**Figure 3.2**). The obtained image features 3D structures on the surface of the material with a high lateral and vertical resolution, primarily defined by the sharpness of the AFM tip and also the nature of the interaction forces between the tip and sample.[127]

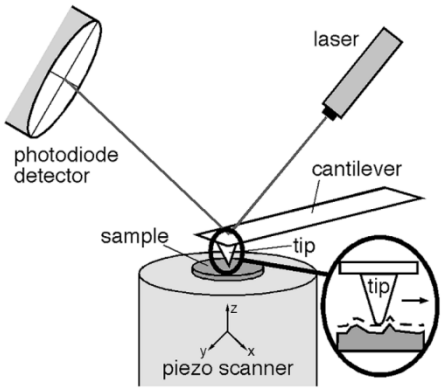

Figure 3.2. Schematic of an AFM instrument comprising a photodiode detector, a laser, a cantilever with an end-attached sharp tip and a piezo-electric scanner.[128] Reprinted with permission from ref (128). Copyright 2010, Elsevier.

Commonly, AFM measurements are conducted using contact and tapping-mode. In the first approach, the tip is in permanent contact with the sample surface during the AFM measurement. A feedback system is employed to maintain a constant tip-surface-contact, yielding a 3D image of the surface topography of the materials. In tapping-mode, the sharp tip is scanned across the sample surface under continuous tapping on the surface of the material with a characteristic frequency, highly sensitive to the probe-sample interactions. Thus, the variation of such frequency

and phase is used to probe the surface chemistry and topography of the film. The latter mode is superior over the former, because it can clearly distinguish the microdomain structures on the surface of a BCP film, being a frequently-used method for probing microdomain orientation and organization, in addition to offering the estimates on the domain diameter.[126] In the contact mode, the domain morphology can also be recognized, based on the height-differences between the distinct domains. Yet this is often more challenging than using the phase information of the tapping-mode AFM. In addition, soft polymer samples may be damaged by the continuous contact of the sharp tip with the surface.

Unfortunately, AFM also exhibits significant limitations in the characterization of nanoscale morphology and structures of films and monoliths (**Table 3.1)**. First, AFM only offers information on the surface topography of exposed materials. It cannot measure the bulk properties of the materials. Secondly, AFM is not suitable for material characterization on rough surfaces due to its intrinsic difficulties in probing rough surfaces. It is also challenging to obtain the longer-range (>10 μm) information on the nanoscale morphology of BCPs and STMS using AFM as compared to X-ray scattering. As with the latter, this method cannot afford important information on the mass-transport-related material characteristics.

3.1.3 Electron Microscopy (EM)

Electron microscopy such as transmission electron microscopy (TEM)[113] and scanning electron microscopy (SEM)[76,113,129] have been also employed to assess the nanoscale morphology of the cylindrical nanostructures. These microscopic methods directly image local morphology of nanopores and domains with high spatial (< 1-5 nm) resolution, allowing for diameters, spacing and orientation to be determined for relatively small μm-scale sample regions. Importantly, SEM probes the surface topography of the exposed materials, yielding 2D projected images of topographical surface features. On the other hand, TEM images the nanoscale structure of very thin (< 100 nm) slices of a sample as a result of electron transmission across the thin layer of the material.

The main components of an EM include an electron source (e.g. field emission gun), suitable optics (e.g. electron lenses and aperture) for focusing the electron beam, a vibration-isolated sample stage and electron detectors. [129] In general, an EM probes a sample by focusing an electron beam onto the sample under simultaneous recording the scattered or transmitted electron beam

from it, yielding high resolution surface and cross-sectional material characteristics of a μm-scale sample region. In SEM, the probing electrons are observed to undergo multiple interactions with the materials at different penetration depths.[129,130] For example, secondary electrons are scattered from a shallower (*ca.* 2 – 5 nm in depth) surface region, revealing the surface information of the materials.[130] In contrast, the backscattered electrons (BE) originated from elastic scattering from deeper region (up to 400 nm in depth) of the materials and offers information on their chemical composition of the materials, as BE scales up with the atomic number of the constituent atoms in the materials.[130] In TEM, a beam of electron is irradiated through a thin slice of a nanostructured material, before being detected on the other side of the sample. As the scattering cross-section is highly dependent on the atomic number of the constituent atoms in the materials, the transmitted electron intensity can be used to probe the nanostructures, providing information on the morphology of the samples with a high spatial resolution (0.1 nm or lower) for sub-μm sample regions.[130]

Electron microscopy also shows significant limitations for characterization of nanostructured materials (**Table 3.1**). First, imaging the morphology of polymer samples is challenging because of their intrinsic low electric conductivity that often leads to severe surface charging effects during imaging. To overcome such problems, the non-conducting polymer materials are frequently stained with heavy-metal compounds or coated with a thin-layer of a conducting material such as gold before the measurements. Second, TEM and SEM provide nanostructure morphologies of dried materials under ultrahigh vacuum and are not suitable for probing the solvent-swollen morphology of nanostructures. Note that cryo-TEM can be also used for freeze-dried samples, thus allowing the morphologies to be imaged under a quasi-wet environment.[131] However, freeze-drying can also change the natural characteristics of the nanostructures. As with XRD and AFM, EM cannot provide any evidence on the ability of nanostructures on supporting the mass-transport therein. These limitations have been recently addressed by fluorescence-based methods as described in the rest of the section.

Table 3.1. Comparison of Conventional Methods for Characterization of the Physical Properties in Nanostructured Materials: SAXS/XRD, AFM and SEM/TEM.

	SAXS/XRD	**AFM**	**SEM/TEM**
Characterization	• macroscopic materials property: periodicity, spacing, morphology, orientation	• high-resolution surface topography: diameter, orientation, structure	• high-resolution nanoscale morphology: diameter, orientation, structure
Spatial Resolution	• low (0.1 mm or less)	• high (ca. 2 - 10 nm)	• TEM: very high (0.1 nm or less) • SEM: high (1-2 nm)
Dimension of Measurement	• lateral: wide (< 0.1 mm) area • vertical: entire thickness (> mm)	• lateral: narrow area (µm) • vertical: surface (nm)	• lateral: narrow area (µm) • vertical: surface (SEM), thin (<100 nm) slices (TEM)
Advantages	• imaging in air or vacuum • simple and non-destructive method	• offer local information • imaging in air, solution or vacuum	• offer local information from exposed surface (SEM) or cross-sectional layer (TEM)
Limitations	• spatially-averaged information • requires sufficiently large sample volume/thickness	• surface-specific information • not suitable for rough samples • lack of cross-sectional images	• required ultra-high vacuum • staining/coating for non-conductive polymers

3.2 Fluorescence-Based Methods

3.2.1 Molecular Flux Measurements

In the past, the cylindrical nanostructures in nanopore membranes have been explored regarding their ability to provide molecular pathways across the entire media. For such investigations, the flux of molecules across the nanoporous membrane was measured using a U-tube permeation cell or a conductivity cell.[30] In this setup, the nanoporous membrane is sandwiched between two solution-filled half-cells as illustrated in **Figure 3.3**. Importantly, one of the chambers (feed chamber) contains a solution with a high concentration (µM range) of the probe molecules, while the other, the permeate chamber, is initially free of such molecules. The setup permits the increase of the probe molecules' concentration (C_{perm}) in the permeate chamber to be monitored as a function of time (t) using UV/vis or chromatographic methods.[30] The increase of the concentration originates from the mass-transport of molecules across the nanoporous membrane, allowing the rate and selectivity of molecular mass-transport to be measured. The results also reveal the continuity and accessibility of the solution-filled nanopores for probe molecules in the membrane.[7] In general, the diffusion-controlled flux, J, of the molecules can be quantitatively assessed from the slope of the C_{perm}-t-relationship.[9]

$$J = -DP\frac{\varepsilon}{\tau}\frac{dC_{perm}}{dx} \qquad \text{(Eq. 3.2)}$$

where D is the diffusion coefficient, P is the partition coefficient, ε is the fraction of the materials cross-section containing open pores, τ is the pore tortuosity and dC_{perm}/dx is the concentration gradient.[132] Importantly, J is directly related to structural parameters of nanostructured materials (ε, τ), permitting the spatially-average information on number of open and continuous pores and the extent of pore alignment to be revealed.[9,18] In fact, Martin and coworkers investigated the effect of the physical size of pores and molecules on restricting the permeation of molecules across gold nanotubule membranes.[133] In a series of flux measurements, the size of probe molecules and nanopores were varied. The results show that the pores could exclude the molecules if their hydrodynamic diameter was similar or larger than the nanopore diameter, as represented by a negligible flux through the material.[133] As expected, the smaller molecules could access the sufficiently large nanopores. Yet, these measurements did not address the role of the material tortuosity because of the limited ability to characterize the local structures of the membrane.[18]

In general, the information obtained through the flux measurements reflects the spatially-averaged material properties of the entire membrane. Thus, these measurements cannot reveal important local morphology and nanoscale material characteristics including material heterogeneities and defects. Considering that these material heterogeneities contribute to the overall material properties and performance characteristics in technological applications, new methods need to be developed for the assessment of these local nanofeatures and to characterize the overall material characteristics. Ultimately, this will allow novel nanostructured materials to be developed, engineered and optimized for their applications in potential future technologies.

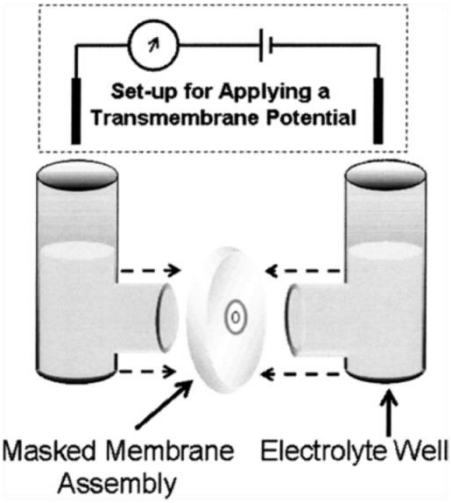

Figure 3.3. Schematic of an U-tube cell used for the measurement of the molecular flux across cylinder-shape nanopore membrane.[30] Reprinted with permission from ref (30). Copyright 2005, Taylor & Francis.

3.2.2 Single-Molecule Tracking (SMT)

3.2.2.1 Introduction

With the development of SMT in recent years, several challenges and limitations of previous ensemble measurements have been successfully addressed. Indeed, SMT has been employed to assess the local structures of the materials through the measurements of mass transport dynamics of molecules within the nanostructures.[17] The method relies on recording the trajectories of individual fluorescent probe molecules, reflecting the rate and direction of their motions. Considering that the probe molecules preferentially partition into specific nanoscale domains of interest, the probe trajectories provide structural information on these domains, revealing their ability to restrict, guide and support the molecular mass-transport.

In general, SMT offers several advantages over conventional methods (e.g., AFM,[97,113] SEM/TEM[118] and SAXS[117-119,134-137]) for characterization of nanostructured materials. These are based on its capabilities to detect, observe and visualize nanoscale domain and nanopore morphologies with high spatial resolution.[17,18] Since these processes are observed at the single molecule and single event levels, SMT offers quantitative information on the temporal and nanoscale spatial heterogeneity of most samples under various environments (e.g., in ambient air, under controlled environments and in solution).[138] Such variations are often obscured by the averaging that occurs when ensemble methods are employed. Furthermore, since the locations of single molecules can be determined to very high precision,[139,140] sub-diffraction limited spatial resolution (down to a few nanometers) can also be achieved in images reconstructed from the measured positions of diffusing and adsorbing,[141,142] or photomanipulated[143-145] molecules.

Historically, SMT has been employed for the first time by Schmidt and coworkers in 1996 to measure the diffusion coefficient of rhodamine-labeled phospholipids in a phospholipid membrane under ambient conditions.[19] The average of the 531 single-molecule diffusion coefficients (D_{SMT} = 1.4 ± 0.1 μm^2/s) was twice that of the ensemble diffusion coefficient (D_{FRAP} = 0.8 ± 0.1 μm^2/s) as estimated by FRAP. The results were attributed to the different length scales of the measurements: SMT measures diffusion along nm-scale distances, whereas FRAP commonly probes the diffusion of many molecules over μm-scale sample regions.[146] In the following two decades, SMT methods have been used to study the motions of molecules in one,[147-150] two[139,151,152] and three[153] dimensions on surfaces,[152] in polymer films,[151] lipid bilayers,[139,154]

Langmuir films,[139,155,156] in gels[153,157] and in cells and cell membranes.[158-160] These studies have afforded a wealth of new information on molecular motion, yielding quantitative data on diffusion coefficients, as well as entrapment and surface adsorption/desorption times.[161]

In recent investigations, SMT has provided unique means for material characterization of nanostructures:

(i) It revealed that the nanostructures were open, accessible to molecules and could support molecular diffusion of relatively large probe molecules.[148,162]

(ii) It afforded visual evidence on the presence of defects and material heterogeneities with a high spatial resolution including their role on the local mass-transport.[162-164]

(iii) It provided *qualitative* discussion on the sizes, orientation and order of the organized domains.[56,164,165]

However, more remains to be learned from such studies. For example, detailed *quantitative* analysis of the direction (i.e., the angle in the film plane) along which each molecule diffuses could provide important evidence of macroscopic channel alignment, especially when samples designed to exhibit such alignment have been prepared.[166-170] The same data can be used to determine the distribution of trajectory angles, and hence, the distribution of channel orientations. Importantly, the degree of trajectory alignment and hence the level of materials order can be quantified by calculation of order parameters from the individual trajectory angles.

In the present work, SMT is employed to *simultaneously* and *quantitatively* assess

(i) the orientation and size of individual 1D nanostructures (pores and microdomains),[22-24]

(ii) the local order of nanostructures in μm-scale regions of STMS and BCP film,[22-24] and

(iii) the diffusion direction and diffusion coefficients of individual molecules incorporated into the microdomains and nanopores in BCP and STMS films.[1,22]

Furthermore, FRAP was used to quantitatively assess (iv)the long-range continuity of the BCP microdomains (see Chapter 8).[1]

In the next section, the SMT instrumentation is introduced, including the most essential experimental considerations for quantitative material characterization of the nanoscale structures using SMT (*vide supra*). Then previous applications of SMT are briefly discussed, highlighting the advantages of SMT for material characterization.

3.2.2.2 Instrumentation in SMT

Widefield Illumination. SMT measurements are most often performed on a widefield fluorescence microscope.[17,18] A typical setup is shown in **Figure 3.4**.[18] Such a microscope commonly consists of a light source such as a laser, suitable optics including optical filters, a dichroic mirror or polarizers, a high magnification objective lens and a sensitive CCD-camera for detection of the signal. During the SMT experiment, a laser is directed through appropriate optics before it is focused into the sample through an objective lens. The emitted fluorescence of single probe molecules is in turn collected by the same objective lens and is transmitted through the dichroic mirror before finally being detected by an electron-multiplying (EM) CCD-camera.

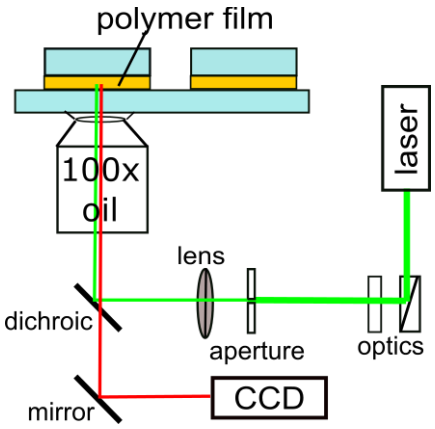

Figure 3.4. Schematic of widefield microscope used for wide-field single molecule imaging.

Importantly, this setup has two major advantages as compared to a confocal microscope.[138] First, it permits the dynamics of many single molecules within nanoscale structures to be recorded simultaneously for µm-scale wide sample areas (e.g. 30 µm x 30 um). For such purposes, the samples are broadly illuminated overr a relatively wide area using an objective lens with a high numerical aperture (*NA* = 1.3 – 1.5) and magnification (80-100x). A high *NA* of the objective lens is essential for an efficient collection of the relative weak emitted fluorescence of individual fluorescent probe molecules. High magnification is used to faciliate their detection as diffraction-limited spots of appropriate size. The second advantage of the widefield setup includes the data recording via a new generation of highly-sensitive CCD-cameras, which affords the high-speed data collection (up to 100 frames per sec for smaller readout areas of CCD) and with sufficiently

high sensitivity (and thus high S/N). This allows for tracking fast moving probe molecules at high S/N.

Conventional widefield and TIRF mode. All SMT measurements in the present study were conducted on an epi-fluorescence microscope in which the same objective was used for excitation and simultaneous collection of the single molecule fluorescence.[17,18] The main advantage of this mode is the lower background intensity as compared to the transmission mode caused by the incoming laser beam and non-ideal optical filters.[138] However, in the epi-fluorescence mode, the laser beam also penetrates across the entire film thickness, which results in higher background signal due to out-of focus fluorescence from larger depth of the sample.[138] This mode is suitable only for thin films or samples with limited thickness because thicker samples frequently produce high fluorescence background in the SMT data, thus decreasing its S/N ratio. Fortunately, TIRF can be used for thicker films because the probe molecules' excitation occurs only close to the glass-sample interface, reducing the background fluorescence intensity (**Figure 3.5**). In TIRF, the laser beam is adjusted to strike the glass-sample interface at an angle, larger than the critical angle (θ_{crit}), leading to its total internal reflection when the refractive index of sample (n_s) is smaller than that of the glass (n_g): $n_s < n_g$.[138,171]

$$\theta_{crit} = \arcsin\left(\frac{n_s}{n_g}\right) \quad \text{(Eq. 3.3)}$$

At the same time, the presence of an evanescent wave can be observed at the glass-sample-interface. This is in turn used for the fluorescence excitation within a nm-scale thin layer adjacent to the underlying substrate, primarily limited by the penetration of the evanescent wave into the media. The penetration depth of the evanescent (d_p) wave can be estimated using:[171]

$$d_p = \lambda/4\pi\sqrt{n_g^2 sin^2\theta - n_s^2} \quad \text{(Eq. 3.4)}$$

where λ is the wavelength of the light source. Typically, d_p is between 30 to 300 nm depending on the incident angle (θ).[172] For the SMT measurements in CF-PS-*b*-PEO sandwich film of µm-scale thickness, perfect TIRF mode could not be obtained because of $n_s \approx n_g$. Instead, the SMT data were recorded under a quasi-TIRF which permits the background fluorescence to be reduced due to a shorter penetration of the beam through the sample.[173] For thin films, TIRF measurements

are not required because the film thickness is less than the focal length (*ca.* 1 μm for 100x) of the objective lens. Thus, little background fluorescence from out-of-focus region contributed to the observed background intensity.

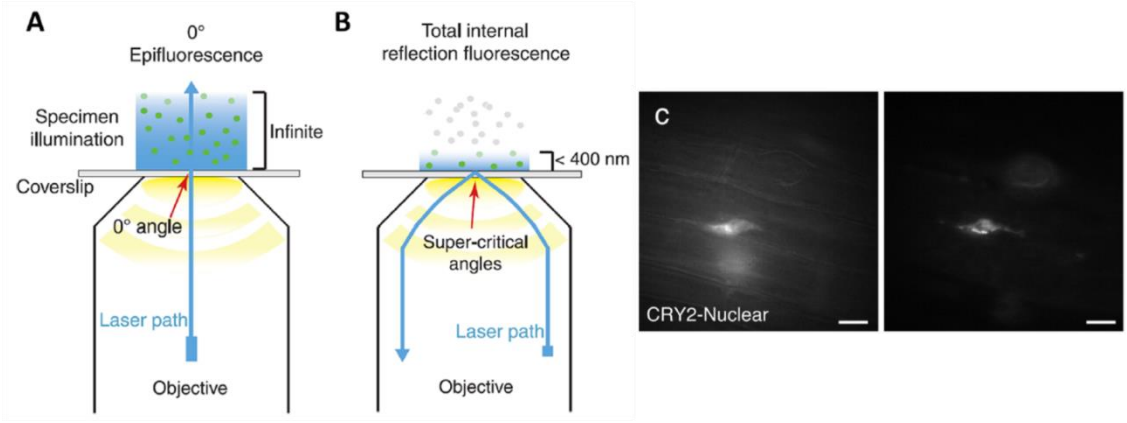

Figure 3.5. Schematic of (a) epi-fluorescence and (b) objective-based TIRF imaging mode. (c) A typical fluorescence image of cell recorded using epi-fluorescence (left) and TIRF mode (right).[174] Reprinted with permission from Ref (174). Copyright 2012, The Royal Society of Chemistry.

Spatial Calibration. In the SMT measurements, the fluorescence of each of the single molecules is detected by the CCD-camera as round spots on a dark background. Due to diffraction of light, the radius (r) of the spots is limited by

$$r = \frac{0.61\lambda}{n\sin\theta} \qquad \text{(Eq. 3.5)}$$

where λ is the wavelength of the laser (488 -532 nm in this study) and $n\sin\theta$ is the numerical aperture ($NA = n\sin\theta$) of the objective lens (in the present work: $NA = 1.49$). From this relationship, it is clear that the width of a fluorescent spot is approximately 300 nm. Importantly, for the detection of a single molecule in the SMT data, the diffraction-limited spots are fitted to a 2D Gaussian function as represented by a point-spread function (PSF). It has been shown that a spot comprising of 3-4 pixels in diameter can be fitted most accurately.[138] This required appropriate optics with a pixel size of approximately 100 nm. In our SMT studies, pixel size was adjusted to be 125 nm and 177 nm for the diffusion measurements in CF-PS-*b*-PEO and STMS films.[1,22-24] The calibration of the pixel size was performed on a thin film containing polystyrene bead with a

nominal size of 1 μm in diameter. Measuring the cross-sectional fluorescence intensity of an array of fluorescent beads provided a calibration value for pixel-length relationship.

Choice of Fluorescent Probe Molecules. The choice of fluorescent probe molecules is of tremendous importance for SMT measurements since these molecules directly probe and explore the environment and nanostructure properties of the materials.[17] So far, the majority of studies have employed fluorescent-labeled biomolecules (DNA, proteins and lipid molecules),[19,175] quantum dots/rods[176] and most importantly fluorescent dyes as tracer molecules.[20,165,177] Fluorescent probe molecules are chosen based on several criteria. First, they should have a high fluorescence quantum yield. Commonly, fluorescent dye molecules exhibit a high quantum yield of 0.04 – 1, but this can be highly dependent on the chemical environment (e.g. organic solvent), temperature and excitation wavelength. Secondly, the fluorescent probe molecules should be photostable, offering a long (ideally >1min) life time prior to photobleaching for SMT measurements. In fact, SRB has a high quantum yield of 0.34 in ethanol and a high photostability.[178] Furthermore, fluorescent probe molecules are chosen based on their ability to probe steric, electrostatic and hydrophobic interactions. Thus, the molecular lengths[150,179,180] and charge[179,181,182]of the probe molecules have been frequently varied in a series of SMT measurements.

In the present work, two different fluorescent dye molecules were used to account for the different chemical environment of the cylindrical nanostructures in STMS and CF-PS-*b*-PEO films. For SMT measurements in a STMS film, a hydrophobic C_{11}OPDI dye molecule (see Figure 3.6b) was used because it preferentially partitions into the cylindrical hydrophobic mesopores due to hydrophobic effects.[22] Thus, these single molecules are used as reporters for hydrophobic interactions within the nanoscale pores in addition to the local information on the material characteristics of the nanopores. For the SMT measurements in phase-separated CF-PS-*b*-PEO films, a negatively charged SRB dye (see **Figure 3.6a**) was employed as it preferentially partitioned into the cylindrical PEO microdomains.[23,24] The partitioning is mainly driven by complexation between the sodium countercation of SRB with the PEO domains.[183] Therefore, SRB dye molecules can be used for investigations of the structural and mass-transport properties of molecules in the cylindrical microdomains. Careful selection of the suitable tracer molecules depends upon the objective of the study.

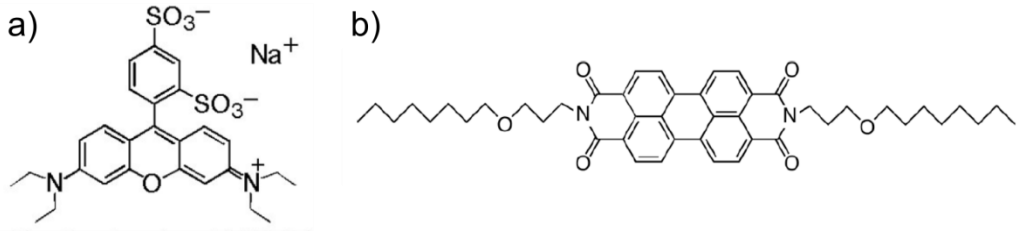

Figure 3.6. Chemical structure of a) SRB and b) C_{11}OPDI fluorescent dye molecules.[22,23] Reproduced with permission from ref [22, 23]. Copyright 2011, The Royal Society of Chemistry. Copyright 2012, The American Chemical Society.

Automated Spot Detection and Linking in Trajectories.[22] The tracking of single molecules across multiple video frames requires initial detection of individual molecules (i.e., as single fluorescent spots) and determination of their positions in each frame. The individual molecules appearing in the sequence of video frames must then be linked into trajectories. Molecule detection and position determination can be accomplished by any of a number of published methods.[184-186] Molecular position can often be determined to a precision well beyond the diffraction limit (i.e., ~$\lambda/2$), with localization precision as small at ~ 5-10 nm reported under relatively high, but common, signal-to-noise levels in SMT experiments.[139,140,149,187] In the present work, molecule detection, validation and position determination were accomplished using methods reported by Sbalzarini and Koumoutsakos[184] and implemented in an ImageJ plugin.[188]

The linking of fluorescent spots in video frame sequences has been accomplished previously by manual[151] and semi-automated[189,190] procedures, the former relying largely on human judgment. Manual linking was precluded in the present studies by the need to analyze large numbers of trajectories. Fully automated linking was instead employed and was accomplished by implementation of modified literature-based methods.[184] In these methods, a linear cost functional (Eq. 3.6)[184] is defined and subsequently minimized to determine frame-to-frame associations of individual fluorescent spots. The cost, ϕ of linking spot j in frame t to spot k in frame t+1 was initially determined by:

$$\phi_{jk}(t,t+1) = \left(x_j(t) - x_k(t+1)\right)^2 + \left(y_j(t) - y_k(t+1)\right)^2 \qquad \text{(Eq. 3.6)}$$

in which (x_j, y_j) represents the x, y position of spot j. The cost functional was evaluated globally, for all pairs of spots during initial spot linking.

After initial construction, the trajectories were subsequently refined by iteration through the spot linking process using a variant of the previous cost functional:[191]

$$\phi_{ijk}(t-1,t,t+1) = \left(x_i(t) - x_j(t+1)\right)^2 + \left(y_i(t) - y_j(t+1)\right)^2 + w\left(1 - \frac{\left(\left(x_i(t-1) - x_j(t)\right)\left(x_j(t) - x_k(t+1)\right) + \left(y_i(t-1) - y_j(t)\right)\left(y_j(t) - y_k(t+1)\right)\right)^2}{\left(\left(x_i(t-1) - x_j(t)\right)^2 + \left(y_i(t-1) - y_j(t)\right)^2\right)\left(\left(x_j(t) - x_k(t+1)\right)^2 + \left(y_j(t) - y_k(t+1)\right)^2\right)}\right) \quad \text{(Eq. 3.7)}$$

The new term in Eq. 3.7 represents the quantity ($1\text{-}\cos^2\delta\theta$), where $\delta\theta$ is the change in direction of molecule motion required to link three spots in three consecutive frames, and w is a weighting factor, empirically set to 2 in the present implementation. Application of Eq. 3.7 during the spot linking process effectively dissociates trajectories incorporating two or more 1D segments into separate 1D trajectories. In the present works, the resulting 1D trajectory segments are used to visualize and quantify trajectory orientation and thus the 1D nanostructures. Distribution data of the trajectory angles provide valuable means to quantitatively assess the order of the nanostructures in local sample regions.

3.2.2.3 Previous Applications of SMT

Measurement of Diffusion Coefficients. In the absence of external forces, the trajectory data provide a means for estimating single-molecule diffusion coefficients in local sample regions.[192] The distribution of single-molecule diffusion coefficients permits material heterogeneities to be assessed via the histogram width as previously reported.[55,56,149,150,193] Such variation is likely attributable to the local fluctuation in size and organization of the nanostructures if the solvent content in the materials was well-controlled. As reported, the organic solvent (e.g. chloroform) vapor has been shown to induce and facilitate the mobility of terrylene molecules in the silica nanopores.[149] The author explained such observation through solvation of probe molecules under chloroform atmosphere, preventing their strong adsorption to the active silanol sites of the nanopore walls.

For nanostructured materials with well-controlled solvent level, the distribution of the probe molecules' diffusion coefficients offers important means for characterization of the materials. Park and coworkers, for example, measured the diffusion coefficients of single OPPDI dye molecules in flow-aligned CTAB templated silica monoliths.[55] The histogram of the diffusion coefficients was broadly distributed over a large range of values, thus suggesting local variation of the mesopore properties such as size and organization. Interestingly, the average of the single molecule diffusion coefficients remains similar regardless of the aging time of the injected sol, indicating that probe molecules explore the nanoscale pores, unaffected by cross-linking of the silica matrix.[55]

Visual Evidence of Material Heterogeneities and Defects. SMT methods are now being widely employed to visualize the diffusion of probe molecules in well-organized 1D nanostructures but also within heterogeneous regions containing rare sites and defects. For example, Werley and Moerner revealed the presence of ~ 200 nm wide cracks in the crystals that guide and restricted the diffusive motions along one-direction.[163] Importantly, the measured diffusion coefficients of terrylene molecules exhibited a significant reduction as compared to the bulk values, consistent with strong interactions of probe molecules with the crack walls. In several other studies by the Brauchle group[20,149,162] and others,[165,177] the diffusion of single molecules have revealed the presence of interconnected pores, dead ends and curved segments of a 1D nanostructure as represented by two neighboring trajectory segments, shorter and curved trajectories. [162] The ability of SMT for single molecule detection with a high precision makes it valuable for characterization of defects and material heterogeneities.

Assessment of Continuity and Accessibility of Nanostructures. More recently, the continuity and accessibility of 1D nanostructures for relatively large dye molecules was also investigated using SMT methods, providing complementary data to high resolution TEM methods. In pioneering work, Zürner, et al. followed the diffusion of fluorescent terrylene molecules in surfactant-templated 1D silica nanopores.[162] Interestingly, the single molecule trajectories were directly correlated to cylindrical nanopores measured by TEM in identical samples regions. The results showed that probe molecules could follow open 1D nanochannels over μm-length scales, crossed between neighboring channels, were trapped in dead ends and followed curved

nanochannels, consistent with disordered structures of the film. [162] All of these observations therein suggested the presence of open, continuous nanopores as well as defects and rare sites in the materials that were challenging to be detected by other experimental techniques.

SMT studies of diffusion are not limited to nanoscale pores but also have been previously employed to probe the diffusion of fluorescent probe molecules within cylindrical polybutadiene (PB) microdomains in a cylinder-forming poly(ethylene oxide)-polybutadiene diblock copolymer film.[165] The single-molecule trajectories represent the diffusive motions of tracer molecules confined along PB microdomains over a μm-scale distance, in agreement with AFM images of the same film. The results of these studies demonstrated the utility of SMT methods for assessment of the local continuity of the nanostructures and their accessibility for molecules over several micrometers.

Limitations of SMT. However, SMT cannot probe longer-range (>10 μm) material characteristics because of the limited photostability of the fluorescent probe molecules. The probe molecules tend to photobleach before they can explore the entire length of individual nanostructures. One fluorescence method capable of investigating molecular transport over wider sample regions is FRAP. Since its development more than 40 years ago, FRAP has been widely employed to explore the transport of molecules in various biological materials and others. [146] FRAP affords measures of the spatially-averaged diffusion coefficients of many molecules over a longer-range (>10 μm) as a result of the fluorescence recovery of a small (μm -scale) photobleached region. It is also a simple and straight forward method and has found wide applications in various fluorescence microscope systems. Thus, it can be integrated in a wide-field fluorescence microscope as used for SMT measurements in our study (Chapter 8). One major advantage of this setup is the ability to conduct FRAP and SMT measurements in identical sample areas, permitting complementary information on molecular diffusion within confined nanostructures to be quantitatively assessed. Importantly, FRAP measurements provide a quantitative measure of long-range continuity of the aligned PEO microdomains in CF-PS-*b*-PEO films. In the next section, the FRAP method is introduced along with its instrumentation and important applications.

3.2.3 Fluorescence-Recovery After Photobleaching (FRAP)

Since its development in the 1970s by Webb and coworkers, FRAP has been one of the most powerful and popular analytical methods for measuring molecular mobility in small (<1mm) sample regions of biological materials such as cells, lipid bilayers and cell surfaces.[146] Recently, FRAP has also been employed for studying mass-transport in nanostructured materials such as in cylindrical organic nanotubules or carbon nanotubes.[194-196] In FRAP, the data are collected based on user-defined photobleaching of fluorescent probes at a small sample region and by subsequent monitoring of the gradual fluorescence recovery in the bleached area. The rate and extent of the recovery allowed the mass-transport rate and the fraction of mobile and immobile molecules to be determined, respectively.[146] Visual inspection of the recovery pattern also affords valuable information on the dimensionality of mass-transport. The main advantage of FRAP is its simplicity and applicability for a large number of different samples as long as the molecular mobility is high enough, and more importantly, occurring along a sufficiently long distance (> 10 μm). In the next section, the instrumentation of FRAP is described along with essential features and important concepts behind these. Next, relevant applications of FRAP in biological materials and nanostructures are highlighted. Then, limitations of ensemble methods in general and FRAP are summarized.

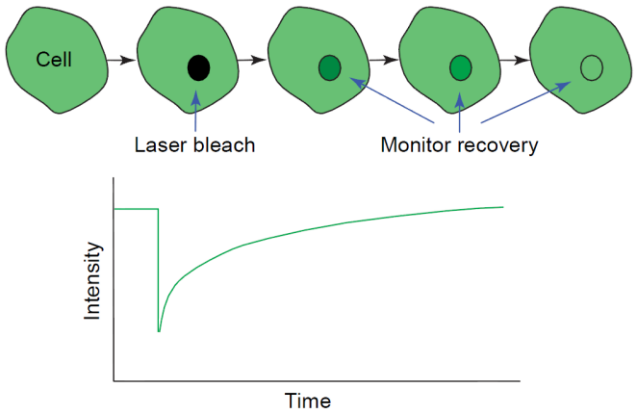

Figure 3.7. Schematic of a FRAP experiment involving the photobleaching using an intense laser pulse and subsequent fluorescence monitoring at the same area. The time dependence of the fluorescence intensity is used to estimate the diffusion coefficient.[197] Reprinted with permission from Ref (197). Copyright 2004 Elsevier Ltd.

Instrumentation. FRAP measurements are now being widely performed on a confocal fluorescence microscope which commonly comprises a laser source, an high-NA objective lens, a piezo-scanning stage, a pinhole, a detector (photomultiplier tube or avalanche photo diode) appropriate optics and filters. Experimentally, the photobleaching of a well-defined sample region is accomplished by focusing an intense laser beam with narrow diameter (ideally diffraction-limited) through a high-NA objective lens on the sample. This requires the utility of a small pinhole for shaping the incoming broader laser beam down to one with a diffraction-limited size. In earlier FRAP studies, the photobleaching pattern was commonly circular due to limited sample or scanning abilities of the stationary laser source in the instrument.[198] More recently, various photobleaching pattern including stripes, ellipses or circles have been employed in FRAP measurements for studying 1D and 2D mass-transport, respectively.[199] Choosing the suitable pattern is important because it permits an analytical equation to be derived, simplifying the quantitative data analysis.

For monitoring the fluorescent recovery from the same area upon photobleaching, the sample is systematically scanned via a piezo-scanning-stage using a laser with significantly weaker intensity. This attenuated (e.g. 1000 times weaker than at photobleaching) laser is aimed to prevent excessive photobleaching during data recording. The fluorescence emission is collected by the objective and directed through a pinhole and onto a detector (commonly an APD). The use of a pinhole permits the detection under low background conditions. All out-of-focus fluorescence intensity can be effectively excluded which is highly essential for obtaining FRAP data with a high signal to noise ratio.

Recently, FRAP experiments have been conducted on a widefield fluorescence microscope which allowed the fluorescence intensity to be observed for a µm-scale wide sample area.[1] Scanning of the sample is not required for this setup. Thus, the data collection is in general significantly faster than using the confocal microscope making it more suitable for observing and measuring of higher probe molecule mobilities.[1] The disadvantages of wide-field FRAP include the limited control of photobleaching size and pattern. As in this work, photobleaching occurred for a circular region of several microns in width, primarily governed by the stationary sample or laser source. Furthermore, the diameter of the photobleached region is larger as compared to confocal FRAP due to the widefield illumination mode, excluding its utility for smaller µm-size samples such as short organic nanotubes.

Applications of FRAP. FRAP have been widely employed to study molecular transport in biological materials including cells, on cell surfaces, phospholipid membranes an lipid bilayers just to name a few.[198] It measures the spatially-averaged diffusion behavior of many molecules at the same time, providing their average diffusion coefficients but also the fraction of mobile and immobile molecules.[146] More recently, FRAP has also been employed to study the binding phenomena in biological systems, allowing a binding constant to be extracted when an appropriate diffusion-binding model has been applied for the data analysis.[197] More recently, the diffusion coefficients (*D*) of fluorescent dyes have been measured in 1D nanostructured materials using FRAP. The Gai group reported a position dependence of *D* in 30-40 μm long lipid tubules, revealing heterogeneities of the materials.[194] Likewise, Okamoto and coworkers measured the ensemble D of dye molecule diffusion within shorter (<10 μm) silica nanotubes, revealing heterogeneous diffusion dynamics through a broad distribution of D values obtained from multiple measurements.[195] These studies show that FRAP can probe the more localized mass-transport and material properties in a um-scale sample region as compared to flux measurements or NMR methods.

Strengths and Limitations of FRAP. Despite its usefulness in providing valuable information on mass-transport phenomena for cylindrical nanostructured materials, FRAP shows several significant limitations. First, the transport of molecules in the material in general reflects the spatially-averaged mass-transport dynamics of many molecules within multiple structures. Little is known about the local, μm-scale mass-transport and material properties. Important detailed information involving spatial and temporal transport heterogeneities is frequently obscured by ensemble averaging of the data. Second, the mass-transport dynamics of molecules within the nanostructures cannot be explicitly observed by FRAP. It can indirectly be understood from the recovery of the fluorescence in the photobleached regions, consistent with molecular transport in the materials. As for an ensemble method, it fails to provide a more detailed spatially and temporally-resolved picture of how molecules diffuse at different locations in the nanostructures. Because of the above mentioned limitations, the mass-transport within 1D nanostructured materials have been more recently explored using single molecule methods including important advantages as described above (*vide supra*).

Chapter 4 - Trajectory Angle Determination in One Dimensional SMT Data by Orthogonal Regression Analysis

Reproduced with permission from The Royal Society of Chemistry.
Published as: Tran Ba, K. H., Everett, T. A., Ito, T., Higgins, D. A. *Phys. Chem. Chem. Phys.* **2011**, *13*, 1827-1835.

4.1 Introduction

This chapter describes the utility of the orthogonal regression analysis for analysis of 1D single-molecule trajectory data, reflecting the motion of single molecules and particles along approximately linear (i.e., 1D) diffusion trajectories in nanostructured materials.[200-203] The results obtained provide a quantitative assessment of the in-plane orientation of individual trajectories. Variations in their orientations within selected sample regions serve as a proxy for determining local materials order via an order parameter $\langle P \rangle$ which reflects the average deviation of individual trajectories from the mean trajectory orientation in a given sample region. Estimates of the error in each trajectory angle and in single molecule positioning are also obtained, along with the variances in molecular position of mobile molecules along the individual trajectories. The former provides a quantitative means to distinguish 1D diffusing molecules from those diffusing in 2D or are immobile. The positioning error provides an estimate of the spatial resolution and, along with the motional variance along the trajectory; an alternative means to distinguish 1D and 2D/immobile trajectories. Demonstration and validation of this method was achieved by applying it to the analysis of single-molecule trajectories in already well-characterized mesoporous silica thin films incorporating cylindrical channels.[147-150,204-207] Our method is broadly applicable to analysis of diffusion in other 1D nanomaterials such as phase-separated block copolymers[165] and silica nanotubes.[195] It is also applicable in studies of biological samples, and could be used to assess myosin motion along actin filaments,[208] kinesin motion along microtubules,[209] the motions of macromolecules,[210] cells[211] and vesicles[212] as they follow surface gradients, or the directed motion of particles within cell membranes.[213] In all cases, the results of this analysis will provide a more quantitative data on associated diffusion coefficients, trajectory angles, angle distributions and errors therein.

4.2 Experimental Section

4.2.1 Sample Preparation

Sols for the preparation of surfactant-templated silica thin films were prepared as described previously.[214,215] Briefly, these were obtained by mixing tetramethoxysilane (TMOS, 99%, Aldrich), deionized water (HPLC grade, Acros), absolute ethanol (200 proof, HPLC grade, Sigma-Aldrich) and HCl (ACS grade, Fisher Scientific) in a small vial. After addition of the above components, the sol was stirred for 1 h and was then allowed to age for an additional 24 h at room temperature in a dessicator. Cetyltrimethylammonium bromide (CTAB, Aldrich) was then dissolved in the sol by vigorous stirring for 1 h. The final molar ratio in the sols was typically 1:49.1:0.01:12.3:0.2 for TMOS, ethanol, HCl, H_2O and CTAB, respectively. Dye-doped mesoporous silica films were prepared by adding an isopropanol solution of bis-N,N'-(octyloxypropyl)perylene-3,4,9,10-tetracarboxylic diimide (OPPDI) to a portion of the above sol to yield a total dye concentration of 2 nM. OPPDI was synthesized by following previously-described procedures.[216,217] Its structure is shown in **Figure 4.1**.

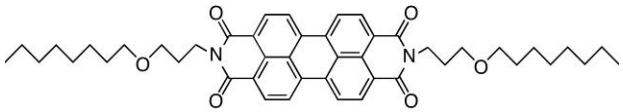

Figure 4.1. Chemical Structure of bis-N,N'-(octyloxypropyl)perylene-3,4,9,10-tetracarboxylic diimide (OPPDI) used as the fluorescent tracer in SMT experiments. Reprinted with permission from Ref (22). Copyright 2011 The Royal Society of Chemistry.

Film deposition was accomplished by a method previously termed "vertical spin coating" in which the sample was spun along an axis parallel to the substrate plane.[218] In this procedure, ~ 100 µL of sol was spin cast (30s at 10,000 rpm) onto a plasma cleaned glass coverslip (Fisher Premium) immediately after addition of dye to the sol. The films were subsequently dried overnight at room temperature in a dessicator before the experiment. The mean film thickness of the prepared films was determined to be 180 ± 20 nm by spectroscopic ellipsometry (α-SE, J. A. Woollam). Surface profilometry measurements (XP-2, Ambios Technology) were used to confirm the film thickness obtained by ellipsometry and to quantify root-mean-square surface roughness,

which was found to be 9 ± 3 nm. The latter value provides important confirmation that the films are continuous.

The presence of hexagonally-ordered cylindrical mesopores in the films was confirmed by X-ray diffraction (XRD).[206,214] X-ray measurements were performed on a Bruker D8-Advance powder X-ray diffractometer using Cu Kα-radiation (40 KV, 40 mA) at 1.54 Å with a 0.05° step size and a 3 s step time. A representative XRD data is shown in **Figure 4.2**.

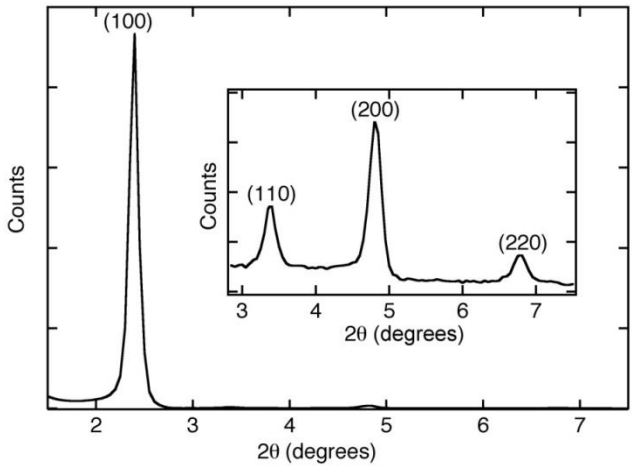

Figure 4.2. Typical X-Ray diffraction data from a surfactant-templated mesoporous silica film. The X-ray pattern is consistent with a hexagonal structure having characteristic (100) and (200) peaks at 2θ = 2.35° and 4.75°, respectively. Small intensity (110) and (220) peaks indicate that the sample also incorporates a small degree of 3D hexagonal or cubic symmetries. The inset depicts the (110), (200) and (220) peaks from the sample. Reprinted with permission from Ref (22). Copyright 2011 The Royal Society of Chemistry.

4.2.2 Instrumentation

All SMT studies were conducted on a wide-field fluorescence microscope as introduced in **Chapter 3**. This system is built on an inverted epi-illumination microscope (Nikon Eclipse Ti), which was supported on a pneumatic vibration isolation table. Light from a blue diode laser (488 nm) was used to excite the dye molecules. Prior to incidence on the sample, the laser light was passed though appropriate band-pass filters and polarization optics. Both linear and circularly-polarized light were employed in separate experiments. Linearly polarized light was produced by use of an appropriate polarizer and 488 nm half-wave plate (Special Optics). Circularly polarized light was obtained by inserting a 488 nm quarter-wave plate (Special Optics) into the beam path, with its optical axis rotated 45º from the incoming polarization. For uniform illumination of the sample, the laser light was also passed through a diffuser. It was subsequently reflected from a dichroic beamsplitter (505 nm cutoff) and into the back aperture of an oil-immersion objective (Nikon Apo TIRF 100x, 1.49 N.A.). The incident laser power was maintained in the 0.5 – 1 mW range (estimated from measurements made just prior to the dichroic beamsplitter). An electronic shutter was used to control sample illumination. Fluorescence from the film was collected in reflection and was separated from the excitation light by passage back through the dichroic beamsplitter and appropriate bandpass (550 nm passband center wavelength, 40 nm width) and long-pass (515 nm cutoff) filters. A back-illuminated EM-CCD camera (Andor iXon DU-897) was used as the detector.

Wide-field movies were recorded as 100 frame videos with 0.33 s exposure times per frame. The image size was 512 pixels x 512 pixels, corresponding to an 87 μm x 87 μm (1 pixel = 0.17 μm) region in the sample. 1D diffusion in large ordered domains was only observed in previous studies after exposure of the films to high humidity environments.[149] Therefore, prior to the recording of videos, the samples were hydrated for 1 h at a relative humidity (RH) of ~70 % and/or imaged under a mixture of ethanol and water vapor. The same RH atmosphere was maintained throughout all experiments.

4.2.3 Trajectory Analysis

Orthogonal Regression Analysis of Trajectories. The tracking of single molecules across multiple video frames requires detection of individual molecules (i.e., as single fluorescent spots), determination of their positions in each frame, and finally, linking of the individual fluorescent spots into trajectories. The method employed is described in detail in **Chapter 3.3.2** and effectively dissociates curved trajectories and those incorporating multiple 1D segments into separate 1D trajectories. Quantitative analysis of individual trajectory segments was accomplished by implementation of orthogonal linear regression methods.[201-203] This analysis provides the "best fit" (x,y) positions of the molecule being tracked in each trajectory, the orientation of the 1D trajectory segment (in the film plane), and estimates of errors in these parameters. Common least squares regression methods cannot be employed because they implicitly neglect errors in the x data.

The orthogonal regression procedure assumes both x and y positions are measured to similar levels of precision. Single molecules are assumed to take a random walk in 1D about their mean position (x=0, y=0). The measured position (x_i, y_i) is then defined by:

$$\begin{aligned} x_i &= R_i \cos\theta + \delta_i \\ y_i &= R_i \sin\theta + \delta_i \end{aligned} \qquad \text{(Eqs. 4.1)}$$

where R_i represents the actual (i.e., error free) position along the 1D trajectory, θ the angle (-90° – 90°) of the trajectory segment with respect to the x axis (horizontal direction) in the video frames, and δ_i the error in measuring the position of the molecule. The mean position of each molecule is defined as $\langle R \rangle = 0$.

To facilitate development of the regression equations, Eqs. 4.1 may be rewritten as:

$$\begin{aligned} x_i &= X_i + \delta_i \\ y_i &= X_i \tan\theta + \delta_i \end{aligned} \qquad \text{(Eqs. 4.2)}$$

where X_i represents the best estimate of the actual x position of the molecule. The best-fit line ($Y_i = X_i \tan\theta$) yields the minimum total error between the measured data points and the line, with the error determined along the normal drawn from each point to the fitted line. The best estimates of the actual molecule positions are represented by:

$$X_i = \frac{x_i + y_i \tan\theta}{1 + \tan^2\theta}$$
$$Y_i = \frac{x_i + y_i \tan\theta}{1 + \tan^2\theta}\tan\theta \qquad \text{(Eq. 4.3)}$$

The best-fit line is obtained by finding $\tan\theta$ for which the sum of the squared residuals (SSR) between x_i and X_i, and y_i and Y_i, is at a minimum:

$$\text{SSR} = \frac{1}{n}\sum_{i=1}^{n}\left[(x_i - X_i)^2 + (y_i - Y_i)^2\right] = \frac{1}{n(1+\tan^2\theta)}\sum_{i=1}^{n}(y_i - x_i\tan\theta)^2 \qquad \text{(Eq. 4.4)}$$

By setting the derivative of SSR with respect to $\tan\theta$ equal to zero and solving, $\tan\theta$ is found to be:

$$\tan\theta = \frac{(S_{yy} - S_{xx}) + \sqrt{(S_{yy} - S_{xx})^2 + 4S_{xy}^2}}{2S_{xy}} \qquad \text{(Eq. 4.5)}$$

where

$$S_{yy} = \frac{1}{n}\sum_{i=1}^{n} y_i^2,\ S_{xx} = \frac{1}{n}\sum_{i=1}^{n} x_i^2 \text{ and } S_{xy} = \frac{1}{n}\sum_{i=1}^{n} x_i y_i \qquad \text{(Eq. 4.6)}$$

The large sample approximation has been employed in defining Eqs. 4.6, greatly simplifying the derivation of the error expressions given below.[202] In the present work, only data from trajectories ≥ 25 frames in length are employed in the analysis.

The variance in the position measurement for each molecule (i.e., the errors in determining x_i and y_i) along each trajectory is given by:[202,203]

$$\sigma_\delta^2 = \frac{S_{yy} - 2S_{xy}\tan\theta + S_{xx}\tan^2\theta}{1 + \tan^2\theta} \qquad \text{(Eq. 4.7)}$$

Eq. 4.7 provides an estimate of the positioning error across the entire length of the trajectory. Errors in locating each molecule arise in part from finite noise levels in the fluorescence profile of its associated spot.[140,187] However, the positioning error across the full trajectory length also includes errors from real deviations in the molecular position from a 1D trajectory. As shown by Brauchle, et al., single molecules diffusing through mesoporous silica occasionally cross between neighboring channels.[147] Furthermore, individual trajectories are likely to deviate from perfect

linearity due to deviations (i.e. subtle bends and kinks) in the channels. Such behaviors are manifested as increased measurement error in the present model. As a result, σ_δ^2 actually reflects the total deviation of each trajectory from a 1D model.

The variance in the tangent of the estimated trajectory angle can also be determined:[202,203]

$$\sigma_{\tan\theta}^2 = \frac{\sigma_\delta^4 \tan^2\theta + S_{xy}\sigma_\delta^2 \tan\theta\left(1+\tan^2\theta\right)}{nS_{xy}^2} \qquad \text{(Eq. 4.8)}$$

where *n* is the number of data points in each trajectory segment. The error in the trajectory angle, σ_θ, is then obtained by further manipulation of Eq. 4.8:

$$\sigma_\theta = \sigma_{\tan\theta}\cos^2\theta \qquad \text{(Eq. 4.9)}$$

Application of Eqs. 4.8 and 4.9 to individual trajectories (see below) provides a useful means for distinguishing 1D trajectories from those of 2D-diffusing and immobile molecules.

Trajectory Angle Order Parameter. Deviations in the individual trajectory angles from the mean orientation of trajectories within a given sample region affords an important quantitative measure of the degree of trajectory alignment. A ubiquitous order parameter employed in systems of spherical symmetry is the average of the second Legendre polynomial $\left\langle P_2(\Delta\theta)\right\rangle$,[219] where $\Delta\theta = \bar{\theta} - \theta$ and $\bar{\theta}$ represents the mean trajectory orientation in a given sample region. Here, we employ its 2D analog:

$$\langle P\rangle = 2\left\langle\cos^2(\Delta\theta)\right\rangle - 1 \qquad \text{(Eq. 4.10)}$$

in which the average represented by $\langle\ \rangle$ is taken over all trajectories in a selected population, region or sample domain. The value of $\langle P\rangle$ ranges from one for perfectly ordered populations to zero for totally disordered populations.

Quantitative Assessment of Single-Molecule Populations. In this study, single molecule populations were distinguished and separated based on a threshold value in the trajectory angle error. Such value was obtained from the simulated wide field videos using custom simulation software written in the National Instruments LabView programming environment. In these simulations, molecules were first positioned at random throughout the simulated region. Molecular diffusion was simulated by selecting the frame-to-frame step size (and direction) for each molecule from a Gaussian distribution (in each dimension) having a variance of $2Dt$. Here, t is the frame time (0.33 s) and D the diffusion coefficient of the mobile species. Each video was 100 frames in length. Videos simulating both 1D and 2D diffusion incorporated 100 molecules in a 43.5 μm x 43.5 μm region. Each molecule was assigned a lifetime (i.e., time to photobleaching), generated at random from an exponential distribution having a mean lifetime of 13 s. To maintain a constant concentration of molecules in the simulated region, bleaching of one molecule triggered positioning of a new molecule at a random position. For 2D simulations, each molecule was assigned a diffusion coefficient of $3x10^{-12}$ cm^2/s to properly model the experimental data, which depicts very slow diffusion for this population (see **Figure 4.12**). Simulations of 1D molecular motion employed a diffusion coefficient of $3x10^{-10}$ cm^2/s. The S/N- ratio in the images was set to a value that closely approximated the experimental data. The simulated videos were analyzed in a manner identical to analysis of the experimental videos. **Figure 4.3A** depicts the distribution of trajectory angle errors obtained from three separate simulations of 2D-diffusing species. Appended to **Figure 4.3A** is a Log Normal fit to the data. This fit was used to determine the probability that 2D-diffusing molecules would be erroneously classified as 1D-diffusing. As described in the main text, trajectories having $\sigma_\theta < 3.35^o$ were classified as 1D-diffusing molecules, while those with $\sigma_\theta \geq 3.35°$ were classified as 2D-diffusing or immobile molecules. The area under the Log Normal fit below the threshold was 5.5% of the total area under the curve, indicating a 5.5% error rate at which 2D trajectories will accidentally be classified as 1D trajectories. **Figure 4.3B** depicts the distribution of the trajectory variance ratio from the same data set and its fit to a Log Normal function. An error rate of 5.5% occurs in this data at a variance ratio of 0.197, the threshold value used for separation of 1D and 2D trajectories based on variance ratio data.

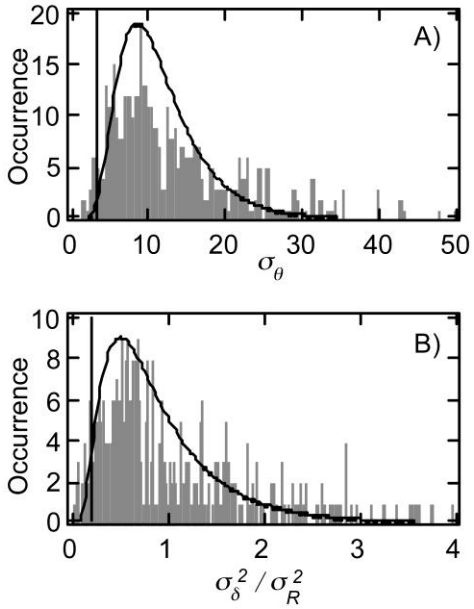

Figure 4.3. A) Distribution of trajectory angle error (σ_θ) derived from three simulated movies. Also shown is a Log Normal fit to the data (solid line). The latter was used to determine the error rate for a threshold of $\sigma_\theta = 3.35°$. B) Distribution of the trajectory variance ratio and Log Normal fit (solid line). The variance ratio threshold for distinguishing 1D from 2D-diffusing and immobile molecules was determined to be 0.197. Reprinted with permission from Ref (22). Copyright 2011 The Royal Society of Chemistry.

4.3 Results and Discussion

4.3.1 Observation of Single Molecule Motion in Mesoporous Silica Films

SMT data recorded on a wide-field fluorescence microscope were used to monitor the diffusion of single molecules in mesoporous silica thin films. **Figure 4.4A** shows a representative frame from one such data. Single OPPDI molecules appear as bright round diffraction-limited (250 nm in width) fluorescent spots. The majority of these spots is observed to move in from frame to frame and was linked into trajectories as described in Chapter 3. As we seek information on the orientation and degree of alignment of 1D trajectory segments, the automated procedure employed was designed to split trajectories exhibiting two or more linear segments into separate trajectories. **Figure 4.4B** plots all trajectories recorded in the SMT data. As is apparent from the trajectory data, a large number of linear (1D) trajectory segments are observed, with the majority oriented approximately along the horizontal direction on the image. In addition, SMT videos recorded under linearly-polarized excitation light demonstrate that the dye diffuses in an aligned state[149] through these regions (**Figure 4.5**).

The data depicted in **Figure 4.4A** were recorded under circularly-polarized excitation, allowing for efficient excitation and detection of all dye molecules oriented in the film plane. In contrast, SMT videos recorded under linearly-polarized excitation provide additional information on the orientation of molecules diffusing through the mesopores.[149] **Figures 4.5AB** depict representative frames from Videos 2 and 3 of identical sample regions recorded using orthogonal excitation polarizations. **Figures 4.5CD** plot the trajectories determined from each video and show that trajectories exhibiting 1D motion along the vertical direction appear when the excitation light is polarized along this direction. Likewise, trajectories oriented along the horizontal direction appear when the incident light is polarized along the horizontal direction. As the transition dipole associated with excitation of OPPDI by 488 nm light is known to be polarized along the molecular long axis (**Figure 4.1**),[220,221] it is concluded the dye diffuses in an aligned state, with its long axis oriented parallel to the local channel axis. Similar conclusions have been drawn for diffusion of terylene diimides in related materials.[149]

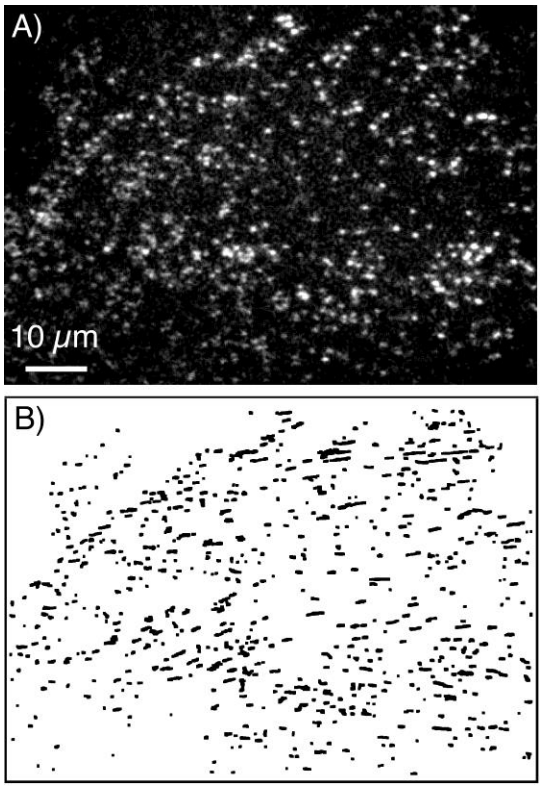

Figure 4.4. A) Representative frame of a 100 frame SMT video depicting single molecule motions in a CTAB templated mesoporous silica thin film. Fluorescence in this video was excited using circularly-polarized light. B) Trajectories depicting the motions of the individual probe molecules across the full 100 frames of the video. Reprinted with permission from Ref (22). Copyright 2011 The Royal Society of Chemistry.

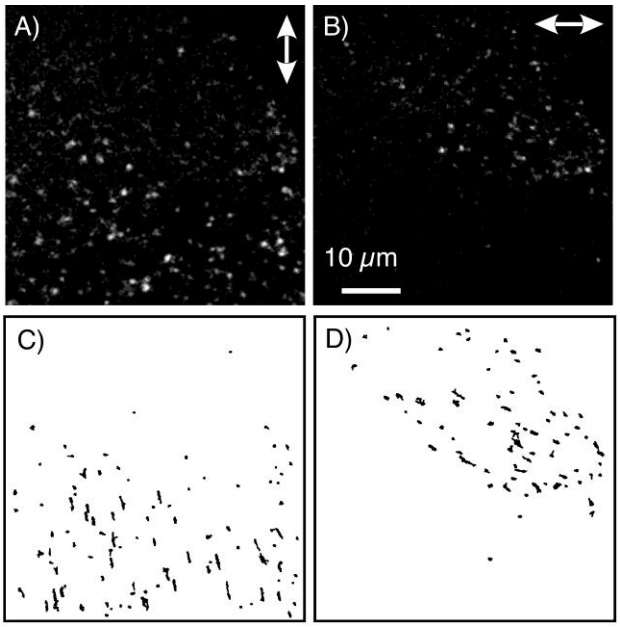

Figure 4.5. A) and B) Representative frames of two separate 100 frame videos recorded from identical regions of a surfactant-templated mesoporous silica thin film. Fluorescence in these videos was excited using linearly polarized light, as designated by the appended white arrows. C) and D) Trajectories depicting the motions of the individual molecules in these videos. To enhance trajectory visibility, only those ≥ 10 frames in length are shown. Reprinted with permission from Ref (22). Copyright 2011 The Royal Society of Chemistry.

4.3.2 Mesopore Alignment by Vertical Spin Coating

It is noteworthy that the mesopore orientation expected from the "vertical spin-coating" procedure[218] employed for sample preparation is along the horizontal direction (to within ~ ±10°). Unfortunately, collection of a large number of SMT data to date has shown no detectable preference, on average, for mesopore alignment along this direction. **Figure 4.6** presents another typical image of mesoporous silica films and associated trajectories obtained from a similar sample. This sample region shows clear evidence for the presence of at least two distinct grains having different (nearly orthogonal) trajectory orientations. Neither is oriented exactly along the expected direction (horizontal). These observations suggest that the surfactant micelles and mesopores form (or form ordered domains) only after most of the solvent has evaporated, and hence, are not aligned by the shear forces active during spin coating.

Confinement of molecular motion to 1D trajectories in these videos is attributed to entrapment of the molecules within cylindrical channels running through the mesoporous films.[147-149] XRD data (**Figure 4.2**) provides clear evidence for the presence of hexagonally ordered mesopores oriented in the film plane.[206,214] It is therefore concluded that the molecules exhibiting 1D trajectories are diffusing through these channels, with the individual trajectory segments depicting the direction of local channel orientation. The large number of oriented trajectories indicates that these materials incorporate relatively large domains (up to tens of microns in size) of oriented mesopores. Bräuchle and coworkers have provided direct evidence in support of such an assignment by comparing high-resolution TEM images of mesoporous materials to single molecule diffusion trajectories obtained from identical sample regions.[147] They did not, however, provide a quantitative assessment of trajectory orientations and channel order which will be the major topic of this study.

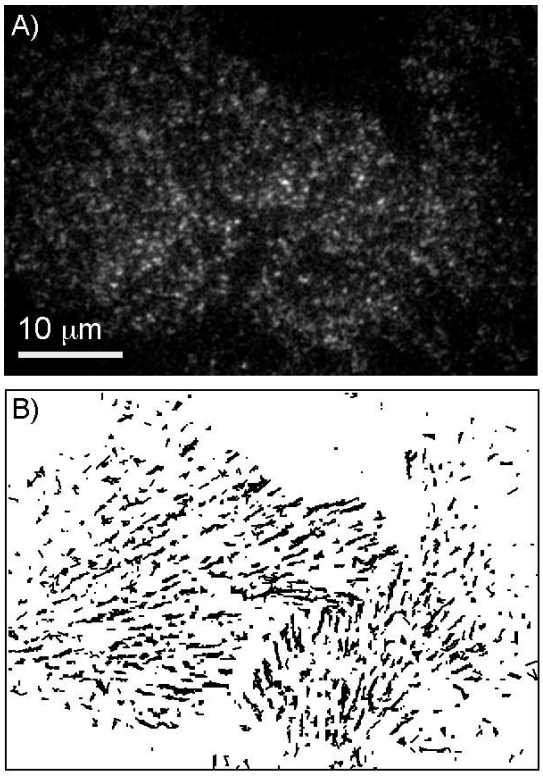

Figure 4.6. A) Representative frame of a 100-frame video depicting single molecule motions in a surfactant-templated mesoporous silica thin film. The SMT data were recorded in another film region as compared to Figure 1. Fluorescence in this video was excited using circularly-polarized light. B) Trajectories depicting the motions of the individual molecules across the full 100 frames. The data revealed the presence of three distinct grains of coherent orientation in the silica thin film. Reprinted with permission from Ref (22). Copyright 2011 The Royal Society of Chemistry.

4.3.3 Analysis of Single-Molecule Trajectory Data

Assessment of 1D trajectory orientation and order requires that 1D-diffusing molecules first to be separated from those of immobile or 2D-diffusing molecules. While the trajectories can be qualitatively separated by simple observation, information on the level of error associated with trajectory classification can only be obtained by more quantitative methods. Fortunately, the orthogonal regression method provides the quantitative means for making such a determination, namely, through the error in the fitted trajectory angle (σ_θ, Eqn. 10). The trajectory variance ratio ($\sigma_\delta^2/\sigma_R^2$, from Eqns. 7 and 8) affords an alternative, equally valid means for making this determination (see experimental section).

Because the error estimators given in Eqns. 7-10 are only valid for relatively large data sets, this analysis was only performed for trajectories $\geq$ 25 frames in length. **Figure 4.7** depicts representative trajectories and their fits (top), and histograms of the individual step angles in each (bottom).[222] Included are examples of linear trajectories showing clear evidence of 1D diffusion (**Figures 4.7AB**). These trajectories exhibit angle errors (σ_θ) of 0.4° and 1.0°, respectively, along with trajectory variance ratios of 0.003 and 0.0025. Also shown are examples of trajectories having σ_θ values of 4.7° and 7.7° and variance ratios of 0.430 and 0.663 (**Figures 4.7CD**, respectively). These two trajectories are attributed to immobile and 2D-diffusing molecules, respectively. The latter likely reflects diffusion on the surface of the silica film or in disordered porous film regions. The presence of immobile species reflects the possibility for molecular adsorption to film surfaces[214,215] or entrapment in small pores.[149] Diffusion coefficients reported below provide support for the assignment of these two populations.

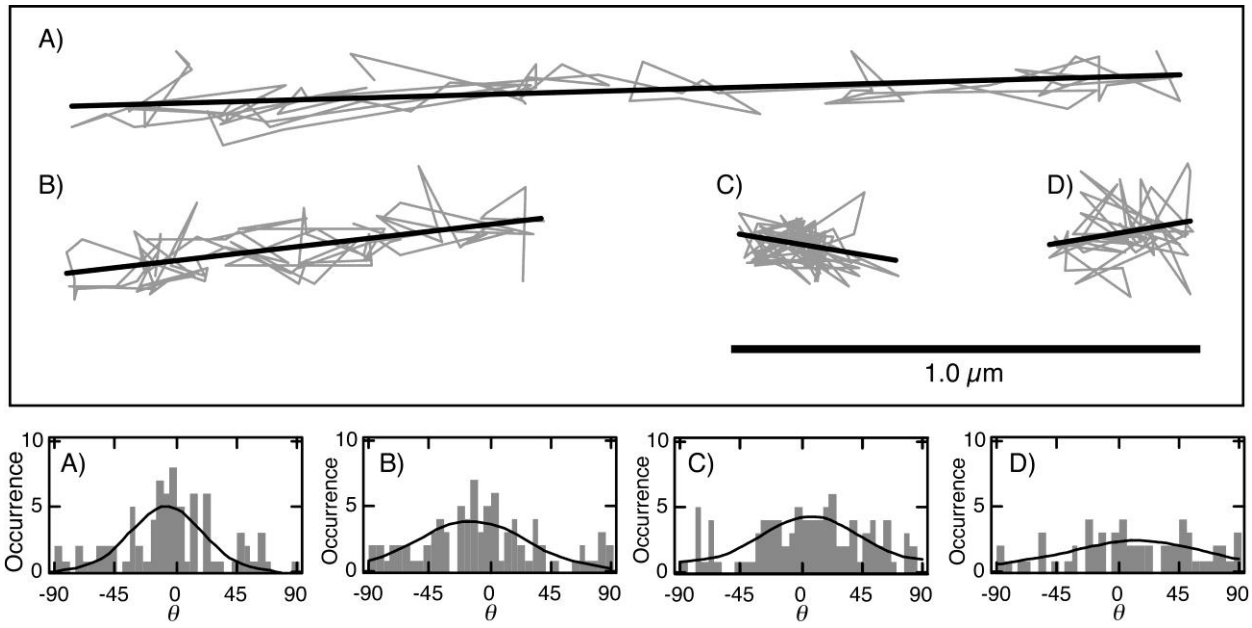

Figure 4.7. Top: Representative trajectories recorded in the silica films and fits to these data using the orthogonal regression analysis. A), B) Trajectories showing 1D diffusion and having trajectory angle errors (σ_θ) of 0.4° and 1.0°, respectively. C), D) Representative trajectories depicting immobile and 2D-diffusing single molecules with σ_θ values of 4.7° and 7.7°, respectively. Bottom: Histograms depicting the single-step angles for the trajectories shown in A) to D). Each of these distributions is fit to a Gaussian curve to determine the mean step angle. Reprinted with permission from Ref (22). Copyright 2011 The Royal Society of Chemistry.

4.3.4 Assessment of Single Molecule Populations

The individual trajectories in the SMT data were separated into two sub-populations based on their σ_θ values. **Figure 4.8A** plots the distribution in σ_θ obtained for all trajectories ($\geq$ 25 frames in length). Appended to **Figure 4.8A** is a Gaussian fit to the peak encompassing the smallest σ_θ values. This fit was used to determine a threshold of σ_θ = 3.35°, below which all trajectories were classified as 1D trajectories. Trajectories having $\sigma_\theta \geq 3.35°$ were classified as 2D-diffusing or immobile molecules. The threshold employed corresponds to a value of $2.33\sigma+\mu$ where σ represents the standard deviation of the Gaussian and μ its peak position. This threshold was selected to ensure 99% of the trajectories falling within this distribution would be counted as 1D trajectories. An estimate of the likelihood that 2D/immobile trajectories are erroneously incorporated in the 1D population was obtained by applying the same analysis to simulated data from "immobile" and 2D-diffusing molecules, as described in section 4.2.2. These results show that ~ 5.6% of the "immobile" molecules would be erroneously incorporated into the 1D population (see **Figure 4.3**), whereas as many as ~ 27% of rapidly diffusing 2D species may be incorporated with a threshold of σ_θ = 3.35°. As shown below, the vast majority of 2D/immobile molecules diffuse very slowly, indicating the actual error rate is likely close to 5.6%. **Figures 4.8BC** depict histograms of the 1D-diffusing and 2D/immobile populations determined based on this threshold. **Figure 4.9** depicts the results obtained from a similar analysis employing the trajectory variance ratio metric instead. Comparison of the histograms shown in Figures **4.8BC** and those in **Figure 4.9BC** shows that these two methods yield virtually identical results.

As is apparent from the data shown in **Figure 4.8**, approximately one half (48%) of the 153 trajectories analyzed exhibit 1D diffusion, with the remainder comprising 2D-diffusing and immobile populations. The histogram shown in **Figure 4.8B** incorporates a single peak, demonstrating that a single population of similarly-oriented trajectories is found in this region of the sample. The histogram peak position for the 1D-diffusing molecules (**Figure 4.8B**, $\sigma_\theta < 3.35°$) provides a direct measure of the mean trajectory alignment, and hence, the average orientation of the mesopores in the region imaged. Here, the mesopores are found to align, on average, very close to horizontal on the image, having $\overline{\theta} = -3.1^{\circ}$.

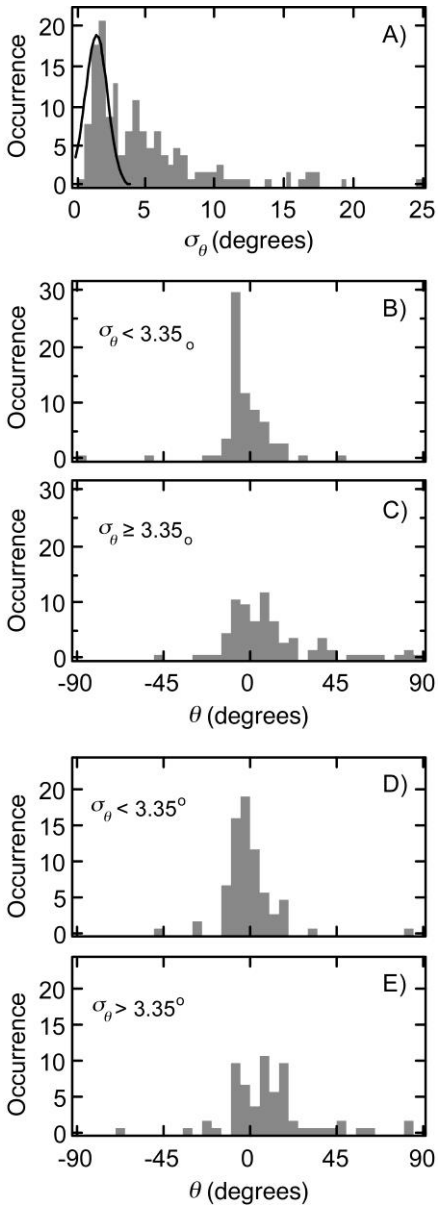

Figure 4.8. A) Distribution of trajectory angle error ($\sigma\theta$) derived from the data in **Figure 4-4**. Also shown is a Gaussian fit to the smallest distribution peak. The latter was used to determine the threshold ($\sigma\theta = 3.35^o$) for distinguishing 1D- from 2D-diffusing and immobile molecules. B), C) Distributions of trajectory angles for 1D-diffusing ($\sigma\theta < 3.35^o$) and for 2D-diffusing, immobile ($\sigma\theta \geq 3.35^o$) probe molecules, respectively. D), E) Corresponding distributions of trajectory angles determined from the average step angle for each trajectory. Only data for trajectories ≥ 25 frames in length are shown. Reprinted with permission from Ref (22). Copyright 2011 The Royal Society of Chemistry.

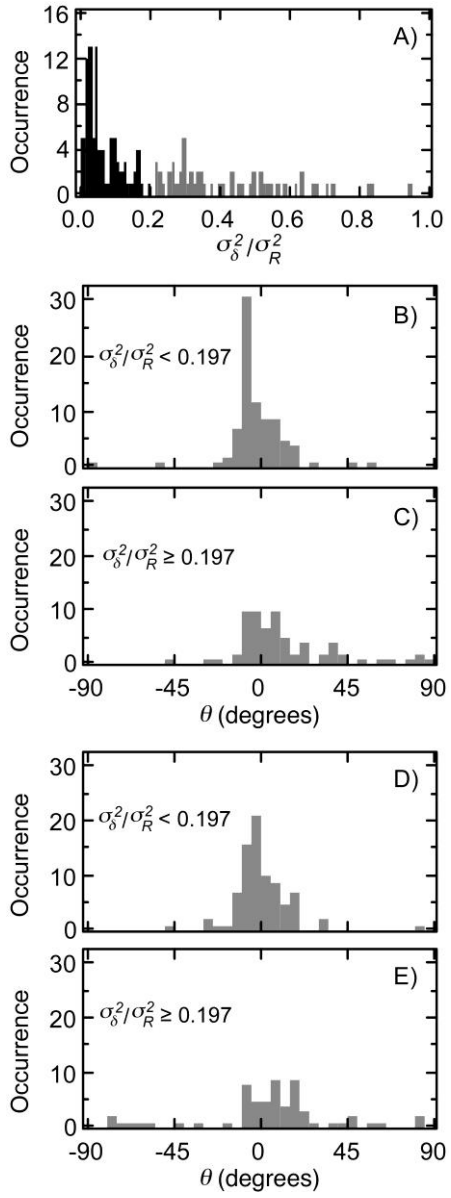

Figure 4.9. A) Distribution of $\sigma_\delta^2/\sigma_R^2$ values derived from SMT data in **Figure 4-4**. Variance ratios for 1D-diffusing and 2D/immobile populations are shown in black and gray, respectively. The data were divided into two populations using a threshold of $\sigma_\delta^2/\sigma_R^2$ = 0.197. B), C) Distributions of trajectory angles for 1D-diffusing species and for 2D-diffusing/immobile species, respectively. D), E) Corresponding distributions of trajectory angles determined from the average step angle for each trajectory. Only data for trajectories ≥ 25 frames in length are shown. These results are nearly identical to those shown in **Figure 4-8**. Reprinted with permission from Ref (22). Copyright 2011 The Royal Society of Chemistry.

4.3.5 Quantitative Assessment of Mesopore Order

The variations in the measured trajectory angles provide important physical insights into the degree of trajectory angle alignment, which directly reflects the degree of mesopore alignment in ordered domains of mesoporous silica thin films. Disordered sample regions produce broad distributions, while perfectly ordered materials will produce very narrow ones. While visual inspection of the histogram width affords a qualitative view of trajectory alignment, the order parameter $\langle P \rangle$ provides a quantitative measurement of order. It can be calculated using the following equation:

$$\langle P \rangle = 2\left\langle \cos^2(\Delta\theta) \right\rangle - 1 \qquad \text{(Eq. 4.11)}$$

For the data shown in **Figure 4.8B**, $\langle P \rangle$ = 0.90 ± 0.07 (average ± 95% confidence interval), consistent with a mean angular deviation from $\bar{\theta}$ of 13.1°. For comparison purposes, simulated videos having similar characteristics (i.e., signal-to-noise, bleaching rates, etc.,) to the experimental data and incorporating perfectly ordered trajectories were generated. **Figure 4.10** shows the results of such data with $\langle P \rangle$ = 0.998, indicating $\langle P \rangle$ from the experimental data reflects real materials disorder, and is not simply due to measurement error. This conclusion is supported by the fact that the mean trajectory angle error (1.8°) from the experimental data would also yield an order parameter of 0.998, were the trajectories perfectly ordered.

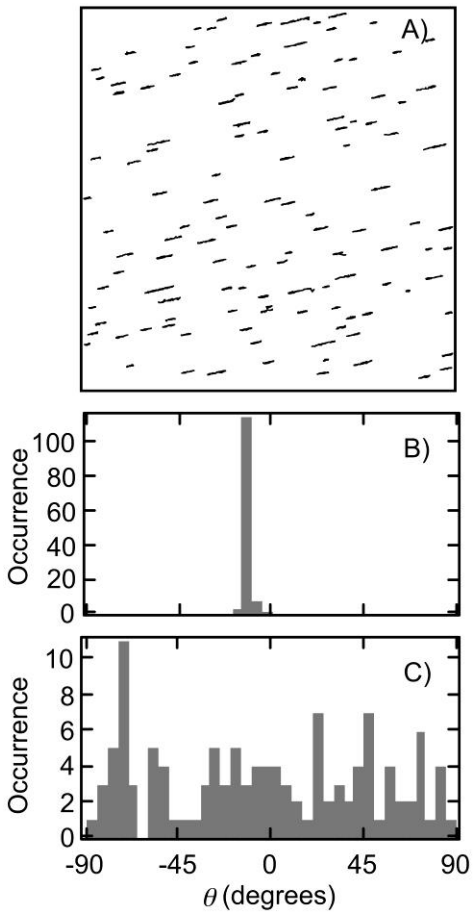

Figure 4.10. A) Trajectories from simulations of 1D-diffusing molecules. B), C) Distributions of trajectory angles for simulated 1D-diffusing and simulated 2D-diffusing species, respectively. In A), all trajectories were assigned an angle of -12.5°. All molecules were assigned diffusion coefficients of D = 3.0x10^{-10} cm^2/s. All simulation conditions (image area, dye concentration, bleaching rate, signal-to-noise ratio, etc.) were set to approximate those of the experimental data described in the main text. Reprinted with permission from Ref (22). Copyright 2011 The Royal Society of Chemistry.

4.3.6 Single-Step Analysis of SMT Data

To confirm the efficacy of the orthogonal regression analysis, trajectory orientations were also determined by calculating the average of the single-step angles for each trajectory.[222] **Figure 4.7** (bottom) presents a graphical depiction of this process in which the single-step angle histograms were fit to Gaussian functions to determine the mean angle. Histograms derived from all of the trajectories analyzed are plotted in **Figures 4.8DE**. The average trajectory orientation ($\bar{\theta} = -0.5^{\circ}$) and order parameter ($\langle P \rangle$ = 0.90 ± 0.06) for the 1D-diffusing population (**Figure 4.8D**) are similar to those determined above from the orthogonal regression. The average orientations ($\bar{\theta} = 11.8^{\circ}$, $\bar{\theta} = 4.4^{\circ}$) and order parameters (<*P*> = 0.70 ±0.10, <*P*> = 0.62 ± 0.14) of the 2D/immobile populations (regression, single-step angle data, respectively) are also similar. The relatively large $\langle P \rangle$ values obtained from the 2D-diffusing/immobile population likely reflect inclusion of some oriented 1D trajectories. Simulated videos of 2D-diffusing populations (see **Figure 4.10C**) yielded $\langle P \rangle$ = 0.00±0.13 as expected, when analyzed by the regression method. Nevertheless, the similarities of the regression and step angle results confirm the validity of the trajectory angles determined by the regression method. The advantages of the regression method include its simplicity and computational efficiency, and the ability to objectively differentiate between 1D and 2D/immobile trajectories.

4.3.7 Observation of Domaining in Mesoporous Silica Films

While the sample region analyzed above (**Figure 4.4**) incorporates a relatively large region of ordered mesopores, it is more common to find two or more differently-oriented regions within a single video. **Figure 4.6** depict one such region. Visual inspection of these data shows the presence of at least two different domains. The left half of the video incorporates trajectories aligned close to the horizontal direction, while the right half depicts trajectories oriented closer to vertical. The trajectories determined from this video were again separated into 1D-diffusing and 2D/immobile populations. The 1D-diffusing trajectories showed clear evidence for incorporation of three distinct, differently-oriented populations in this video. **Figure 4.11A** plots these trajectories. The three populations are labeled a, b, and c and are color coded to clearly depict the trajectories included in each. **Figure 4.11B** plots histograms showing the trajectory angles determined for these three populations. Populations a, b, and c yield average angles of -64.8°, -12.6° and 54.8°, respectively. They yield order parameters, $\langle P \rangle$, of 0.89 ± 0.05, 0.89 ± 0.03, and 0.87 ± 0.17 (average ± 95% confidence intervals). The latter correspond to mean angular deviations from $\bar{\theta}$ for each population of 13.6°, 13.6° and 14.8°, respectively.

It is noteworthy that all four populations analyzed from **Figures 4.4** and **4.6** yield statistically indistinguishable order parameters, suggesting that the degree of alignment for the open, 1D mesopores found in these regions is similar. Taken together with the observation that the ordered domains are not appreciably aligned by spin coating, this result suggests that the ordered assemblies of silica-encapsulated micelles self-assemble on the sample surface during spin coating, as the solvent evaporates.[223]

As a final caveat, it should be noted that under more general circumstances, proper inclusion of the 2D-diffusing/immobile populations in the assessment of materials order may suggest a lower level of materials order. However, as shown in the following section, the 2D/immobile population in the present studies exhibits diffusion coefficients that are, on average, ~ 40 times smaller than the 1D-diffusing population. It is concluded that the vast majority of these molecules are adsorbed/entrapped on/in the materials and therefore, their trajectories afford no information related to alignment of the open channels that support 1D diffusion.

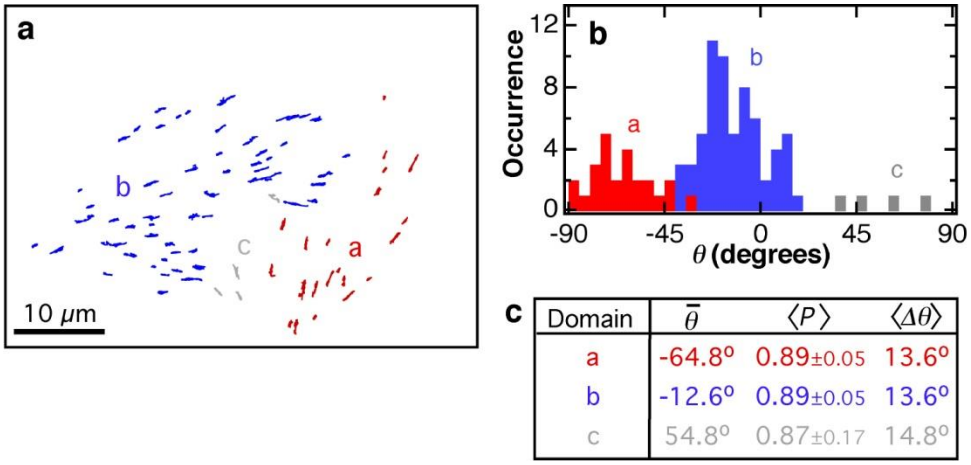

c

Domain	$\bar{\theta}$	$\langle P \rangle$	$\langle \Delta\theta \rangle$
a	-64.8°	0.89±0.05	13.6°
b	-12.6°	0.89±0.05	13.6°
c	54.8°	0.87±0.17	14.8°

Figure 4.11. A) Trajectories and B) trajectory angle histograms for 1D-diffusing molecules shown in **Figure 4.6**. Only trajectories ≥ 25 frames in length are shown. The trajectories have been divided into three distinct populations, labeled a, b, and c, based on trajectory angle and region within the image area. C) Average tilt angles, the order parameter and the standard deviation of the angle distribution of the three grains are summarized. Reprinted with permission from Ref (22). Copyright 2011 The Royal Society of Chemistry.

4.3.8 Estimation of the Single-Molecule Diffusion Coefficients

The assignment of the two single-molecule populations described above as 1D-diffusing and 2D-diffusing/immobile populations is supported by the diffusion coefficients measured for each. An estimate of the mean diffusion coefficient in each case was obtained by calculating the mean square displacement (MSD) along each trajectory. The average MSD for each trajectory was determined by first calculating the MSD for a series of time delays between one and 20 frames and then calculating the average slope of the MSD vs delay-time line. Histograms depicting the measured values are shown in **Figure 4.12**. Average diffusion coefficients were measured to be 1.6×10^{-10} cm^2/s for the 1D-diffusing ($\sigma_\theta < 3.35°$) and 4.3×10^{-12} cm^2/s for the 2D-diffusing/immobile single molecules. The latter suggests the vast majority of molecules in the $\sigma_\theta \geq 3.35°$ population are immobile. The former is similar to the diffusion coefficients reported in a number of earlier studies of related materials. For example, Zuerner, et al.[147] reported a mean 1D diffusion coefficient of 3.0×10^{-10} cm^2/s for a terylene diimide dye diffusing through mesoporous silica under a chloroform-containing atmosphere. Likewise, Ye et al.[215] reported a diffusion coefficient for Nile Red of 2.7×10^{-10} cm^2/s in nearly identical mesoporous silica materials, as determined from fluorescence correlation spectroscopy experiments performed under a humid atmosphere.

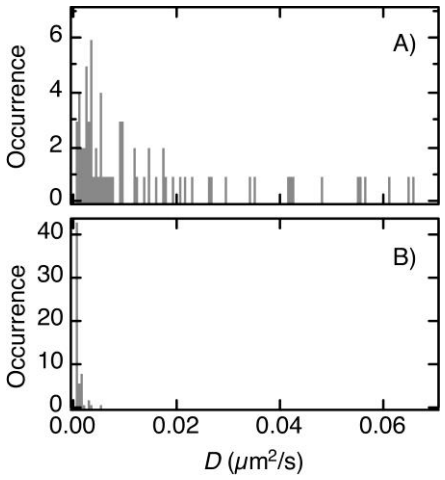

Figure 4.12. Histograms depicting the diffusion coefficients obtained from MSD measurements along individual trajectories for A) 1D-diffusing ($\sigma_\theta < 3.35°$) and B) 2D-diffusing/immobile ($\sigma_\theta \geq 3.35°$) populations. Reprinted with permission from Ref (22). Copyright 2011 The Royal Society of Chemistry.

4.3.9 Precision of Single Molecule Localization

As a final point, it is noted that the precision of single molecule localization has a direct bearing on the spread of the angles determined by orthogonal regression methods. As is now well-known, the precision to which a particular fluorescent spot can be located is often much better than the diffraction limit and is largely dependent upon the S/N ratio.[139,140] The precision of localization may be determined directly from the S/N ratio, or from the error in fitting the individual spots to Gaussian profiles. For 1D trajectories, an estimate of the particle localization precision can be obtained from the orthogonal regression analysis, as defined in Eq. 4.7. The localization variances determined for the data in **Figure 4.4** are plotted in **Figure 4.13**. These data depict mean positioning errors (standard deviations) of σ_δ = 49 nm for 1D trajectories. The minimum positioning error observed was 18 nm and the maximum was 95 nm. Previously, a localization precision of ~ 5 nm has been reported in mesoporous silica[149]. The larger errors exhibited here may reflect a reduction in S/N, but likely also arise from additional molecular mobility due to crossing of the molecules between neighboring channels and from subtle bends and kinks in the channels that cause the trajectories to deviate from perfect linearity. Due to the relatively limited spatial resolution (*ca.* 49 nm) in the present experiments, only deviations occurring on length scales greater than ~ 50 nm are detectable. The present data cannot, for example, be used to detect molecular scale (i.e. 1-3 nm) bends and kinks in the mesopores. Nevertheless, the positioning error data provides valuable information on the length scale over which the alignment and order parameter results are valid. Based on this knowledge, it may be concluded the mesoporous materials are well ordered on distances ranging from ~ 50 nm up to tens of microns, the size of the individual domains observed.

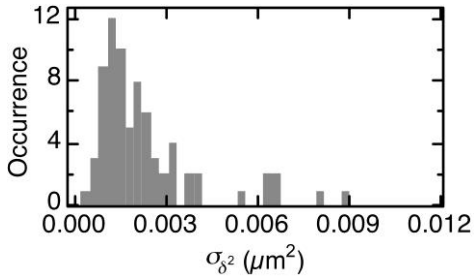

Figure 4.13. Histogram depicting the positioning error for trajectories having $\sigma_\theta < 3.35^o$ (>24 frames in length) as shown in **Figure 4.4**. Reprinted with permission from Ref (22). Copyright 2011 The Royal Society of Chemistry.

4.4 Conclusion

In conclusion, we have established an orthogonal regression procedure for the analysis of 1D diffusion trajectories observed in SMT/SPT experiments. This analysis provides quantitative measurements of the trajectory angle describing single molecule motion. It also provides estimates of the errors in trajectory angle and particle position. Histograms depicting the distribution of trajectory angles provide valuable information on materials order. The utility of this method was demonstrated by its application to the analysis of 1D diffusion in well-characterized STMS thin films, for which trajectory orientation data affords quantitative information on the (in plane) orientation of individual cylindrical mesopores. Quantitative order parameter data were obtained from the trajectories angles for four distinct sample regions. These data show that while average trajectory orientation varies significantly between domains, the order parameters obtained from these domains (and hence, mesopore order) remains relatively constant. This analysis is broadly applicable to any SMT/SPT data in which 1D motion of the particles is expected.

In the following few chapters, the orthogonal regression method was used to quantitatively assess the SMT data recorded in CF-PS-*b*-PEO films. SMT measurements were employed for the characterization of the aligned PEO microdomains in these materials induced by directional solution flow and SVP of organic solvent vapor. We applied the method to discuss the orientation and sizes of individual microdomains, as well as the microdomain organization in the materials. Systematic SMT measurements at multiple lateral position and across the film depth was employed to investigate the effect of various sample preparation conditions (e.g. flow rate, concentration, temperature, organic solvent) on the microdomain alignment in these films and to reveal possible mechanisms. The utility of the orthogonal regression method allowed valuable data to be extracted from the SMT measurements and provided a unique means for the quantitative assessment of the microdomain structures in CF-PS-*b*-PEO films.

Chapter 5 - SMT Studies of Flow-Induced Microdomain Alignment in CF-PS-*b*-PEO Films.

Reproduced with permission from The American Chemical Society
Published as: Tran-Ba, K.-H., Higgins, D. A., Ito, T. *J. Phys. Chem. B* **2014**, *118*, 11406-11415

5.1 Introduction

This chapter describes the systematic investigation of the flow-induced alignment of cylindrical PEO microdomains in thin CF-PS-*b*-PEO films using SMT methods.[22] The results offer valuable assessment of the microdomain alignment and also reveal possible mechanisms in the alignment approach. In the past, BCP films and monoliths comprising aligned cylindrical microdomains have been successfully prepared using the flow of a polymer melt or concentrated solution.[26,117] These nanostructures were aligned by applied shear forces acting on the phase-separated nanofeatures as a result of the flow of molten or viscous BCP solution along confined geometries.[224] Conventional methods afforded valuable data on the overall morphologies in macroscopic samples regions (> 10 μm or larger). However, these methods could not be used to characterize the microscopic (or smaller) morphologies. This is particularly crucial for BCPs materials consisting of a mixture of micrometer-scale grain structures.[95,225]

In this study, SMT methods have been employed to study the microscopic microdomain morphology in flow-aligned CF-PS-*b*-PEO films using SMT methods. The results reveal the usefulness of SMT for the assessment of spatially heterogeneous nanomaterials. CF-PS-*b*-PEO films were prepared under nitrogen atmosphere by depositing its benzene solution on a glass coverslip and overlaying it with a second rectangular coverslip (**Figure 5.1c**), followed by subsequent solvent evaporation. The solution flowed through the gap between the two glass plates primarily based on the pressure applied by the upper coverslip. Microdomain alignment was investigated by recording the diffusional motions of individual fluorescent SRB molecules (**Figure 5.1b**) in the SMT experiments. The SRB probe molecules were observed to preferentially partition into cylindrical PEO microdomains.[23] The morphologies and orientations of individual microdomains and the extent of their order were quantitatively assessed from single molecule trajectories using orthogonal regression methods.[22] Here, sandwiched CF-PS-*b*-PEO films were

prepared at different drying temperatures (T = 20, 40, 60 °C) and CF-PS-*b*-PEO concentrations (C = 20, 30, 40% w/w) to explore the dependence of microdomain orientation and organization on these parameters. Subsequently, SMT data in thin PS-*b*-PEO films prepared at different solution flow rates (v = 1, 3, 5 mm/s) were measured at different distances from the film-substrate interface to explore the role of shear flow in inducing PEO microdomain alignment. Importantly, the SMT data revealed the presence of μm-scale grain morphologies in the PS-*b*-PEO films, and thus allowed the quantitative assessment of order and orientation for cylindrical PEO microdomains in individual grains at ambient conditions.

5.2 Experimental Section

5.2.1 Chemicals and Materials

CF-PS-*b*-PEO (PS, M_n = 42 000 g/mol: PEO, M_n = 11 500 g/ mol; PS volume fraction = 0.8; M_w/M_n = 1.07) was purchased from Polymer Source and used as received. HPLC-grade benzene and ACS-grade SRB were purchased from Acros Organics and used without further purification. A glass coverslip (FisherFinest Premium; 25 x 25 mm^2, 0.2 mm thick) and a rectangularly-cut thinner glass slide (Goldseal® Cover Glass; 22 x 7 mm^2, 0.1 mm thick) were used as substrate and top piece, respectively. PS-*b*-PEO solutions prepared in benzene were adjusted to be 20, 30 and 40% w/w. A 200 nM SRB solution in methanol was added to a PS-*b*-PEO solution to yield nominally 5 nM dye (in the PEO microdomains after solvent evaporation) for film preparation. The SRB probe molecules were observed to preferentially partition into cylindrical PEO microdomains due to complexation of the sodium counteraction with ethylene oxide.[23] In fact, optical fluorescence images of PS-PEO homopolymer films containing SRB dyes showed that the intense fluorescence is primarily originated from phase-separated PEO regions (**Figure 5.1**).

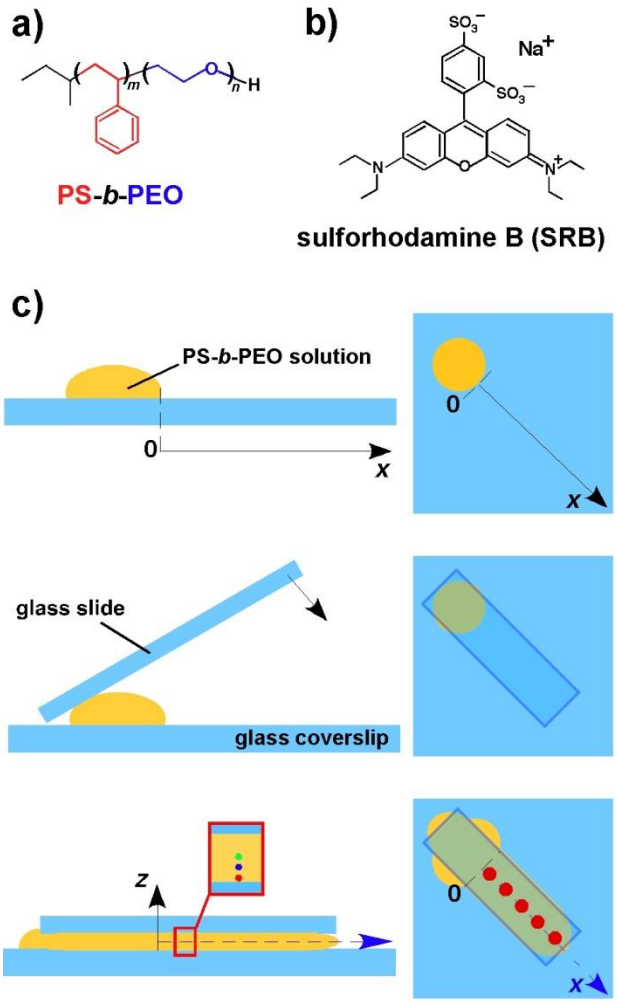

Figure 5.1. Chemical structures of (a) CF-PS-*b*-PEO and (b) SRB. (c) Schematic illustration of the procedure used to prepare a sandwiched CF-PS-*b*-PEO film: A droplet (12.5, 25, 50 µL) of PS-*b*-PEO solution, placed on an underlying glass coverslip (top), was sandwiched by a rectangular glass plate to induce the directional flow of the solution via a pressure applied by the top piece (middle). The solution spread along the gap between the two substrates to form a uniform film (bottom). The film was dried at constant temperature (T = 20, 40, 60 °C) under N_2 atmosphere for 4, 2 or 1 days prior to the SMT measurements. Each sample was measured at five different in-plane positions (red dots; bottom right) along the flow direction at $z \approx 1$ µm. Here, x = 0 mm corresponds to the right edge of the droplet prior to flowing. SMT videos were also acquired at different vertical positions (z = 1, 10 and 20-35 µm; bottom left). Reprinted with permission from Ref (24). Copyright 2014 The American Chemical Society.

5.2.2 Sample Preparation

SRB-doped CF-PS-*b*-PEO films were prepared in a nitrogen-filled glove box (relative humidity < 20%) according to the following procedure (**Figure 5.2c**): A droplet of a CF-PS-*b*-PEO solution (12.5, 25 or 50 μL) containing SRB dye was placed on a glass coverslip, and immediately sandwiched by placing a rectangular-shaped glass slide over the droplet. The solution flowed between the two glass plates from one end of the rectangular slide to the other, primarily due to the pressure applied by the top piece. The flow rate of the polymer solution, which was measured by recording a video during sample preparation, could be increased by using a larger volume of the CF-PS-*b*-PEO solution. The increase in flow rate for larger droplet volumes (e.g. 50 μL) could be attributed to the smaller drag force experienced by the solution farther from the solution-substrate interface. Prior to SMT experiments, sandwiched films were dried in the glove box at 20, 40 or 60 °C for four days, two days or one day, respectively. The different drying durations at different drying temperatures were required to adjust the diffusion rate of single molecules so that they were suitable for the SMT measurements. It should be noted that flow-induced microdomain order and orientation obtained under each set of conditions seemed to be retained, regardless of the drying duration (data not shown).

5.2.3 SMT Measurements

All SMT data collection was performed on a wide-field fluorescence microscope that was described in detail in **Chapter 3.2.**[22] . All SMT videos were 1000 frames in length and were recorded with a cycle time of 60 ms per frame, an electron-multiplying gain of 30 and a readout rate of 10 MHz. The SMT videos were recorded of 16 x 16 μm^2 film regions as 128 pixels x 128 pixels data (2 x 2 binning; 1 pixel = 125 nm). All imaging studies were conducted in air (20 - 30 % relative humidity), and at room temperature ($T \approx 20$ °C). All SMT video data were first recorded at five different locations along the flow direction of a sandwich film (**Figure 5.2c**, bottom right) near the film-substrate interface ($z \approx 1$ μm). Each of the locations was evenly separated at millimeter intervals along the centerline of the sample. The first measurement was conducted at $x \approx 1$ mm from the edge of the initial polymer droplet. In addition, SMT measurements were carried out at different vertical distances from the interface (z = 1, 10, 20 - 35 μm) at a fixed horizontal position (x) (**Figure 5.2c**, bottom left). All SMT measurements were performed in partly solvent-

swollen films after being dried for 1 - 4 days at 20 – 60 ºC, whereas negligible molecular motion was observed in films after complete solvent removal at 230 °C under vacuum (< 1 torr) overnight.[23]

5.2.4 SMT Data Analysis.

The SMT data were analyzed after generating single molecule trajectories according to the procedures reported previously.[22,23] Single molecule trajectories were obtained by linking the positions of individual molecules in consecutive frames. The molecular positions in each video frame were determined by using the ImageJ software. In this study, single molecule trajectories > 9 consecutive frames in length were analyzed and discussed. Each trajectory was fitted to a straight line using orthogonal regression methods.[22,23] 1D, 2D and immobile trajectories, reflecting 1D-diffusing, 2D-diffusing and immobile molecules, were distinguished based on the variation in single molecule positions across (σ_δ) and along (σ_R) the trajectories. Specifically, trajectories with σ_δ > 48 nm and $\sigma_R \geq 77$ nm were classified as 2D, while those with $\sigma_\delta \leq 48$ nm and $\sigma_R \geq 77$ nm were classified as 1D. Trajectories with $\sigma_\delta \leq 48$ nm and $\sigma_R < 77$ nm were identified as Immobile. The threshold values for σ_δ and σ_R were estimated from Monte-Carlo simulations of single molecule diffusion. These simulations employed a signal-to-noise (S/N) ratio and a diffusion coefficient similar to the experimental SMT data.[25,27] The in-plane orientation of each 1D trajectory was discussed by determining the tilt angle, θ, of the fitted straight line relative to the solution flow direction ($\theta = 0°$). The average in-plane orientation of 1D trajectories, $\bar{\theta}$, in a single grain was determined by fitting each θ-distribution to a Gaussian function. The in-plane order parameter of 1D trajectories, $<P>$, in a single grain was determined from the standard deviation of the Gaussian fit, $\sigma = <\Delta\theta>$, using Eq. 5.1:[121]

$$<P> = 2\cos^2<\Delta\theta> - 1 \qquad \text{(Eq. 5.1)}$$

It should be noted that the present study is focused on discussing the orientation and order of PEO microdomains obtained from single molecule diffusional motions, but not on single-molecule diffusion rates due to the ill-controlled solvent content in the films.[23] The radius of cylindrical PEO domains was estimated from 1D trajectories[17,23] to be 11 ± 7 nm (average ± standard deviation; obtained from 1424 trajectories in 30 SMT videos recorded for PS-*b*-PEO films prepared at T = 40 °C, C = 30% w/w, v = 5 mm/s and z = 1 μm), which was close to that in a dried

film (14 ± 2 nm, from AFM images). The large standard deviation from the SMT measurement is primarily due to the limited S/N of the data.[23]

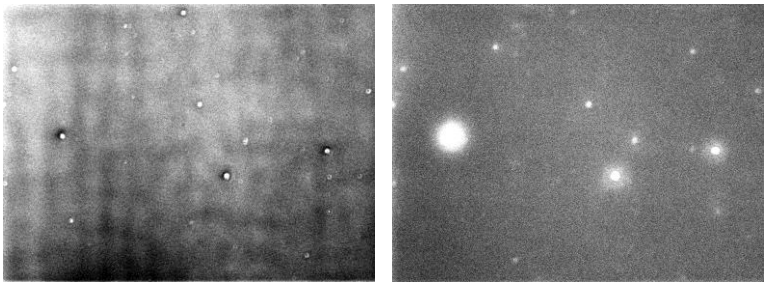

Figure 5.2. Optical (left) and fluorescence (right) images (167 x 223 μm^2) measured from the same area of a SRB-doped thin film prepared from a toluene solution containing PS (412,000 g/mol) and PEO (12,000 g/mol) homopolymers (PS : PEO = 89 : 11). These polymers were purchased from Polymer Source. A toluene solution containing 1.25 wt% PS and 0.15 wt% PEO in addition to SRB (4 nM if the dye uniformly distributed) was spin-coated on a glass coverslip (2000 rpm, 30 sec), and then dried under ambient conditions for one day. The ellipsometric thickness of the film was 68 nm. Fluorescence was observed only at the dots shown in the left image. The number of dots was larger in a film containing PS : PEO = 82 : 18 (data not shown). These images were measured using a 40X objective lens. Reprinted with permission from Ref (23).

5.3 Results and Discussion

In this study, SMT was used to investigate the alignment of cylindrical PEO microdomains in PS-*b*-PEO films induced by pressure-driven solution flow between two glass plates. A PS-*b*-PEO film was formed by sandwiching its benzene solution between two rectangular glass slides (**Figure 5.2c**). The placement of the top glass slide led to the directional flow of the solution, which was expected to induce microdomain alignment in the flow direction by a shear force. SMT measurements were carried out for films that were dried to remove the majority of solvent. Such films showed the diffusional motion of SRB molecules.[23]

In the past, BCP microdomain alignment induced by solution flow was experimentally demonstrated[118,136] and theoretically explained.[226] It was reported that microdomains were better aligned when BCP monoliths were prepared from a more viscous, concentrated BCP solution at higher flow rate, *i.e.*, in the presence of a larger flow-induced shear force.[134,135] In addition, the deterioration of microdomain alignment was reported if the monoliths were dried slowly.[118] Considering the requirement to use partially-solvent swollen CF-PS-*b*-PEO films for SMT measurements,[23] we first studied the effects of drying temperature (T = 20, 40, 60 °C) on microdomain alignment in CF-PS-*b*-PEO films. Subsequently, we assessed microdomain alignment in films prepared at different CF-PS-*b*-PEO concentrations (C = 20, 30, 40% w/w) to find a solution composition suitable for the film preparation method shown in **Figure 5.2c**. Then, we investigated microdomain alignment in CF-PS-*b*-PEO films prepared at different flow rates (v = 1, 3, 5 mm/s) by controlling the solution volume (see Experimental). SMT data measured at different vertical positions (z = 1, 10, 20-35 μm) in addition to the flow-rate dependence permitted us to attribute microdomain alignment to shear flow during film preparation.

5.3.1 Effects of Drying Temperatures on Microdomain Alignment.

Figure 5.3a shows representative wide-field fluorescence images acquired in CF-PS-*b*-PEO films that were prepared from a 30% w/w benzene solution at v = 5 mm/s and then dried at 20 °C for 4 days (top), 40 °C for 2 days (middle) or 60 °C for 1 day (bottom). Each wide-field image depicts the first frame of a 1000-frame SMT video. These images clearly show individual fluorescence spots of diffraction-limited size that correspond to single SRB molecules. **Figure 5.3b** shows single-molecule trajectories obtained from the SMT data shown in **Figure 5.3a**. A large number of 1D trajectories oriented in the solution flow direction were found in the films dried at 40 and 60 °C (**Figure 5.3b**, middle and bottom), reflecting the diffusion of SRB molecules along 1D-aligned cylindrical microdomains over μm-length scales. In contrast, curved trajectories and 1D trajectories tilted from the flow direction were observed in the film dried at 20 °C (**Figure 5.3b**, top), reflecting the presence of curved and misoriented microdomains, respectively.

In addition to the 1D and curved trajectories, these SMT data depict spot-like trajectories originating from immobile probe molecules that are absorbed at the film-substrate interface or at the PS-PEO boundary regions, or are incorporated into unelongated PEO microdomains. Furthermore, some of the 1D trajectories have larger widths, reflecting molecular diffusion within less-confined pathways.[23] Here, the curved and wider 1D trajectories are defined as 2D trajectories. The trajectories obtained from multiple SMT videos were classified as 1D, 2D and immobile ones (**Table 5.1**) using orthogonal regression methods as discussed previously (see Experimental Procedures).[22,23] **Table 5.1** shows that CF-PS-*b*-PEO films dried at 20 °C exhibited a larger fraction of 2D trajectories than those dried at the higher temperatures (> 99% confidence level, CL), as described above. The higher 2D trajectory ratio at T = 20 °C may reflect chain relaxation induced during slow solvent evaporation, which leads to defect formation in gel-like BCP mesophases.[134,135] Further quantitative assessment of the flow-induced microdomain alignment was explored only for 1D trajectories.

Figure 5.3c shows histograms of the trajectory tilt angles, θ, of individual 1D trajectories obtained from the SMT data shown in **Figure 5.3b**. The histograms are clearly peaked near 0° for films dried at the higher T, whereas the histogram for one dried at 20 °C shows two distinct distributions that peak around -17º and 58º. The single peaks with narrow θ-distributions for the former films indicate the presence of single grains comprising highly-ordered microdomains within the 16 x 16 μm^2 region. In addition, the peak near 0° indicates predominant microdomain

alignment in the solution flow direction. In contrast, the observation of two distinct distributions for the film dried at 20 °C suggests the presence of two grains. Importantly, each of them comprises microdomains with a coherent orientation. Indeed, the single molecule trajectory data in **Figure 5.3b** shows two grains based on trajectories aligned in two different directions that may be connected to give curved trajectories. Unfortunately, the size of individual grains was challenging to be estimated from the SMT videos because the boundaries between neighboring grains were made unclear by the relatively large spacing between adjacent trajectories due to the low probe concentration employed.

Table 5.1 summarizes the average in-plane orientation of 1D trajectories, $\overline{|\bar{\theta}|}$, observed for different individual grains in multiple samples. It is clear that films dried at the higher *T* exhibited trajectory orientations closer to the flow direction, as represented by a smaller $\overline{|\bar{\theta}|}$ (> 90% CL). Faster solvent evaporation at higher *T* facilitated 'locking up' of the flow-induced microdomain orientation prior to their relaxation, as reported by Albalak and Thomas.[118]

The width of the θ-distribution provides a means for quantitative assessment of the orientational order of the cylindrical microdomains in individual grains. Narrower distributions reflect higher microdomain order. Interestingly, the order parameter <*P*> obtained from the widths of the distributions in individual grains was, on average, similarly high regardless of *T* (**Table 5.1**). This observation indicates that the packing of the microdomains in each grain was retained during the relaxation of microdomain orientation upon solvent evaporation.

Figure 5.3d depicts the relationship between <*P*> and $\bar{\theta}$ measured for individual grains. It is clear that the deviation of $\bar{\theta}$ from 0° was smaller at higher *T*, whereas many grains exhibited high <*P*> regardless of *T*. There is no clear correlation between <*P*> and $\bar{\theta}$. These results suggest the involvement of different mechanisms in microdomain orientation and ordering: The former was enhanced by shear flow and relaxed during solvent evaporation, whereas the latter reflected the agglomeration of cylindrical microdomains in the benzene solution and was affected by solvent evaporation from fairly concentrated solutions. These results revealed the importance of higher solvent evaporation rates on preserving the flow-induced alignment of 1D microdomains in BCP films.

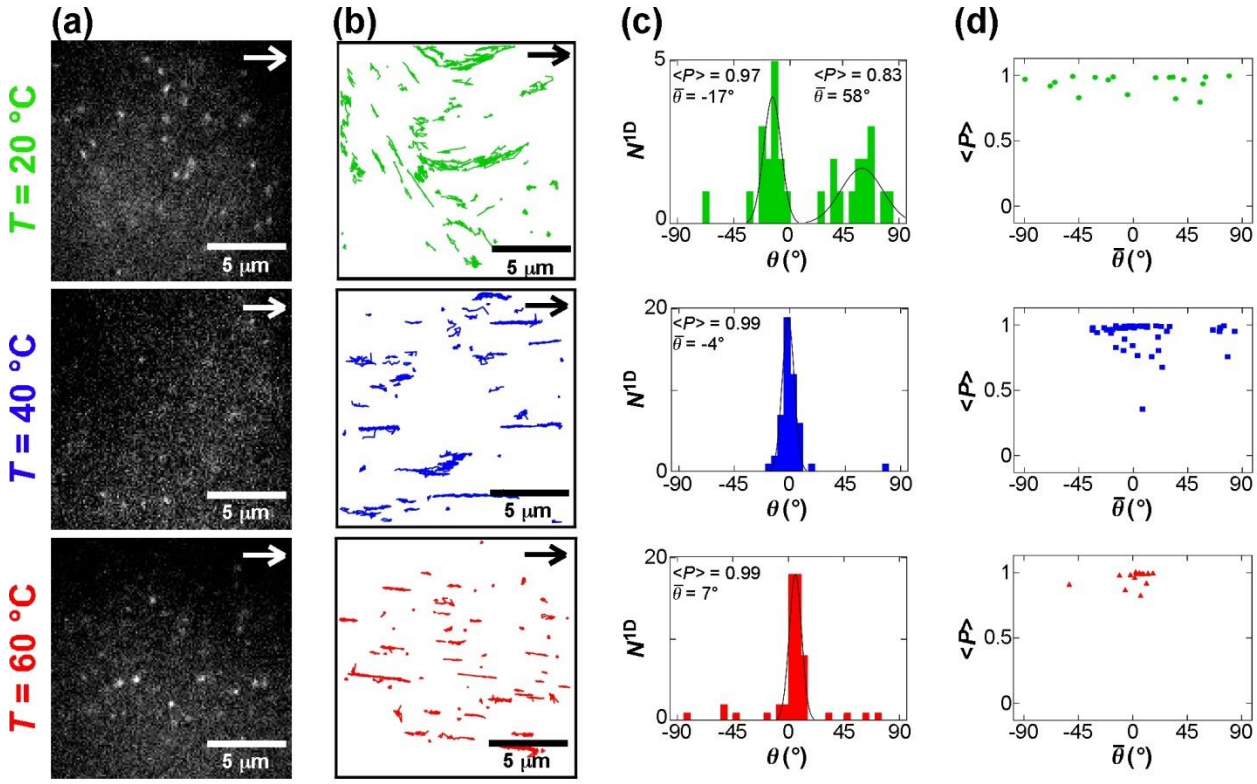

Figure 5.3. (a) Representative wide-field fluorescence images recorded in PS-*b*-PEO films after being dried at different temperatures (T = 20, 40, 60 °C). Upon drying for 4 days (T = 20 °C), 2 days (T = 40) or 1 day (T = 60 °C), SMT data were recorded near the film-substrate interface ($z \approx$ 1 μm). The arrows in the images indicate the flow direction of CF-PS-*b*-PEO solution. (b) Single molecule trajectories > 9 frames in length obtained from the videos shown in (a). (c) Histograms showing the number of 1D trajectories, N^{1D}, at different tilt angles, θ, relative to the flow direction (θ = 0°) obtained from SMT data shown in (a, b). Average tilt angle, $\bar{\theta}$, and order parameter, $\langle P \rangle$, values obtained by fitting the distributions to Gaussian curves (solid lines) are also given. (d) Plots showing the relationship between $\langle P \rangle$ and $\bar{\theta}$ measured for individual grains. The total number of grains, N_{grain}, measured in each type of sample is shown in Table 5.1. Note that Figure 5.3c (middle) shows the same data as Figures 5.4c (middle) and Figure 5.5c (bottom), reflecting the results of the same sample series. Reprinted with permission from Ref (24). Copyright 2014 The American Chemical Society.

Table 5.1. Effects of Drying Temperature on the Fractions of 1D/2D-Diffusing and Immobile Molecules, Average Tilt Angle and Order Parameter from the 1D Trajectories[a]

T *(°C)*	*1D*	*2D*	*Immobile*	$\left\|\overline{\bar{\theta}}\right\|$ *(°)*[b]	<P>[b]	N_{Grain}[c]
20	0.18 ± 0.08	0.37 ± 0.15	0.45 ± 0.18	45 ± 23	0.94 ± 0.07	18
40	0.33 ± 0.13	0.22 ± 0.14	0.43 ± 0.16	22 ± 23	0.93 ± 0.11	52
60	0.30 ± 0.11	0.20 ± 0.14	0.50 ± 0.19	10 ± 12	0.96 ± 0.05	16

[a] Average and standard deviation from SMT data acquired at five different horizontal positions near the film-substrate interface ($z \approx 1$ μm) in each of the three (T = 20 and 60 ºC) or nine (T = 40 ºC) films. The films were prepared from 30% w/w PS-*b*-PEO solution at a flow rate of v = 5 mm/s, and dried for 4 days (T = 20 °C), 2 days (T = 40 °C) or 1 day (T = 60 °C) under nitrogen atmosphere prior to the SMT measurements. [b] Average and standard deviation of the parameters obtained from multiple grains. [c] The total number of μm-scale grains obtained from the three or nine films (15 or 45 SMT videos, respectively). Note that the data of 40 °C (**Table 5.1**, middle) are the same as those of 30% w/w (**Table 5.2**, middle) and 5 mm/s (**Table 5.3**, bottom), reflecting the same sample series. Reprinted with permission from Ref (24). Copyright 2012 The American Chemical Society.

5.3.2 Effects of CF-PS-b-PEO Concentration on Microdomain Alignment

Figure 5.4a depicts representative single molecule trajectories in CF-PS-*b*-PEO films prepared from benzene solutions of different polymer concentrations (C = 20, 30, 40% w/w) at a fixed v (5 mm/s) and T (40 °C). A number of 1D trajectories, reflecting the diffusion of SRB molecules within elongated PEO microdomains, were observed at the three C examined (**Figure 5.4a**). Indeed, the ratio of 1D trajectories was similar regardless of C (**Table 5.2**). In contrast, the microdomain orientation and order was strongly affected by C: Many trajectories in the film prepared at C = 30% w/w (middle) were oriented in the flow direction, whereas those in the other films exhibited significant tilting (C = 40% w/w) and curving (C = 20% w/w). The histograms of the θ-distribution of individual 1D trajectories **(Figure 5.4b)** support the observations in **Figure 5.4a**. Note that the histogram for C = 20% w/w exhibited a single, sharp distribution, apparently because it does not reflect the presence of the curved trajectories. The average orientation of 1D trajectories ($\bar{\theta}$) in each grain was close to zero for these histograms, reflecting microdomain orientation in the flow direction. However, the histogram for the film prepared from a solution of 40% w/w (bottom) shows a broader distribution of θ, giving a smaller $\langle P \rangle$. For multiple samples/grains, trajectory orientation in the flow direction was more reproducibly observed for a 30% w/w solution, as shown in **Figure 5.4c** and by $\overline{|\bar{\theta}|}$ relatively closer to 0° as compared to the others (**Table 5.2;** > 80 % CL). In addition, 30% w/w solutions offered 1D trajectories with slightly higher order than 20% w/w solutions, as indicated by the larger $\langle P \rangle$ shown in **Table 5.2** (> 90% CL). These results indicate that the 30% w/w solution is the most suitable to prepare PS-*b*-PEO films with the desired microdomain orientation.

The observation of better-aligned microdomains at the intermediate concentration can be explained by considering solution viscosity and flow rate. It is known that the shear-induced alignment is enhanced at higher flow rates of a more viscous solution.[134,135] Here, the solution viscosity increases with increasing C. In contrast, the flow rate was lower at higher C due to higher viscosity, because the films were prepared from a fixed solution volume (50 μL) using a rectangular upper glass slide of constant mass: $v \approx 1$, 5 and 10 mm/s for 40, 30 and 20% w/w solutions, respectively. The 40% w/w solution did not provide a sufficiently high v, while the 20% w/w solution did not have a sufficiently high solution viscosity, resulting in less efficient shear-based microdomain alignment as compared to the 30% w/w solution.

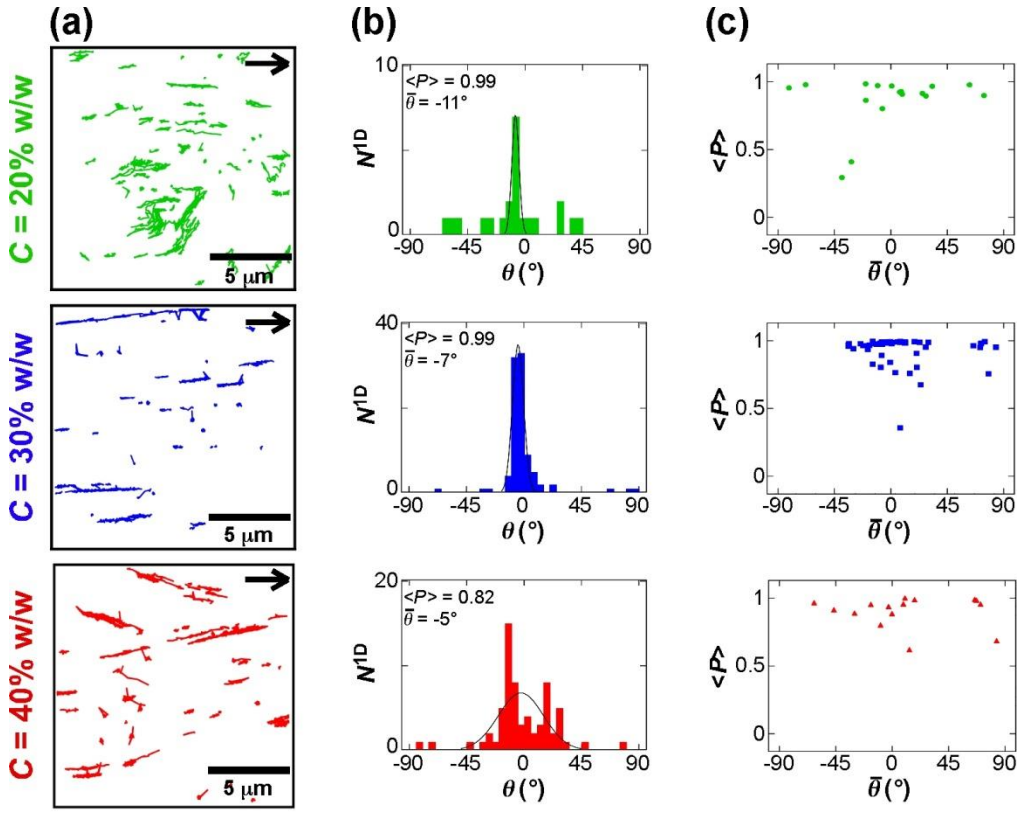

Figure 5.4. (a) Representative single molecule trajectories > 9 frames in length measured in films prepared at different CF-PS-*b*-PEO concentrations (C = 20, 30, 40% w/w) near the film-substrate interface ($z \approx 1$ μm). The arrows in the images indicate the flow direction of CF-PS-*b*-PEO solution. (b) Histograms showing N^{1D} at different θ obtained from SMT data shown in (a). (c) Plots showing the relationship between $<P>$ and $\bar{\theta}$ measured for individual grains. The N_{grain} measured in each type of sample is shown in Table 5.2. Note that the single molecule trajectory data and histogram for C = 30% w/w (Figure 5.4ab, middle) are different from those in Figures 5.3bc (middle) and 5.5ab (bottom)/6ab (top) due to the use of a different sample prepared under the same conditions. However, Figure 5.4c (middle) shows the same data as Figures 5.3c (middle) and 5.5c (bottom), reflecting the results of the same sample series. Reprinted with permission from Ref (24). Copyright 2014 The American Chemical Society.

Table 5.2. Effects of CF-PS-*b*-PEO Concentration on the Fractions of 1D/2D-Diffusing and Immobile Molecules, Average Tilt Angle and Order Parameter from the 1D Trajectories.[a]

C *(% w/w)*	*1D*	*2D*	*Immobile*	$\overline{\lvert\bar{\theta}\rvert}$ *(°)*[b]	<P>[b]	N_{Grain}[c]
20	0.35 ± 0.10	0.26 ± 0.12	0.39 ± 0.13	31 ± 26	0.86 ± 0.20	17
30	0.33 ± 0.13	0.22 ± 0.14	0.43 ± 0.16	22 ± 23	0.93 ± 0.11	52
40	0.32 ± 0.06	0.32 ± 0.08	0.36 ± 0.09	34 ± 29	0.90 ± 0.11	15

[a] Average and standard deviation from SMT data acquired at five different horizontal positions near the film-substrate interface ($z \approx 1$ μm) in each of the three (C = 20 and 40% w/w) or nine (C = 30% w/w) films. The flow rate was 10, 5 and 1 mm/s for 20, 30, 40% w/w CF-PS-*b*-PEO solutions, respectively, due to the difference in solution viscosity. The films were dried at 40 ºC under nitrogen atmosphere for two days prior to the SMT measurements. [b] Average and standard deviation of the parameters obtained from multiple grains. [c] The total number of μm-scale grains obtained from the three or nine films (15 or 45 SMT videos, respectively). Note that the data of 30% w/w (**Table 5.2**, middle) are the same as those of 40 °C (**Table 5.1**, middle) and 5 mm/s (**Table 5.3**, bottom), reflecting the same sample series. Reprinted with permission from Ref (24). Copyright 2012 The American Chemical Society.

5.3.3 Effects of Solution Flow Rate on Microdomain Alignment.

To discuss the influences of shear forces on microdomain alignment more clearly, it is essential to measure CF-PS-*b*-PEO films prepared at a fixed solution viscosity (*i.e.*, at a fixed *C*) with different flow rates (*v*). **Figure 5.5a** shows representative single molecule trajectories in CF-PS-*b*-PEO films prepared at a different *v* (1, 3, 5 mm/s) from 30% w/w benzene solutions at a fixed *T* (40 °C). The flow rates were varied by adjusting the volumes of CF-PS-*b*-PEO solutions. **Figure 5.5a** clearly shows that films prepared at higher *v* exhibited 1D trajectories better-oriented in the flow direction, as supported by the histograms (**Figure 5.5b**) showing a larger number of 1D trajectories with θ close to 0°. The percentage of 1D trajectories was independent of *v* (**Table 5.3**). Importantly, the improvement of trajectory orientation at *v* = 5 mm/s was reproducibly observed, as indicated by the narrower distribution in $\bar{\theta}$ about 0° (**Figure 5.5c**) and the $\overline{|\bar{\theta}|}$ values closer to 0° (**Table 5.3**; > 70% CL) from multiple grains obtained at *v* = 5 mm/s. In addition, the trajectory order was slightly improved at higher *v*, as represented by the larger <*P*> (**Table 5.3**; > 80% CL for data at *v* = 1 mm/s as compared to the others). These observations reveal enhanced microdomain alignment in the flow direction at higher *v*, as anticipated for shear-induced microdomain alignment.[135,136]

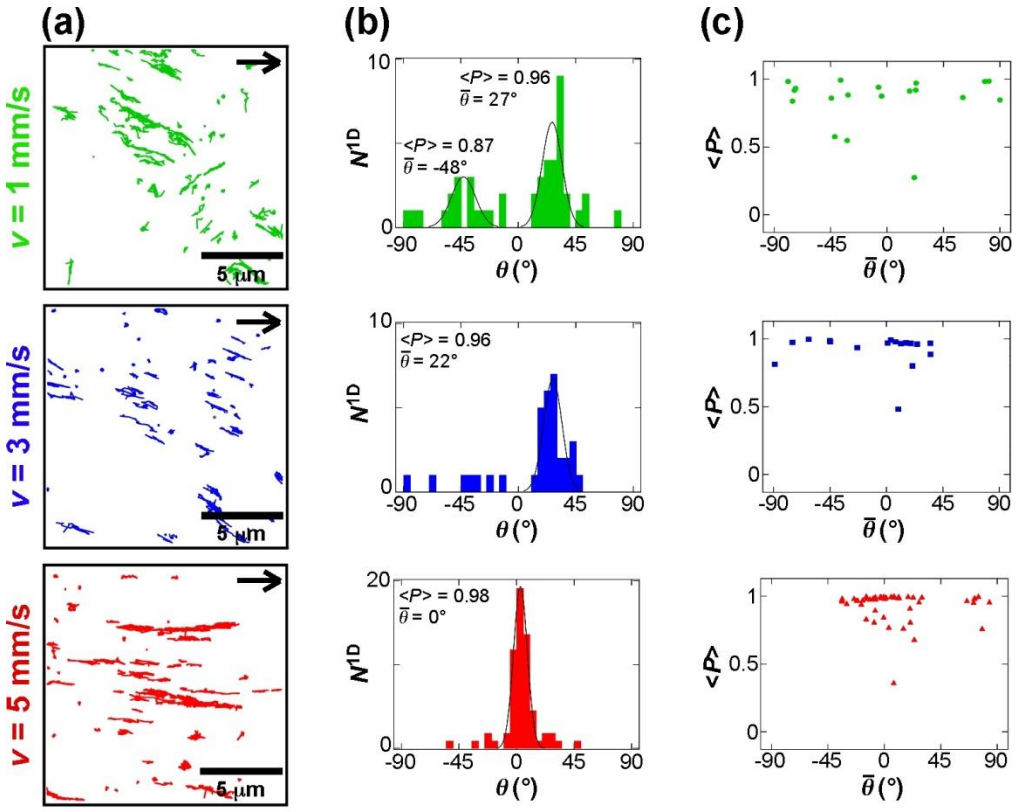

Figure 5.5. (a) Representative single molecule trajectories > 9 frames in length measured in films prepared at different flow rates (v = 1, 3, 5 mm/s) near the film-substrate interface ($z \approx 1$ μm). The arrows in the images indicate the flow direction of CF-PS-*b*-PEO solution. (b) Histograms showing N^{1D} at different θ obtained from SMT data shown in (a). (c) Plots showing the relationship between $<P>$ and $\bar{\theta}$ measured for individual grains. The N_{grain} measured in each type of sample is shown in **Table 5.3**. Note that the single molecule trajectory data and histogram for v = 5 mm/s (**Figure 5.5ab**, bottom) are different from those in **Figures 5.3bc** (middle) and **5.4ab** (middle) due to the use of a different sample prepared under the same conditions. However, **Figure 5.5c** (bottom) shows the same data as **Figures 5.3c** (middle) and **5.4c** (middle), reflecting the results of the same sample series. Reprinted with permission from Ref (24). Copyright 2014 The American Chemical Society.

Table 5.3. Effects of Solution Flow Rate on the Fractions of 1D/2D-Diffusing and Immobile Molecules, Average Tilt Angle and Order Parameter from the 1D Trajectories.[a]

v (mm/s)	*1D*	*2D*	*Immobile*	$\overline{\lvert\theta\rvert}$ (°)[b]	<*P*>[b]	N_{Grain}[c]
1	0.34 ± 0.14	0.17 ± 0.08	0.49 ± 0.15	47 ± 28	0.85 ± 0.19	19
3	0.36 ± 0.09	0.24 ± 0.06	0.40 ± 0.06	30 ± 25	0.92 ± 0.12	18
5	0.33 ± 0.13	0.22 ± 0.14	0.43 ± 0.16	22 ± 23	0.93 ± 0.11	52

[a] Average and standard deviation from SMT data acquired at five different horizontal positions near the film-substrate interface ($z \approx 1$ μm) in each of the three (v = 1 and 3 mm/s) or nine (v = 5 mm/s) films. Such films were prepared from CF-PS-*b*-PEO solutions (C = 30% w/w), and then dried at T = 40 ºC for two days prior to the SMT measurements. [b] Average and standard deviation of the parameters obtained from multiple grains. [c] The total number of μm-scale grains obtained from the three or nine films (15 or 45 SMT videos, respectively). Note that the data of 5 mm/s (**Table 5.3**, bottom) are the same as those of 40 °C (**Table 5.1**, middle) and 30% w/w (**Table 5.2**, middle), reflecting the same sample series.

5.3.4 Flow-Induced Microdomain Alignment at Different Film Depth.

One of the advantages of SMT for materials characterization is its capability to probe nanostructures across μm-scale depths.[23] It is well-known that a larger flow-induced shear force is applied near the interface between two media due to the higher local shear velocity. Here, SMT was thus used to investigate the *z*-dependence (depth profile) of the microdomain alignment in CF-PS-*b*-PEO films. **Figure 5.6a** depicts representative single molecule trajectories in a film measured at different distances from the film–substrate interface (z = 1, 10, 20 μm). The film was prepared from a C = 30% w/w benzene solution at v = 5 mm/s and T = 40 °C. Both **Figure 5.6a** and **Table 5.4** show a similarly large number of 1D trajectories, regardless of z. However, the trajectory orientation was dependent on *z*: The orientations of 1D trajectories deviated from the flow direction at larger *z*, as supported by the corresponding histograms (**Figure 5.6b**). There are two grains in the trajectory data recorded at z = 10 μm (**Figure 5.6a**, middle), yielding peaks at $\bar{\theta}$ = 2° and = -62° in **Figure 5.6b** (middle). The larger deviation of trajectory orientation at larger *z* is also evident from the deviation of $\bar{\theta}$ from 0° in **Figure 5.6c** and the $\overline{|\bar{\theta}|}$ values in **Table 5.4** (> 90% CL for z = 0 μm vs. $z \geq 10$ μm). Interestingly, the trajectory order in individual grains was similarly high (<*P*> ≈ 0.9) regardless of *z* (**Table 5.4**). These results suggest the involvement of different mechanisms behind microdomain ordering (the grain formation) and orientation, as discussed above.

The *z*-dependent microdomain orientation can be qualitatively understood by considering a shear force active at the solution-substrate interface during film preparation. The flow of polymer solution during sample preparation was primarily driven by the pressure applied upon the placement of the rectangular glass plate over the polymer solution. Such flow is expected to exhibit a parabolic flow profile due to the presence of stagnant boundary layers on the surfaces of the two substrates.[224] In a parabolic flow profile, the local shear velocity (thus shear force) is greatest in the region closest to the solution-substrate interface, resulting in the microdomain orientation defined by the flow direction at smaller *z*. However, the shear force was not strong enough to efficiently stretch cylindrical microdomains, as indicated by the similar 1D fractions measured in samples at different *z* and *v* (**Tables 5.4** and **5.3**). The observation that <*P*> is not strongly dependent upon either *v* or *z*, suggests that the microdomain order was predominantly determined by their agglomeration in solution rather than by shear forces active during sample preparation (*vide supra*).

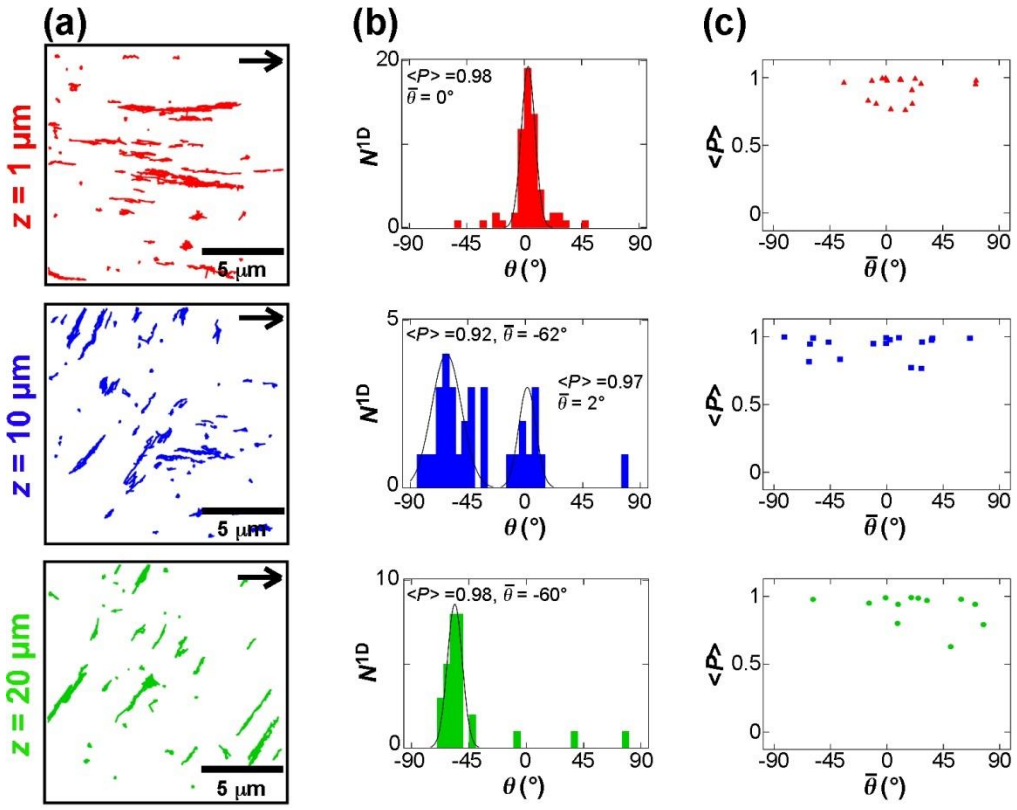

Figure 5.6. (a) Representative single molecule trajectories > 9 frames in length recorded at different distances from the film-substrate interface (z = 1, 10, 20 μm) in a CF-PS-*b*-PEO film. The film was prepared at v = 5 mm/s, C = 30% w/w and dried at T = 40 °C for 2 days. The arrows in the images indicate the flow direction of CF-PS-*b*-PEO solution. (b) Histograms showing N^{1D} at different θ obtained from SMT data shown in (a). (c) Plots showing the relationship between $<P>$ and $\bar{\theta}$ measured for individual grains. The N_{grain} measured in each type of sample is shown in **Table 5.4**. Note that the single molecule trajectory data and histogram for z = 1 μm (**Figure 5.6ab**, top) are the same as those in **Figure 5.5ab** (bottom). However, **Figure 5.6c** (top) shows different data than **Figure 5.5c** (bottom) due to a smaller number of data set that were recorded at different z. Reprinted with permission from Ref (24). Copyright 2012 The American Chemical Society.

Table 5.4. Fractions of 1D/2D-Diffusing and Immobile Molecules, Average Tilt Angle and Order Parameter from the 1D Trajectories Recorded at Different Distances from the Film-Substrate Interface.[a]

z (μm)	*1D*	*2D*	*Immobile*	$\overline{\lvert\theta\rvert}$ (°)[b]	<*P*>[b]	N_{Grain}[c]
1	0.32 ± 0.15	0.22 ± 0.09	0.46 ± 0.15	20 ± 21	0.92 ± 0.09	18
10	0.33 ± 0.15	0.19 ± 0.09	0.47 ± 0.16	34 ± 25	0.93 ± 0.08	17
20 - 35	0.32 ± 0.08	0.21 ± 0.05	0.48 ± 0.09	35 ± 27	0.91 ± 0.11	12

[a] Average and standard deviation from SMT data acquired at different horizontal positions in three different films. These films were prepared from CF-PS-*b*-PEO solutions (C = 30% w/w) at v = 5 mm/s, and then dried at T = 40 ºC for two days prior to the SMT measurements. A series of SMT data were collected at three different z for each film. In total, fifteen (z = 1 μm), thirteen (z = 10 μm) and eight SMT videos (z = 20-35 μm) were recorded. [b] Average and standard deviation of the parameters obtained from multiple grains. [c] The total number of μm-scale grains obtained from the three films. Note that the data at z = 1 μm (**Table 5.4**, top) are different from those at 5 mm/s (**Table 5.3**, bottom) due to the limited number of SMT videos recorded at different z. Reprinted with permission from Ref (24). Copyright 2012 The American Chemical Society.

5.4 Conclusions

In this study, SMT has been demonstrated to be a useful tool for the quantitative assessment of the microdomain morphologies in thin BCP films. We systematically investigated the flow-induced alignment of cylindrical PEO microdomains in CF-PS-*b*-PEO films prepared by sandwiching a polymer solution droplet between two glass plates. SMT could be used to quantitatively assess the alignment of individual microdomains as well as microdomain order in individual μm-scale grains from 1D single molecule diffusion trajectories. The microdomain orientation in a CF-PS-*b*-PEO film prepared from its solution could be controlled under a pressure-driven flow and was consistent with a shear-flow mechanism, as indicated by the flow rate dependence and depth profile of microdomain orientation. In contrast, the fraction of 1D microdomains and microdomain order in individual grains was less sensitive to the sample preparation conditions, probably because they reflected microdomain agglomeration morphologies in the relatively concentrated solutions. Furthermore, optimization of drying temperature was needed to reduce the misorientation of microdomains and grains during solvent evaporation. The presence of μm-scale grains in films prepared from a BCP solution was found as a possible obstacle to fabrication of macroscopically-aligned microdomains which is essential for many technological applications.

Thus, we sought to further improve the microdomain alignment without grain-structures and boundaries for the entire film thickness using an previously reported SVP approach. This method relies on the directional vapor penetration form one side to the other side of the film or monolith. This has been reported by Osuji to lead to the formation of well-aligned microdomains across the entire film thickness (< 1 mm).[25] In chapter 6, the SVP-induced microdomain alignment in CF-PS-*b*-PEO films treated by different organic solvent vapors is studied using SMT.[23] The results are also being used to evaluate the extent of the microdomain alignment. In particular, the presence of a millimeter-scale PEO microdomain alignment across the entire thickness of the film was observed when a suitable solvent vapor was employed for SVP treatment. This study again demonstrated the utility of SMT methods for characterization of the nanoscale morphology of BCP films at ambient condition and with high spatial precision.

Chapter 6 - SMT Studies of Millimeter-Scale Cylindrical Microdomain Alignment in CF-PS-*b*-PEO Films Induced by SVP

Reproduced with permission from The American Chemical Society
Published as: Tran-Ba, K.-H., Finley, J. J., Higgins, D. A., Ito, T. *J. Phys. Chem. Lett.* **2012**, *3*, 1968-1973.

6.1 Introduction

This chapter describes systematic SMT investigations of the SVP-induced microdomain alignment in CF-PS-*b*-PEO thin films.[23] Here, we attempted the fabrication of a CF-PS-*b*-PEO film comprising macroscopically aligned microdomains using SVP. The method was selected among a variety of other methods including the flow-approach (see Chapter 5) because of its simplicity and the capability to align microdomain structures across the entire film thickness.[227] Indeed, Osuji has previously reported the preparation of oriented cylindrical microdomains in SBS films by SVP with tetrahydrofuran vapors.[25] Quantitative assessment of the microdomain morphologies in these films using SAXS have revealed the overall well-organized microdomain morphologies in macroscopic sample regions. Importantly, Osuji studied the effect of the solvent vapor pressure on the microdomain alignment after a suitable solvent for SVP has been found. It is well known that the selectivity of organic solvents is crucial for the solvent-based microdomain alignment.[66] So far, the solvent effect on the SVP-induced microdomain of BCPs such as CF-PS-*b*-PEO has not been reported yet, in particular on the single-molecule level using SMT. Our investigations are aimed to provide important insights into the SVP-induced microdomain alignment and may also reveal potential mechanisms behind it through a detail characterization of the nanoscale morphology with a high spatial nanometer-scale resolution.

In this study, the effect of different organic solvent vapors with varying selectivity to PS and PEO on the SVP-induced microdomain alignment was systematically investigated.[23] Vapors of 1,4-dioxane, benzene and toluene was used for the horizontal penetration through the CF-PS-*b*-PEO films, which were sandwiched between two planar glass substrates (**Figure 6.1c**). Microdomain alignment was evaluated by recording the diffusive motions of SRB probe molecules (**Figure 6.1b**). SRB is expected to selectively partition into the cylindrical PEO microdomains

due to the complexation between Na^+ and PEO.[228] The single molecule trajectory data were analyzed using orthogonal regression methods previously developed by our group (see Chapter 3)[22] to quantitatively assess the orientation and order of the microdomains in the SVP-treated CF-PS-*b*-PEO films. The results show that highly aligned cylindrical PEO domains are obtained in films annealed by SVP methods using 1,4-dioxane. Importantly, domain alignment occurs throughout the entire μm-thick and millimeter wide films. In contrast, films treated with benzene or toluene vapors did not exhibit a long-range microdomain alignment. The SMT results also afford a quantitative measure of the PEO microdomain radius using the positional variances across the 1D trajectories. Through this work, we have identified a suitable solvent for the SVP-induced alignment of cylindrical PEO microdomains over a millimeter-scale distance in CF-PS-*b*-PEO films, and have demonstrated the utility of SMT for characterization of the nanoscale morphology in substrate-confined CF-BCP monoliths, under solvent-swollen ambient conditions.

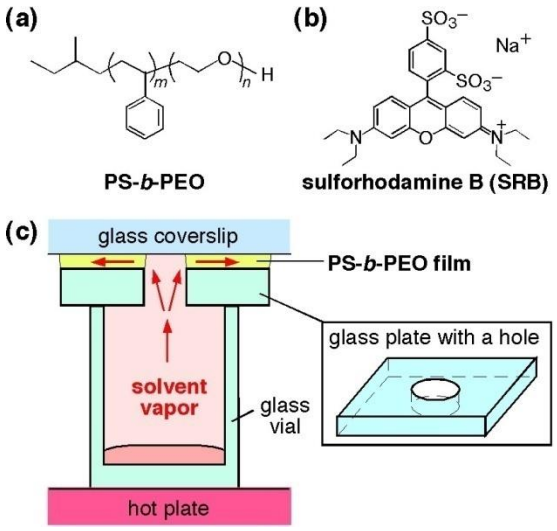

Figure 6.1. Chemical structures of (a) CF-PS-*b*-PEO and (b) SRB dye. (c) Experimental setup employed for SVP. A CF-PS-*b*-PEO film is sandwiched between a glass coverslip and a glass plate with a hole. The hole allowed the films to be exposed to solvent vapor via their edges. The temperature of the hot plate was controlled to obtain a similar solvent vapor pressure (ca. 0.5 atm) within the glass vial for all solvents employed. Solvent vapor horizontally penetrates through the CF-PS-*b*-PEO film from the hole to the edge of the glass plate. Reprinted with permission from Ref (23). Copyright 2012 American Chemical Society.

6.2 Experimental Section

6.2.1 Sample Preparation

Dye-doped CF-PS-*b*-PEO (Polymer Source; PS, M_n =47 000 g/mol; PEO, M_n =7 000 g/mol; PS volume fraction ~ 0.785; M_w/M_n = 1.07) sandwich films for SMT experiments were prepared as follows. A polymer layer was drop-cast from a 7% (w/w) benzene solution of CF-PS-*b*-PEO containing SRB (the dye concentration was ~5 nM in the PEO domains) on a glass plate (Corning) incorporating a hole (6 mm in diameter). After drying, the glass plate was placed on a plasma-cleaned glass coverslip (FisherFinest premium) so that the deposited polymer film faced the coverslip. This assembly was then heated at 230 °C for 10 hrs under vacuum (ca. 0.3 torr). During heating, the polymer melted and sealed the gap between the two glass substrates. The film thickness was 4 ~ 10 μm, as estimated from depth-dependence SMT data and cross-sectional FE-SEM images (using a Zeiss Leo 32 SEM at the Microscopy and Analytical Imaging Laboratory, the University of Kansas). The resulting sandwiched film was then exposed to 1,4-dioxane, benzene or toluene vapor at < 20% relative humidity for one day (**Figure 6.1c**). The temperature of the hotplate was adjusted to 60 °C for benzene, 80 °C for 1,4-dioxane and 90 °C for toluene so that the film was exposed to solvent vapor of similar vapor pressure (~0.5 atm). During SVP, the whole assembly was placed within a large beaker (17 cm diameter, 9 cm height) to heat the assembly uniformly and to reduce solvent vapor condensation in the film. The films were dried in a desiccator, and then transferred to a wide-field fluorescence microscope for SMT measurements at room temperature and in air.

It should be pointed out that after a sample was dried for longer time, the regions exhibiting immobile probe molecules expanded from the edges of the film. In addition, dried films exhibited higher fluorescent background possibly due to the partial detachment of the films from the substrates. In this work, the diffusion coefficients of probe molecules are not reported since the diffusion rates are determined by the residual solvent quantities in the films. Varying diffusion coefficients of SRB probes were found when the SMT was recorded at different position x of a film or in a film dried for different duration in the desiccator.

6.2.2 Quantitative Assessment of the SMT Data

Threshold Value for Separation of 1D and 2D Trajectories. In this study, the trajectory angle error (σ_θ) was employed for distinguishing between 1D- and 2D-trajectories. A threshold σ_θ for 1D- and 2D-trajectories was determined from Monte Carlo computer simulations according to the procedures we previously reported.[1] The simulations depicting 1D motions were performed for the data analysis of the 1,4-dioxane-treated films, whereas 2D simulations were used to analyze the data of films penetrated by toluene and benzene vapors. Prior to the simulations, the signal to noise ratio, molecular survival times and diffusion coefficients (D) were determined and averaged from multiple experimental SMT videos at varying positions x of each film. These data were used as input parameters in the custom simulation software written in the National Instruments LabView programming environment. In these simulations, 20 molecules were first randomly positioned throughout the 16 x 16 μm^2 region. Molecular diffusion was simulated by selecting the frame-to-frame step size (and direction) for each molecule from a Gaussian distribution (in each dimension) having a variance of $2Dt$ (for 1D) or $4Dt$ (for 2D). In this simulation, the frame time t (0.04 s) and the diffusion coefficient D of the mobile species were set to match the experimental data. Each video was 1000 frames in length. The mean lifetime (i.e., time to photobleaching) of molecules was 0.5 s as determined from the experimental data.

For example, from SMT data recorded in the 1.4-dioxane-, benzene and toluene-treated samples (**Figure 6.4**, x = 1.5 mm), the mean diffusion coefficients of molecules were determined to be 4.6 x 10^{-9} cm^2/s (1D, 1,4-dioxane), 1.3 x 10^{-9} cm^2/s (2D, benzene) and 2.4 x 10^{-9} cm^2/s (2D, toluene), respectively. The simulated videos were analyzed by the orthogonal regression method, as with the experimental videos. **Figure 6.2** depicts the histograms of trajectory angle errors obtained from the simulations based on the parameters measured in the 1,4-dioxane-treated film. A Log Normal fit to the data, which is represented by the bold curve in **Figure 6.2**, was used to determine the probability that 1D-diffusing molecules would be erroneously classified as 2D-diffusing. From the Log Normal fit, the average (μ) and the standard deviation (σ) of trajectory angle errors could be determined. Hence, the threshold trajectory angle error separating 1D and 2D diffusing molecules could be then calculated as 6.0° (= μ + 1.64σ) at 95% confidence interval. Here, trajectories having $\sigma_\theta < 6.0°$ were classified as 1D-diffusing molecules, while those with $\sigma_\theta \geq 6.0°$ were classified as 2D-diffusing or immobile molecules. The area under the Log Normal fit above the threshold was 5 % of the total area under the curve, indicating a 5 % error rate at which

2D trajectories will accidentally be classified as 1D-trajectories. We also did the simulation of 2D trajectories by using the same input parameters as in the simulation of 1D trajectories predominantly found in the 1,4-dioxane treated films. As a result, a 20 % error rate was determined indicating that 20 % of 2D trajectories will be accidently classified as 1D. However, apparently no 2D trajectories are present in SVP films of 1,4-dioxane. **Figures 6.2bc** show the distributions of the trajectory angle errors obtained from simulations on the parameters measured in the benzene- and toluene-treated films, respectively. The threshold value was found for the 2D species as $\sigma_\theta = 1.5°$ for both cases. Hence, trajectories having $\sigma_\theta < 1.5°$ were classified as 1D, while those with $\sigma_\theta \geq 1.5°$ were classified as 2D-moving or immobile molecules.

Threshold Value for Separation of 2D and Immobile Populations. In this study, we distinguished between 2D and immobile trajectories based on the positional error (σ_{other}). This parameter was estimated from the position errors obtained from immobile molecules in a SMT video recorded in a 1,4-dioxane-treated CF-PS-*b*-PEO film. First, 1D-trajectories were separated from the 2D-trajectories/immobile population by the procedure described above.[1] The mean square displacements (MSD in nm^2/s) of the 2D/immobile trajectories were converted to the displacements R (in nm) by $R = \sqrt{MSD \cdot t}$, where t is the frame time (= 0.042 s) . A histogram of displacements R is depicted in **Figure 6.3** including a Gaussian fit as a solid curve. The latter was used to determine the threshold displacement R separating the immobile and 2D populations under the assumption that the immobile molecules offer smaller R. The mean value (μ) and standard deviation (σ) of the Gaussian curve were 5.4 nm and 5.2 nm, respectively. Thus, the threshold value that gives the 95% possibility to find the immobilized spots was found to be 13.9 nm ($= \mu + 1.64\sigma$). Hence, all species exhibiting a displacement $R \geq 13.9$ nm were classified as 2D-diffusing, while those having $R < 13.9$ nm were classified as immobile. The molecules having $R < 13.9$ nm were used to determine σ_{other}.

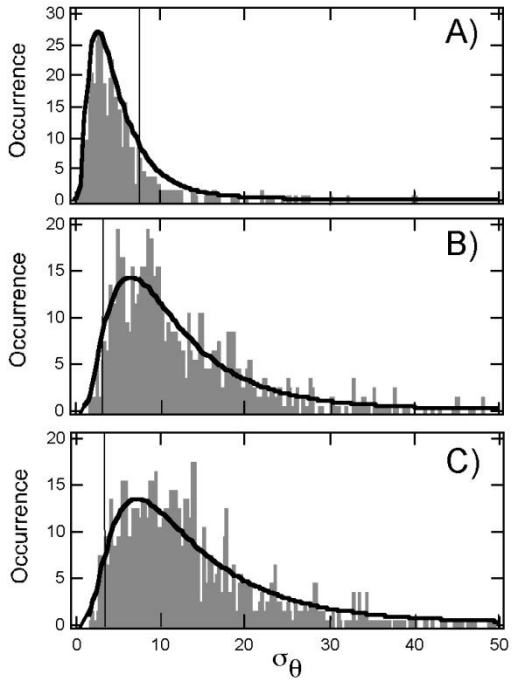

Figure 6.2. Histograms of trajectory angle errors (σ_θ) derived from a widefield video simulating A) 1D-trajectories in the 1,4-dioxane-treated film; B) 2D-trajectories in the benzene-treated film and C) 2D-trajectories in the toluene-treated film. A Log Normal fit to each data is shown by a solid curve. Reprinted with permission from Ref (23). Copyright 2012 American Chemical Society.

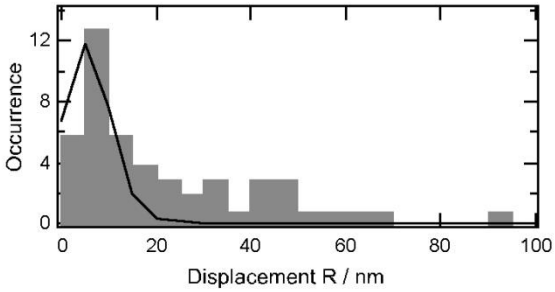

Figure 6.3. A histogram of displacements *R* of 2D/immobile species derived from a widefield video measured with a 1,4-dioxane treated film. The threshold *R* was determined from a Gaussian fit (solid curve) and was found to be 13.9 nm. Reprinted with permission from Ref (23). Copyright 2012 American Chemical Society.

6.3 Results and Discussion

6.3.1 Solvent Effect on the SVP-Induced Microdomain Alignment

Figure 6.4 depicts the trajectories, > 5 frames in length, of single SRB molecules in CF-PS-*b*-PEO films that were treated with 1,4-dioxane, benzene or toluene vapor. The SMT data were acquired from multiple regions along the solvent penetration direction (θ = 0º). The majority of the molecules in these films were found to be mobile, suggesting that their adsorption onto the substrate or absorption into PS domains was relatively minor.[229] It should be noted that some solvent must remain in the film to observe probe molecule diffusion. However, the solvent content, which significantly affected the rate of molecular diffusion, could not be precisely controlled as its evaporation depends upon ambient temperature and humidity. Thus, this work explores the dimensionality and direction of probe diffusion and probe confinement to the PEO domains, but not quantitative measurement of diffusion rates.

Single molecules in films treated with 1,4-dioxane vapor produced 1D trajectories that were oriented predominantly along the solvent penetration direction (horizontal on the images). The small deviation in the angles might come from misalignment on the microscope or nonuniform film edges. In contrast, those treated with benzene or toluene vapor showed predominantly 2D trajectories. The 1D trajectories in 1,4-dioxane-treated films were observed over distances of 2 mm. As supported by the optical fluorescent images (**Figure 5.1**), SRB is expected to preferentially partition into the PEO domains,[228] revealing their structure. The observation of 1D single molecule trajectories is therefore concluded to reflect the presence of aligned, 1D cylindrical PEO domains in 1,4-dioxane-treated films.

The paucity of 1D trajectories in films treated with benzene or toluene vapor suggests the PEO domains are not strongly aligned by these solvents. The differences between 1,4-dioxane and the other solvents are attributable to differences in solvent-PEO interactions. As suggested by their solubility parameters (δ),[230] 1,4-dioxane (δ=20.5) more selectively solvates PEO (δ = 19.6 ~ 20.2) than PS (δ=17.5 ~ 19.3). In contrast, benzene (δ = 18.8) and toluene (δ = 18.2), which have been employed previously for SVA in PS-*b*-PEO films,[84,97,101,113] have greater affinity for PS.

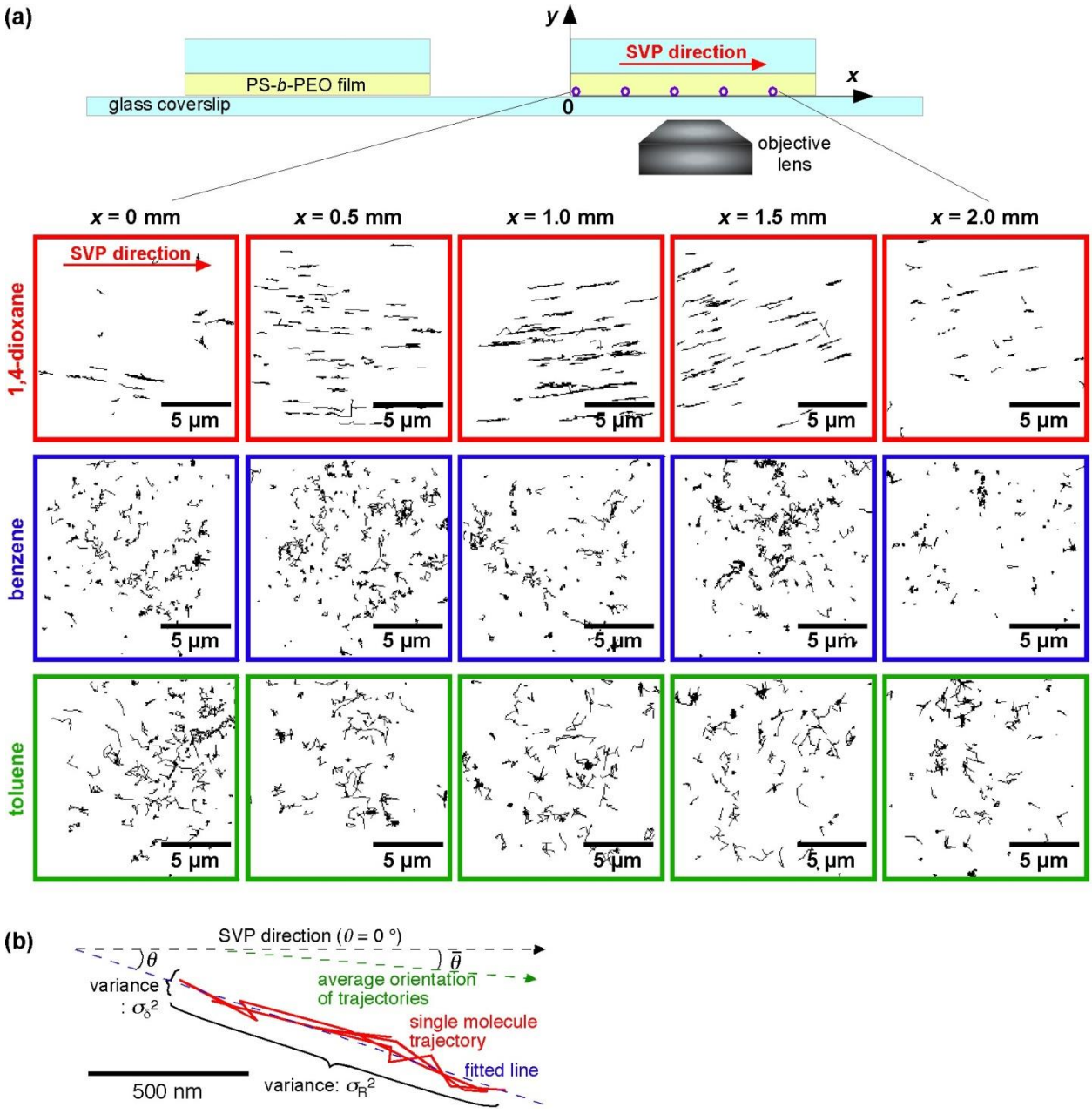

Figure 6.4. (a) Experimental setup for SMT measurements with a wide-field fluorescence microscope and trajectory data (> 5 frames in legnth) obtained from SMT videos of samples at different film depths upon the SVP of 1,4-dioxane, benzene and toluene. (b) A typical single-molecule trajectory measured in a 1,4-dioxane-treated film (red) and the best-fit line obtained by the orthogonal regression method (blue). Reprinted with permission from Ref (23). Copyright 2012 American Chemical Society.

6.3.2 Quantitative Assessment of Microdomain Order and Orientation

Quantitative assessment of the SMT data was accomplished using orthogonal regression methods,[22] which involve the fitting of individual trajectories to a straight line (**Figure 6.4b**).[22] A number of parameters are obtained as outputs, and these provide unique quantitative information on CF-PS-*b*-PEO film properties. The in-plane orientation angles, θ, of 1D trajectories provides data on the alignment of individual cylindrical domains. Also provided are the variances of molecular motion along, σ_R^2, and across, σ_δ^2, the 1D trajectories. The former is related to the diffusion coefficient for each molecule, while the latter affords a means to determine the radius of the cylindrical domains, with nanometer-scale precision. Furthermore, the associated trajectory angle error, σ_θ, given by Eq. 6.1, allows 1D and 2D trajectories to be distinguished:[22]

$$\sigma_\theta^2 = \frac{\sigma_\delta^2 \sin\theta\cos\theta}{n}\left(\frac{\sigma_\delta^2}{\sigma_R^2}+1\right) \qquad \text{(Eq. 6.1)}$$

where n is the frame number. For this analysis, Monte Carlo simulation data were employed to determine the threshold σ_θ separating the 1D and 2D populations (see **Chapter 6.2**).[22] **Figure 6.5** plots the fraction of trajectories exhibiting 1D motion (1D%) in each of the CF-PS-*b*-PEO films treated with the three solvents. The majority of the trajectories (68 -80%) in 1,4-dioxane-treated films were 1D, consistent with the presence of oriented 1D diffusion pathways for the probe molecules. Histograms depicting the trajectory population as a function of trajectory angle θ offer quantitative information on the alignment of the individual PEO domains and a complete view of the in-plane orientation distribution function, for domains that support 1D diffusion. Such data is used to determine the average alignment ($\bar{\theta}$) of the domains with respect to the solvent penetration direction and also the in-plane orientational order parameter, $\langle P \rangle$, given by Eq. 6.2:[22]

$$\langle P \rangle = 2\langle \cos\Delta\theta \rangle - 1;\ \Delta\theta = \theta - \bar{\theta} \qquad \text{(Eq. 6.2)}$$

The $\langle P \rangle$ value defines the spread in the domain orientation angles from the average alignment ($\bar{\theta}$), as projected into 2D from what is actually a 3D trajectory orientation distribution function.[231] The results of this analysis show that the average trajectory alignment was predominantly parallel to 1,4-dioxane penetration (i.e., $\bar{\theta}$ ~ 0 °, **Figure 6.6a**), consistent with the literature.[25] Furthermore, the degree of alignment was high, with $\langle P \rangle$ ~ 0.9, in central film regions (**Figure**

6.6b). Importantly, high values for 1D% and $\langle P \rangle$ as well as $\bar{\theta} \approx 0\,^{\circ}$ were observed over distances of 2-mm from the point of solvent vapor entry (**Figures 6.5** and **6.6**). The 1,4-dioxane based SVP induced PEO domain alignment with high $\langle P \rangle$ values throughout the entire sample thickness, as shown by SMT data recorded at different film depths (z = 0 – 4 μm) (**Figure 6.7**). Regardless of z, the majority of trajectories were 1D, horizontally aligned and exhibited a high orientational order as represented by $<P> > 0.8$ at the center of the film.

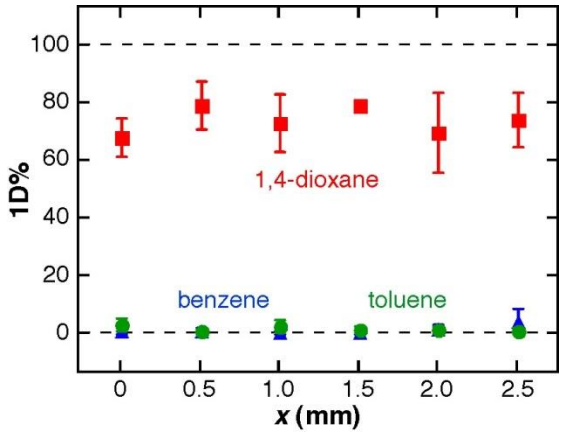

Figure 6.5. Fraction of trajectories exhibiting 1D diffusion (1D%) from SMT videos of CF-PS-*b*-PEO films at different distances x from the hole, upon the SVP of 1,4-dioxane, benzene and toluene. The error bars represent the 95%-confidence interval. Reprinted with permission from Ref (23). Copyright 2012 American Chemical Society.

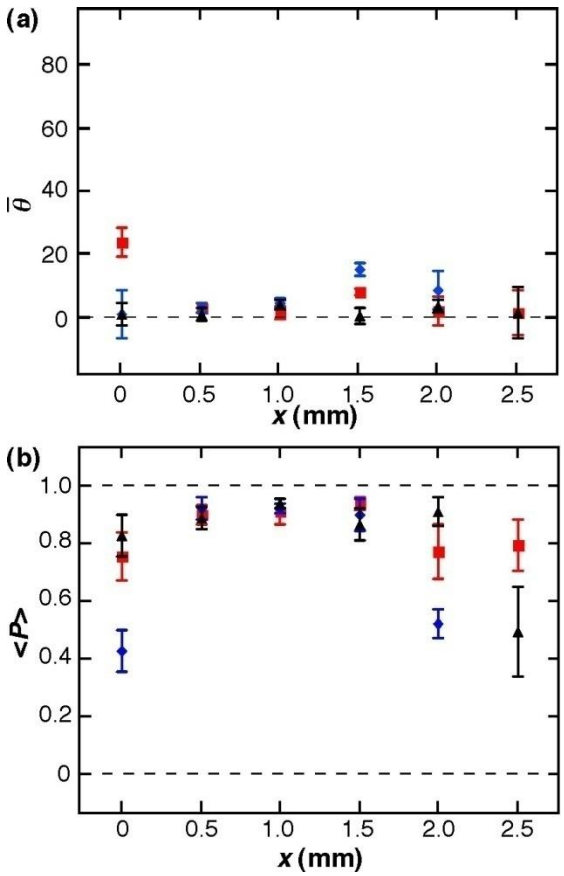

Figure 6.6. (a) Average deviation of 1D trajectories, $\bar{\theta}$, from the solvent penetration direction, and (b) order parameter $\langle P \rangle$ calculated from SMT data obtained from 1,4-dioxane-treated films at different positions *x*. The data shown were obtained from three different samples, while the data shown in blue was obtained on the sample shown in Figure 6.4a (upper). Note that the data depicted in these figures were obtained from three different images at a fixed *x*. The error bars represent the 95%-confidence interval. Reprinted with permission from Ref (23). Copyright 2012 American Chemical Society.

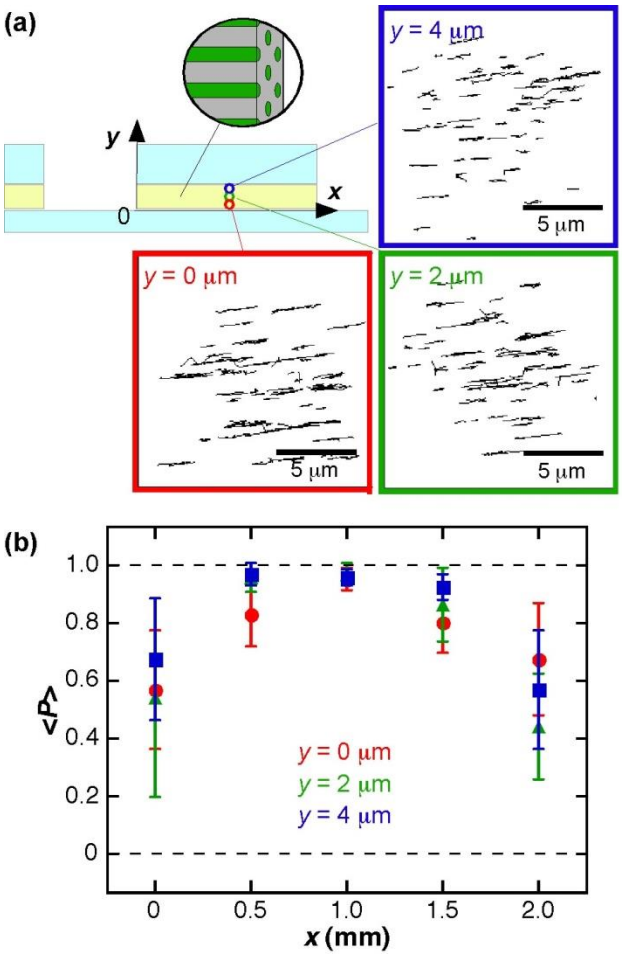

Figure 6.7. (a) Single-molecule trajectories calculated from SMT videos recorded in a 1,4-dioxane-treated film at x = 1.5 mm and three different focusing depths (y = 0, 2, 4 μm). (b) Order parameter $\langle P \rangle$ obtained from SMT videos recorded at three different depths in the CF-PS-*b*-PEO film. The error bars represent the 95%-confidence interval. Reprinted with permission from Ref (23). Copyright 2012 American Chemical Society.

6.3.3 Estimation of the Microdomain Radius

The radius of the PEO domains can be determined from σ_δ^2 of 1D trajectories recorded in SVP films with 1,4-dioxane. The sizes of the PEO domains, which are much smaller than the diffraction-limited resolution of the optical microscope, can be determined because the locations of individual molecules can be measured with nanometer-scale precision when sufficient signal to noise ratios are achieved.[140] The measured σ_δ^2 incorporates contributions from transverse molecular motions within the nanoscale domains (r^2) along with measurement errors due to the finite precision of molecule localization (σ_{other}^2).[140] The latter was estimated from the position errors obtained from immobile molecules in the same videos, as described in experimental section (**Chapter 6.2.2**). Domain radius (r) was then calculated using the following relationship:

$$\sigma_\delta^2 = \sigma_{other}^2 + r^2 \qquad \text{(Eq. 6.3)}$$

The σ_δ and σ_{other} values from the 1D trajectories in an SMT video with the highest signal-to-noise ratio, which gives the smallest error on r, were 31 ± 3 and 29 ± 4 nm, respectively, giving r = 11 ± 10 nm (average ± 95% confidence limit). The large error on the domain radius reflects the signal to noise ratio of the video and also the presence of defects in the film. Importantly, the r value from SMT is close to the domain radius (14 ± 2 nm) measured by AFM on the surface of similar CF-PS-*b*-PEO films (**Figure 6.8**), suggesting that the probe molecules mainly diffuse within *individual* cylindrical PEO domains. **Figure 6.9** shows an SEM image of a exposed (top glass detached) CF-PS-*b*-PEO film treated by SVP with 1,4-dioxane. The presence of aligned nanostructures can be clearly seen with a periodicity around 30 nm, consistent to the results of AFM and SMT measurements.

The predominance of 2D trajectories observed in films treated with benzene or toluene vapor indicates that these solvents are not suitable for SVP-based alignment of cylindrical PEO microdomains in CF-PS-*b*-PEO films. Poor microdomain alignment in this case might seem to contradict previous reports of SVA-based alignment of PEO in thin CF-PS-*b*-PEO films using these same solvents.[97,101] However, SVA in the prior work induced vertical (i.e., perpendicular) domain alignment in films of limited thickness (≤ 0 5 μm). The edges of our sandwiched films, where solvent evaporates to the air, were nonuniform, as suggested by the smaller $\langle P \rangle$ values in **Figure 6.6b**. Thus, even if the cylindrical PEO domains in our films were aligned by solvent

evaporation, the alignment would be difficult to detect over such short distances by SMT. Therefore, we believe that the 2D trajectories recorded in these films reflect the reptated, worm-like structure of the PEO domains formed *within* the CF-BCP films, in the absence of external fields.[94] The importance of solvent vapor-PEO interactions in producing aligned domains in CF-PS-*b*-PEO films was consistent with literature reporting domain alignment using humidified benzene vapor.[97,113] The preferential partitioning of water into the cylindrical PEO domains during SVA enhanced the microdomain alignment.[112,113]

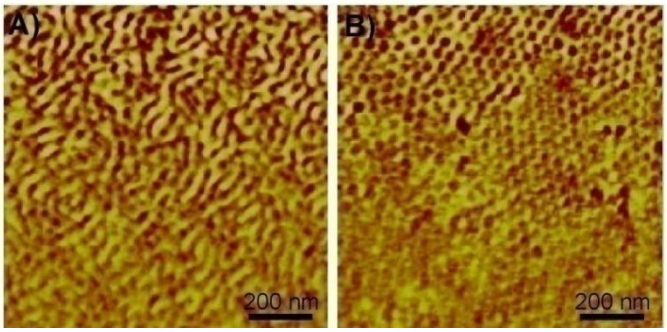

Figure 6.8. AFM phase images of a thin CF-PS-*b*-PEO film (a) before and (b) after SVA with 1,4-dioxane. The film was prepared by spin coating from an 1% w/w toluene solution at 3000 rpm for 30 s. Its ellipsometric thickness was *ca*. 50 nm. Improved perpendicular alignment of cylindrical PEO microdomains was observed after solvent annealing (right). Reprinted with permission from Ref (23). Copyright 2012 American Chemical Society.

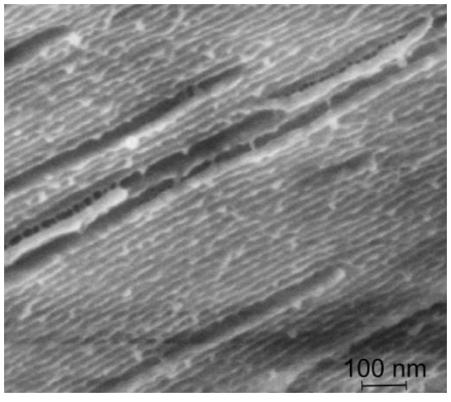

Figure 6.9. A SEM image of a 1,4-dioxane-treated CF-PS-*b*-PEO film. The exposed film was prepared for SEM by detachment of the top glass after complete solvent evaporation. PS domains were stained with osmium oxide prior to SEM, thus PS appeared darker than PEO.

6.4 Conclusions

In summary, we have quantitatively assessed the alignment of cylindrical microdomains in CF-PS-*b*-PEO thin films by SMT. The results demonstrate that penetration of 1,4-dioxane induced the alignment of cylindrical PEO domains in these films, and that these domains confine the diffusive motions of SRB molecules in 1D. In contrast, benzene and toluene vapors did not induce long-range domain ordering, resulting in the observation of 2D molecular motions. The alignment of the cylindrical PEO domains was quantitatively assessed based on 1D%, σ_δ, $\bar{\theta}$ and $\langle P \rangle$ parameters obtained from an orthogonal regression analysis of the SMT data. CF-PS-*b*-PEO films treated with 1,4-dioxane exhibited a predominance of 1D PEO domains (1D% ≈ 75%) with a high orientational order ($\langle P \rangle \approx 0.9$) aligned in the direction of solvent penetration ($\bar{\theta} \sim 0°$) over millimeter length scales. SMT data were also employed to determine the PEO domain radius. The value obtained (*ca.* 11 nm) was close to that determined on the film surface by AFM methods (*ca.* 14 nm). These results demonstrate the utility of SMT methods for characterization of nanoscale domains in cylinder-forming block copolymer films. The simple approach reported here for the fabrication of CF-PS-*b*-PEO monoliths comprising well-aligned cylindrical PEO domains will facilitate the application of CF-PS-*b*-PEO monoliths for templates in nanomaterials synthesis and chemical separations/sensing.

Importantly, microdomain structures observed so far, representing the shorter-range (μm-scale) material properties of CF-PS-*b*-PEO films through the single-molecule diffusion trajectories.[17] Unfortunately, these trajectory data only offer poor information on the effective nanostructure length because of the limited life time of the probe molecules during the SMT measurements using an intense laser light during SMT measurements. The estimation of the effective continuity of the nanostructures and their accessibility for molecules is highly essential for potential applications, defining their efficacy.[2] In the next study, we employed FRAP for investigations of the longer-range material characteristics in a CF-PS-*b*-PEO film. FRAP was used because of its simplicity and more importantly the capability for integration into a wide-field microscope (as used for SMT measurements).[146] Complementary information on the material characteristics can also be obtained through this setup in a series of FRAP and SMT measurements in identical sample regions. More importantly, the results also provide a quantitative measure of the effective microdomain connectivity as reflected by the SRB diffusion over longer μm-scale distances.

Chapter 7 - FRAP and SMT Diffusion Measurements of Anisotropic Diffusion in a CF-PS-*b*-PEO Film.

Reproduced with permission from The American Chemical Society.
Published as: Tran-Ba, K.-H., Higgins, D. A., Ito, T. *Anal. Chem.* **2015**, *87*, 5802 - 5809.

7.1 Introduction

This chapter describes the ensemble and single-molecule diffusion measurements within identical regions of a CF-PS-*b*-PEO film using FRAP and SMT.[1] Here, we successfully extend the FRAP capability of our wide-field fluorescence microscope (as used for SMT) for the assessment of the ensemble diffusion of molecules over a longer-range (>10 μm), characterizing the μm-scale microdomain continuity of the film. We specifically choose FRAP over other conventional ensemble methods because it offers spatially-averaged information for a smaller microscopic sample region as compared to NMR or flux measurements.[146] As previously reported, FRAP could be used to reveal important differences in the molecular mobility at different μm-scale regions of a nanotubes with tens of a micron in length.[194] The single microscopy setup with FRAP and SMT capability also permits the assessment of complementary information of morphology and mass-transport in a series of FRAP and SMT measurements. The results of the investigation afford an advanced characterization of the 1D nanostructures, thus deepen our knowledge on the mass-transport and material characteristics in CF-PS-*b*-PEO.

In this study, a series of FRAP and SMT measurements were performed in a CF-PS-*b*-PEO film (*ca*. 4 μm thick) with aligned cylindrical PEO microdomains containing 10 μM SRB probe molecules induced by directional SVP of 1,4-dioxane (see Chapter 6). The ensemble diffusion behavior of SRB in the PEO microdomains was assessed in FRAP studies of circular photobleached regions (*ca.* 7 μm in diameter). The SRB concentration was subsequently reduced by additional photobleaching, and the diffusion of individual SRB was explored using SMT in the identical area. The FRAP data showed anisotropic fluorescence recovery, yielding the average microdomain orientation. Importantly, the extent of fluorescence recovery observed (*ca.* 90%) permitted the quantification of long-range microdomain connectivity. In addition, the recovery time dependence provided an ensemble measurement of the SRB diffusion coefficient within the cylindrical PEO. The SMT data exhibited 1D diffusion of individual SRB molecules along the

SVP direction across the entire film thickness, as consistent with the FRAP results. The average of the single-molecule diffusion coefficients was close to the value obtained from FRAP measurements in the identical area. The implementation of FRAP and SMT measurements in identical areas provides complementary information on the material properties and molecular diffusion with minimal influence of sample heterogeneity.

7.2 Experimental Section

7.2.1 Chemicals and Materials.

CF-PS-*b*-PEO (PS, M_n = 42 000 g/mol; PEO, M_n = 11 500 g/mol; PS volume fraction 0.8; M_w/M_n = 1.07) was purchased from Polymer Source and used as received. Toluene (HPLC grade); 1,4-dioxane (HPLC grade); methanol (HPLC grade) and SRB (ACS grade) were purchased from Acros Organics and used without further purification.

7.2.2 Sample Preparation.

A CF-PS-*b*-PEO film comprising cylindrical PEO microdomains aligned along a controlled direction was prepared using our previously reported procedure.[23] Briefly, a CF-PS-*b*-PEO solution in toluene (8% w/w; *ca.* 100 µL) containing SRB (nominally 10 µM in PEO after solvent evaporation) was drop-cast on a glass plate (FisherFinest Premium; *ca.* 15 x 15 mm^2, 1 mm thick) having a circular hole (*ca.* 6 mm in diameter) at its center. The polymer sample was dried on a hotplate (*ca.* 50 °C) for 30 min, placed on a glass coverslip (FisherFinest Premium; 25 x 25 mm^2, 0.2 mm thick), and melted in a vacuum oven (< 1 Torr) at 240 °C for six hours to obtain a uniform film sandwiched between the two glass substrates. The sandwiched film was treated by 1,4-dioxane vapor at 80 °C in a nitrogen-filled glove box for one day so that the vapor penetrated through the film from the inner hole to the outer edge of the glass plate. The film was then dried at 40 °C in the glove box for two days prior to the FRAP and SMT measurements. This ensures a diffusion rate of SRB molecules suitable for these measurements.[24] The width of the film defined by the hole edge and the substrate periphery was *ca.* 2 mm. FRAP and SMT data were measured at three different positions (x = 0, 0.5 and 1 mm) measured from the inner hole edge. At x = 0 mm the data were recorded near the inner film edge where 1,4-dioxane vapor was initially introduced.

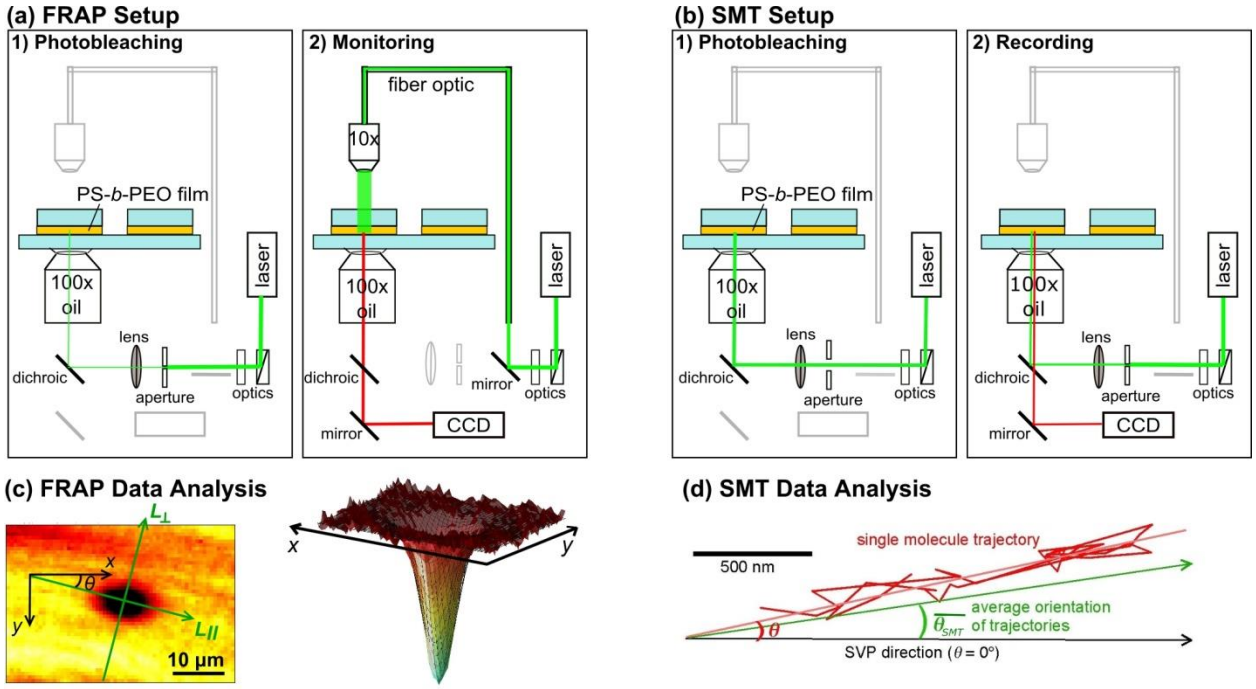

Figure 7.1. Experimental setups for FRAP and SMT measurements. (a) For FRAP measurements, a circular region (*ca.* 7 µm in diameter) in a CF-PS-*b*-PEO film was first photobleached using an intense laser pulse. Subsequently, the fluorescence was imaged by irradiating the sample with attenuated laser light from the top. (b) All SMT data were recorded (right) under broad laser illumination (*ca.* 16 x 16 µm^2) after the entire observation area was further photobleached (left) by more intense laser light. (c) A representative fluorescence image of a photobleached region in the FRAP experiment. Here, *x* and *y* were defined as the directions parallel and perpendicular to the SVP direction (left). $L_{//}$ and $L_{\perp}$ are defined to be parallel and perpendicular to the long-axis of the elliptical photobleached region observed during fluorescence recovery (see **Figure 7.3a**). The fluorescence intensity was fitted to a 2D Gaussian function (black mesh) to measure the width, $w_{//}$, of the intensity profile along $L_{//}$ (right). (d) A typical 1D single molecule trajectory (red) and its best-fit line using orthogonal regression methods. Here, θ represents the tilt angle (red) of the single trajectory with respect to the SVP direction while $\overline{\theta_{SMT}}$ depicts the average trajectory orientation from all 1D trajectories found in each set of SMT data (green). Reprinted with permission from Ref (1). Copyright 2015 American Chemical Society.

7.2.3 FRAP Measurements.

Instrumentation. **Figure 7.1a** shows the wide-field fluorescence microscope setup used for FRAP measurements. The microscope was built on an inverted epi-illumination microscope (Nikon Eclipse Ti). An argon-ion laser (λ_{ex} = 514 nm) was used for excitation and photobleaching of SRB fluorescent dyes. For photobleaching, a more intense beam (*ca.* 200 μW/μm^2) was directed through a small aperture (*ca.* 1 mm in diameter) (**Figure 7.1a**, left), before being reflected via a dichroic mirror (Chroma 555 DCLP) into the back-aperture of an oil-immersion objective (Nikon Apo TIRF 100X; 1.49 NA). The laser beam was then focused to photobleach the SRB molecules in a circular region (*ca.* 7 μm in diameter) in the CF-PS-*b*-PEO film. Immediately after photobleaching, the recovery of fluorescence in the photobleached area was recorded under broad illumination from above by attenuated laser light (*ca.* 20 μW/μm^2) delivered through an optical fiber to an air objective (Newport 10X Air; 0.25 NA) (**Figure 7.1a**, right). The fluorescence images were collected using the oil-immersion objective, passed through a dichroic mirror and a band-pass filter (Chroma, 580/40 HQ), and recorded with an electron-multiplying (EM) CCD-camera (Andor iXon DU-897). Fluorescence images were recorded as 64 pixels x 64 pixels at 4 x 4 binning and depicted 48 x 48 μm^2 sample regions (1 pixel = 0.75 μm). The exposure time was 0.2 s and the readout rate was 1 MHz with no EM-gain. At each *x*, fluorescence images were recorded with a cycle time of 5 s per frame for the first five minutes and with a cycle time of 30 s (for a duration of 10 min at x =1 mm) or 60 s (for a duration of 30 min at x = 0 and 0.5 mm) thereafter. All the data were measured upon focusing at z = 2 μm at room temperature (*ca.* 20 °C) with a relative humidity of 20 – 30%. It should be noted that the photobleached region at t = 0 s was slightly elliptical due to probe diffusion during the short delay (*ca.* 1s) between photobleaching and initial image acquisition.

Quantitative Data Analysis. In the FRAP data analysis, the photobleached region was fitted to a 2D Gaussian function to determine the major ($L_{//}$) and minor ($L_{\perp}$) axis directions, the angle (θ_{FRAP}) between $L_{//}$ and the solvent penetration direction and the full-widths (at 1/e^2 peak height) of the cross-sectional intensity profiles ($w_{//}$ and $w_{\perp}$) (Figure 1c). The following equation, which describes a rotated, elliptical 2D Gaussian function (see appendix for its derivation) was used for the fitting:[232]

$$f(X,Y) = B\text{-}A\exp\left[-\left\{\frac{(X\text{-}X_0)\cos\theta_{FRAP}+(Y\text{-}Y_0)\sin\theta_{FRAP}}{(\sqrt{2}/4)w_{//}}\right\}^2 - \left\{\frac{-(X\text{-}X_0)\sin\theta_{FRAP}+(Y\text{-}Y_0)\cos\theta_{FRAP}}{(\sqrt{2}/4)w_{\perp}}\right\}^2\right] \quad \text{(Eq. 7.1)}$$

In this equation, A is the amplitude of the intensity profile. X_0, Y_0 and B correspond to the center position of the photobleached area (X_0, Y_0) and the background fluorescence intensity from the prebleached image (B).

Theoretical Simulation. Subsequently, an ensemble diffusion coefficient, D_{FRAP}, was determined by numerically fitting the time dependence of $w_{//}$ to a 1D diffusion model. The model assumes (i) the recovery originates purely from the diffusion of fluorescent molecules with a constant time-independent diffusion coefficient along $L_{//}$ according to Fick's second law (Eq. 7.2), for $t > 0$);[146] (ii) the fluorescence profile of the photobleached spot can be described by a Gaussian (Eq 7.3),[146] in which $X = L_{eff}/2$ represents the center of the spot; (iii) diffusion occurs symmetrically toward $X = L_{eff}/2$ within 1D microdomains of a finite total length of L_{eff} ($0 \leq X \leq L_{eff}$) with boundary conditions as defined in Eq 7.4 (for $t > 0$).[233] The following equations for the concentration of fluorescent molecules, $C(X,t)$, were thus used for the fitting:

$$\frac{\partial C(X,t)}{\partial t} = D_{FRAP}\frac{\partial^2 C(X,t)}{\partial X^2} \quad \text{(Eq. 7.2)}$$

$$C(X,0) = C_0 exp[-\alpha T I(X)],\ I(X) = \left[\frac{8P_0}{\pi w^2}\right]\exp\left(\frac{-8\left(X-\frac{L_{eff}}{2}\right)^2}{w^2}\right) \quad \text{(Eq. 7.3)}$$

$$\left[\frac{\partial C(X,t)}{\partial X}\right]_{X=0} = \left[\frac{\partial C(X,t)}{\partial X}\right]_{X=L_{eff}} = 0 \quad \text{(Eq. 7.4)}$$

In Eq. 7.3, T is the photobleaching time, α is the photobleaching rate constant for an irreversible first-order reaction, w is the full-width at $1/e^2$ peak height and P_0 is the total laser power.[146] A Matlab program was used for fitting of the FRAP data to obtain parameters D_{FRAP} and L_{eff} along with their standard errors. It employed built-in functions: The 'pdepe' function was used to numerically solve the equations (Eqs. 7.2-7.4) while the 'lsqcurvefit' function was used for data fitting. The 'nlparci' function was used to estimate a fitting error that reflects the residuals of all data points to the fitting lines.

7.2.4 SMT Measurements.

Instrumentation. All SMT data were collected using a similar wide-field fluorescence microscope setup (**Figure 7.1b**) as employed for FRAP. The setup was previously described in detail by us (see Chapter 5 and 6).[22] In this setup, the single molecule fluorescence was excited and collected using the same 100x oil-immersion objective. Experimentally, a 514 nm laser light of higher intensity (*ca.* 100 μW/μm^2) was first used for photobleaching (for *ca.* 30s) of the majority of SRB dye molecules at a wider areas of interest (*ca.* 30 x 30 μm^2) that included the FRAP area. For such purposes, a broader laser beam that was defined by a larger aperture (*ca.* 10 mm in diameter) was focused on the sample. Subsequently, the single molecule diffusion was recorded at narrower area (*ca.* 16 x 16 μm^2) by exciting the fluorescence using a focused narrower, weaker laser beam (*ca.* 100 μW/μm^2) defined by a smaller aperture (*ca.* 5 mm in diameter). Such procedure allowed us to record SMT data in the samples initially doped with a μM dye concentration. At x = 0 and 0.5 mm, SMT videos were 1000 frames in length and were recorded with a cycle time of 40 ms. Due to higher probe mobility at x = 1 mm, the SMT videos were recorded with a cycle time of 20 ms and were 3000 frames in length. All SMT videos were recorded with electron-multiplying gain of 30 and readout rate of 10 MHz. These data were collected of 16 x 16 μm^2 film regions as 128 pixels x 128 pixels data (1 pixel = 125 nm). Note that an additional 1.5 x magnification built into the microscope was used to obtain a larger single molecule spots in the SMT videos. At each x, five SMT videos were recorded across the film thickness at different vertical positions z (= 0, 1, 2, 3 and 4 μm). Prior to the SMT data analysis, the videos recorded at x = 0 and 0.5 mm were cropped to 90 pixels x 90 pixels and 70 pixels x 70 pixels, respectively. This procedure was required to exclude the high background intensity at the edges of the original videos. At x = 1 mm, the original SMT videos was used without cropping.

SMT Data Analysis. The SMT data were quantitatively assessed using the orthogonal regression methods as previously reported by us. Briefly, single-molecule trajectories were generated by linking the positions of individual molecules in consecutive frames of a SMT video. The positions of those molecules in each video frame were identified by employing the ParticleTracker plugin for the ImageJ software. In this study, single molecule trajectories, >12 consecutive frames in length, were analyzed using the orthogonal regression methods. In these

methods, each trajectory was fitted to a best-fit line, providing variances in the single molecule position along (σ_R) and across (σ_δ) the trajectory as output.

These parameters were employed to distinguish the 1D, 2D and immobile trajectories that reflect 1D-diffusing, 2D-diffusing and immobile molecules, respectively, according to the following procedure. First, immobile and 1D/2D trajectories were separated based on σ_R: Trajectories with σ_R > 44 nm were classified as 'mobile' (1D/2D) while trajectories $\sigma_R \leq 44$ nm were classified as 'immobile'. Next, 1D and 2D trajectories were distinguished based on σ_δ: Trajectories with σ_δ > 56 nm were classified as 2D while those with $\sigma_\delta \leq 56$ nm were classified as 1D. The threshold values of σ_R and σ_δ were determined from simulated results on single molecule diffusion obtained using the Monte Carlo method under the assumptions of signal to noise ratios and diffusion coefficients similar to the experimental data.

As output parameter, the tilt angle, θ, of 1D trajectories is provided, allowing the transport direction and thus orientation and order of the cylindrical PEO domains to be characterized. The single molecule diffusion coefficients, D_{SMT}, were estimated by fitting the relationship of time and Mean-Square-Displacement (MSD) to the following function:

$$MSD = 2nD_{SMT} \qquad \text{(Eq. 7.5)}$$

where n is the dimensionality of diffusion (e.g. n = 1 for 1D diffusion) and t (≤ 5) is the maximum time lag used for this analysis.[192] The maximum time step employed was five because the trajectories were relatively short (> 12 frames). The in-plane orientation of individual 1D trajectories was discussed based on the tilt angle (θ) of the best-fit line relative to the SVP-direction ($\theta = 0°$). The average in-plane orientation ($\overline{\theta_{SMT}}$) of 1D trajectories reflects the average alignment of the cylindrical microdomains.

7.3 Results and Discussion

7.3.1 Experimental Design for FRAP-SMT Measurements at Identical Film Regions.

In this study, FRAP and SMT data were measured in three identical areas of a CF-PS-*b*-PEO film using a wide-field fluorescence microscope (**Figure 7.1ab**). The following four issues were considered in designing the FRAP-SMT experiment using the single microscope setup.

1.) First, a probe concentration suitable for FRAP is significantly higher than that for SMT.[234,235] Thus, the initial SRB concentration in the PEO microdomains was adjusted to be 10 μM, which is suitable for FRAP measurements (**Figure 7.1a**). Subsequently, the probe concentration in a wider area was reduced via photobleaching for the SMT measurements (**Figure 7.1b**, left). It should be noted that the initial concentration of 10 μM indicates the presence of approximately two SRB molecules per μm length in each cylindrical microdomain (22 nm in diameter).[23] Thus, interactions between probe molecules should be negligible.

2.) FRAP requires the photobleaching of a smaller area than SMT. Thus, a tunable aperture was used to define the size of the laser beam directed into the 100x oil immersion objective to obtain circular photobleached areas of *ca*. 7 μm (for FRAP) and *ca.* 30 μm (for SMT) diameters (**Figure 7.1a**, left and **Figure 7.1b**, left).

3.) Third, FRAP requires broad illumination of the sample with relatively weak intensity excitation light to avoid photobleaching during monitoring of the fluorescence recovery (**Figure 7.1a**, right). Thus, a low-magnification (10x) air objective was used for the illumination of the sample from the upper side, with light delivered to the objective using an optical fiber. A neutral density filter was used to attenuate the light. Fluorescence images were recorded from a relatively wide area (*ca*. 45 x 45 μm^2) for the accurate assessment of cross-sectional fluorescence intensity profiles (**Figure 7.2**).

4.) Finally, SMT data were obtained from a narrow region (*ca*. 16 x 16 μm^2) near the center of the circular photobleached area (*ca*. 30 μm in diameter). Wide-field videos of the single molecule motions were recorded for a sufficient period of time (*ca*. 1 min) for accurate measurement of diffusion coefficients with negligible influence of fluorescence recovery.

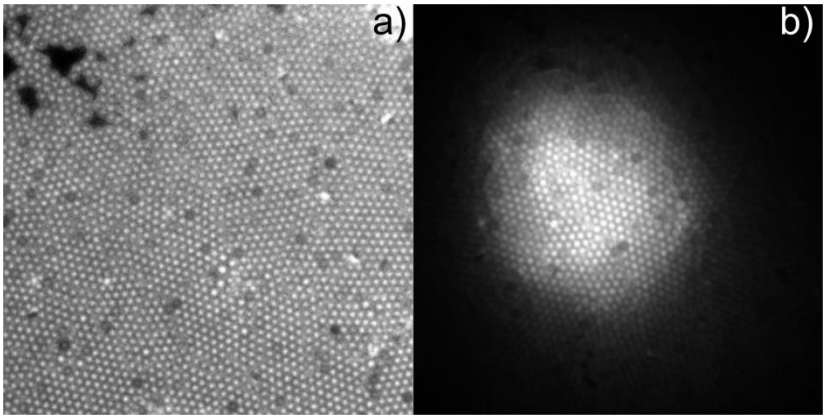

Figure 7.2. Wide-field fluorescence image of polystyrene beads (ca. 1 μm in diameter) at the identical region (45 x 45 μm^2) (a) using top-illumination via a 10x objective lens and (b) epi-fluorescence illumination via a 100x objective lens.

7.3.2 FRAP Measurements.

Figure 7.3a depicts representative wide-field fluorescence images recorded before (*prebleach*) and after photobleaching at three different positions (x). Here, x represents the distance from the inner edge (x = 0 mm) of the circular hole in the substrate along the SVP direction, as represented by the black arrows in the top images.[23] **Figure 7.3a** clearly shows anisotropic broadening of the photobleached regions, together with gradual recovery of the fluorescence intensity. The direction of the major axis ($L_{//}$) of the resulting elliptical region was observed to be close to the SVP direction, as indicated by $\overline{\theta_{FRAP}} \approx 0$ (**Table 7.1**). The elliptical broadening is fairly symmetric to the photobleached area. The anisotropic recovery is thus attributable to diffusion by intact SRB molecules from unphotobleached regions along the aligned PEO microdomains into the photobleached area. Furthermore, the recovery at x = 1 mm was significantly faster than that at the other positions, reflecting the less efficient removal of 1,4-dioxane from the film due to the longer distance from the film/air interface. The fast diffusion of SRB molecules in solvent-swollen PEO microdomains was shown previously by us using SMT.[23,24]

Effective Microdomain Length. The FRAP data also provide information on the effective microdomain length (L_{eff}) from the fraction of maximum fluorescence recovery (f_{max}). For this analysis, the fluorescence intensity, normalized to the prebleached intensity (I/I_0) and averaged

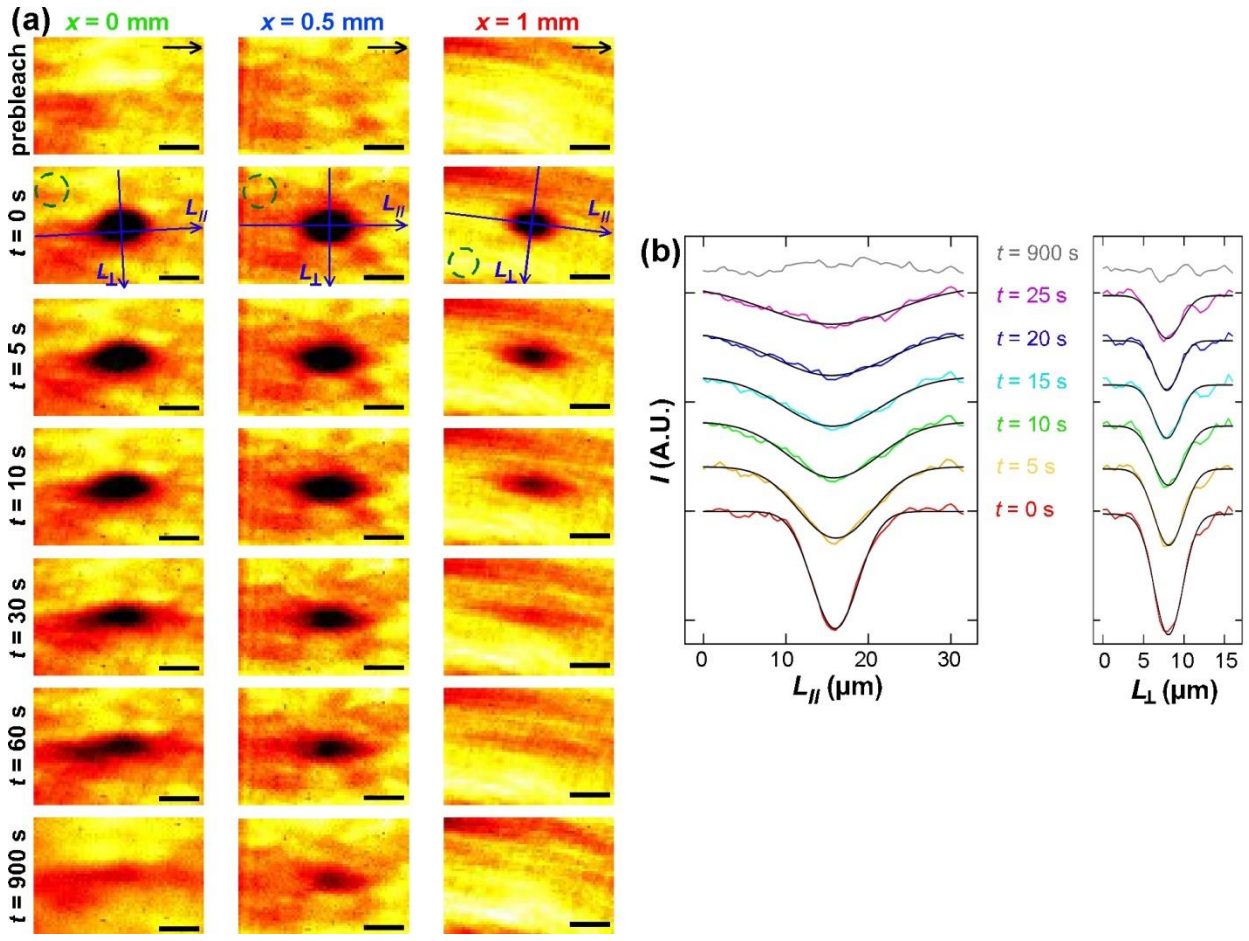

Figure 7.3. (a) Wide-field fluorescence images around the photobleached area (*ca.* 7 μm in diameter) at three different positions in the CF-PS-*b*-PEO film before (*prebleach*), just after (t = 0 s) and at longer t. The scale bar represents 10 μm. Arrows in the top images represent the SVP direction. Green dotted circles and blue arrows at t = 0 s indicate areas that gave the reference fluorescence intensities ($I^{ref}_{prebleach}$ and I^{ref}_{bleach}) and the fluorescence recovery directions ($L_{//}$/$L_{\perp}$), respectively. (b) Fluorescence intensity profiles measured along $L_{//}$ (left) and $L_{\perp}$ (right) at x = 1 mm. Also included are Gaussian fits (solid lines) employed to estimate w. Reprinted with permission from Ref (1). Copyright 2015 American Chemical Society.

Table 7.1. Molecular Diffusion Direction, Fluorescence Recovery and Diffusion Coefficients Measured from Identical Sample Areas in the CF-PS-*b*-PEO film using FRAP and SMT.

x *(mm)*	$\overline{\theta_{FRAP}}$ *(°)*[a]	$\overline{\theta_{SMT}}$ *(°)*[b]	f_{max}	L_{eff} *(μm)*[c]	D_{FRAP} *(μm²/s)*[c]	$\overline{D_{SMT}}$ *(μm²/s)*[b]
0	0 ± 1	0 ± 4	0.94	125	1.0 ± 0.3	1.0 ± 1.2
0.5	-2 ± 1	2 ± 16	0.84	47	1.5 ± 0.7	1.1 ± 1.1
1	7 ± 1	9 ± 5	0.94	113	4.4 ± 0.7	1.8 ± 1.7

[a] The direction of fluorescence recovery obtained by 2D Gaussian fitting of the FRAP data (**Figure 7.1c**). Average and standard deviation from 49 data measured at different recovery times (*t*) at each *x*. [b] Average and standard deviation measured from 1D trajectories in SMT data. For each *x*, five SMT videos were recorded at *z* = 0, 1, 2, 3 and 4 μm. The number of 1D trajectories analyzed was 207, 332 and 653 at *x* = 0, 0.5 and 1 mm, respectively (**Table 7.3**). [c] Determined from the widths of cross-sectional intensity profiles in the $L_{//}$ direction ($w_{//}$; **Figure 7.3b**). The time course for $w_{//}$ reflecting the broadening of a Gaussian intensity profile was fitted using Fick's second law for 1D diffusion (**Figure 7.4**). The error represents the 95% confidence limit estimated from the residuals of individual data points from the best-fitted curve. Reprinted with permission from Ref (1). Copyright 2015 American Chemical Society.

within a circular region of diameter $w_{\perp}$ (6.8 μm for x = 1 mm and 7.5 μm for x = 0 and 0.5 mm), which corresponds to the initially photobleached area, was obtained (see Eq (7.6)). The equation also accounts for a gradual photobleaching across the area imaged during the fluorescence recovery measurements:[236]

$$I/I_0 = \frac{(I_{bleach}-BG)/(I_{prebleach}-BG)}{(I^{ref}_{bleach}-BG)/(I^{ref}_{prebleach}-BG)} \qquad \text{(Eq. 7.6)}$$

In this equation, *BG* is the background fluorescence intensity at the spot measured upon complete photobleaching after the FRAP-SMT measurements; $I_{prebleach}$ and I_{bleach} represent the fluorescence intensities at the photobleached spot before and after the photobleaching, respectively, and $I^{ref}_{prebleach}$ and I^{ref}_{bleach} the corresponding fluorescence intensities in the reference area (shown by the green dotted circles in **Figure 7.3a**). The I/I_0 values at the three positions were plotted as a function of time, t (**Figure 7.4**). As anticipated from the data, I/I_0 gradually increased and reached maximum values of f_{max} = 0.84 ~ 0.94 at $t \geq 25$ min, (**Table 7.1**). Assuming a uniform distribution of fluorescent probes within the microdomains upon maximum recovery, L_{eff} can be estimated to be 47 ~ 113 μm from f_{max} using $L_{eff} = w_{\perp}/(1 - f_{max})$ (**Table 7.1**). This result suggests that the cylindrical microdomains provide fairly long pathways for diffusion of the fluorescent molecules. Similar long-distance information is difficult to obtain using SMT due to the limited trajectory lengths brought about by photobleaching of the molecules (*vide infra*).

It should be noted that most previous FRAP studies employed the t-dependence of I/I_0,[146,237] as shown in **Figure 7.4**, to obtain a diffusion coefficient. In this study, D_{FRAP} was, however, not determined from **Figure 7.4**, because the circular photobleaching spot is not ideal to analyze the fluorescence recovery based on 1D diffusion. Indeed, a rectangular area is usually photobleached for investigation of 1D diffusion.[238] Here, D_{FRAP} was determined from the t-dependence of the width of a cross-sectional intensity profile ($w_{//}$) as was previously employed in some studies.[239,240]

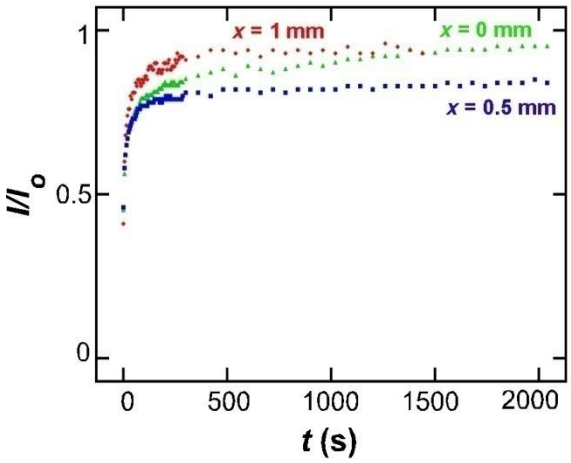

Figure 7.4. The recovery of the normalized fluorescence intensity, I/Io, measured from the photobleached circular area as a function of t and at the three different x. The fluorescence intensity was averaged over a circular region of 7.5 μm (x = 0 and 0.5 mm) and 6.8 μm (x = 1 mm) in diameter. The maximum recovery values, fmax, was estimated as the arithmetic mean of the last ten data points of the curves. Reprinted with permission from Ref (1). Copyright 2015 American Chemical Society.

Figures 7.3b depicts typical cross-sectional intensity profiles along the $L_{//}$ (left) and $L_{\perp}$ (right) directions recorded at different *t*. The profiles clearly show the gradual recovery of the fluorescence intensity. Importantly, the $L_{//}$ profile broadens with *t* (**Figure 7.3b**, left). In contrast, the $L_{\perp}$ profile showed negligible broadening during the FRAP measurement (**Figure 7.3b**, right). This observation is again consistent with the diffusion of SRB molecules along the aligned PEO microdomains. Based on the fitting of the profiles to 2D Gaussian functions (Eq. (7.1)), the profile widths in the directions of $L_{//}$ and $L_{\perp}$ ($w_{//}$ and $w_{\perp}$) were quantitatively measured for individual data. With longer *t*, $w_{//}$ gradually increased (**Figure 7.5**), whereas $w_{\perp}$ changed negligibly (data not shown). The value of $w_{//}$ increased more quickly at x = 1 mm, reflecting the faster diffusion of SRB molecules within more solvent-swollen PEO microdomains (*vide supra*). It should be noted that, ideally, $w_{//}$ should be infinitely large upon complete fluorescence recovery, regardless of the mobile molecule fraction if the microdomains were sufficiently long as compared to the imaged

area. However, the experimental $w_{//}$ reached a plateau (x = 0.5 mm in **Figure 7.5**) or could not be measured at long t accurately (x = 1 mm in **Figure 7.5**). The former probably reflects the finite length of the cylindrical microdomains, which is consistent with the incomplete fluorescence recovery shown in the analysis of I/I_0 (*vide infra*) (**Figure 7.4**). The latter is attributable to the limited S/N-ratio in the fluorescence profile data after complete recovery, preventing a 2D Gaussian fit to the data.

The t-dependent changes in $w_{//}$ were used to determine D_{FRAP} along $L_{//}$ by fitting to a 1D diffusion model based on Fick's second law. The best-fitted line for each data is depicted as a solid line in **Figure 7.5**, and the D_{FRAP} values obtained are summarized in **Table 7.1**. As anticipated from the fluorescence recovery in **Figure 7.1a**, D_{FRAP} was significantly larger at x = 1 mm than those at x = 0 and 0.5 mm. These D_{FRAP} values will be compared with single-molecule diffusion coefficients obtained from SMT measurements below.

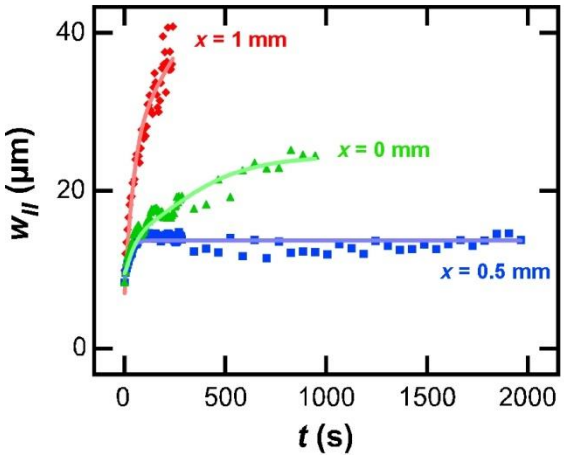

Figure 7.5. The full-width (at 1/e2 peak height), w//, of the fluorescence intensity profiles along L// measured as a function of t. The data were recorded at x = 0 (green triangles), 0.5 (blue squares) and 1 mm (red dots). The solid lines represent the best fits to the experimental data that were generated using a 1D diffusion model. Note that some portions of the data recorded at x = 0 mm (t > 945 s) and x = 1 mm (t >240 s) were not used for the analysis due to the poor S/N-ratios (< 3.29, 99.9 % CL). Reprinted with permission from Ref (1). Copyright 2015 American Chemical Society.

7.3.3 SMT Measurements.

After the FRAP data were collected, SMT data were recorded from identical regions (i.e., at the same *x*) in the same CF-PS-*b*-PEO film. Prior to data recording, the dye concentration was further reduced by photobleaching a somewhat wider area (see experimental section 7.2). **Figure 7.6** depicts single molecule trajectories, > 12 frames in length, recorded at the three different positions (*x)*. At a fixed *x*, SMT data were also recorded at different vertical positions (z = 1 - 4 μm) to observe single molecule diffusion across the film thickness. Here, the trajectories were generated by first detecting the single molecule positions in each video frame and subsequently linking their positions in consecutive frames (see experimental section 7.2). We classified and separated 1D, 2D and immobile trajectories based on a previously reported procedure (see Chapters 5/6).[23,24] 1D trajectories are shown in green (x = 0 mm), blue (x = 0.5 mm) and red (x = 1 mm), while 2D and immobile trajectories are shown in grey and black (for all *x*), respectively.

Next, 1D trajectories were quantitatively assessed by fitting each of them to a best-fit line (**Figure 7.2d**) using orthogonal regression method. This procedure provided, the tilt angle, θ, of individual 1D trajectory relative to the SVP direction as output. **Figure 7.6** (left) depicts the compiled (across z = 1 – 4 μm) histogram of θ obtained from the 1D data measured at different *x*. In each of the images, a narrow distribution that sharply peaked at zero can clearly be seen. The results indicate the presence of cylindrical PEO microdomains exhibiting of high degree of order and oriented in average in the SVP direction (θ = 0°). Indeed, the average tilt angle, $\overline{\theta_{SMT}}$, was close to zero regardless of *x* (**Table 7.1**), consistent to the FRAP's recovery directions, $\overline{\theta_{FRAP}}$, as expected. The good agreement of the FRAP and SMT results thus validate the data analysis of FRAP and SMT. Importantly, the width of the distribution of θ can be also employed to quantitatively assess the organization and order of the cylindrical microdomains. Such information cannot be provided by FRAP due to ensemble averaging of the mass-transport and nanostructure characteristics. The narrowest distribution of θ was observed at x = 1 mm, as represented by a smaller standard deviation in θ (**Table 7.1**), indicating the higher degree of orientational order of the cylindrical microdomain among the three *x* (**Table 7.2**). The result is also consistent to the previous findings of a higher symmetry and larger extent of recovery at x = 1 mm, further supporting the correlation of microdomain order and long-range connectivity.

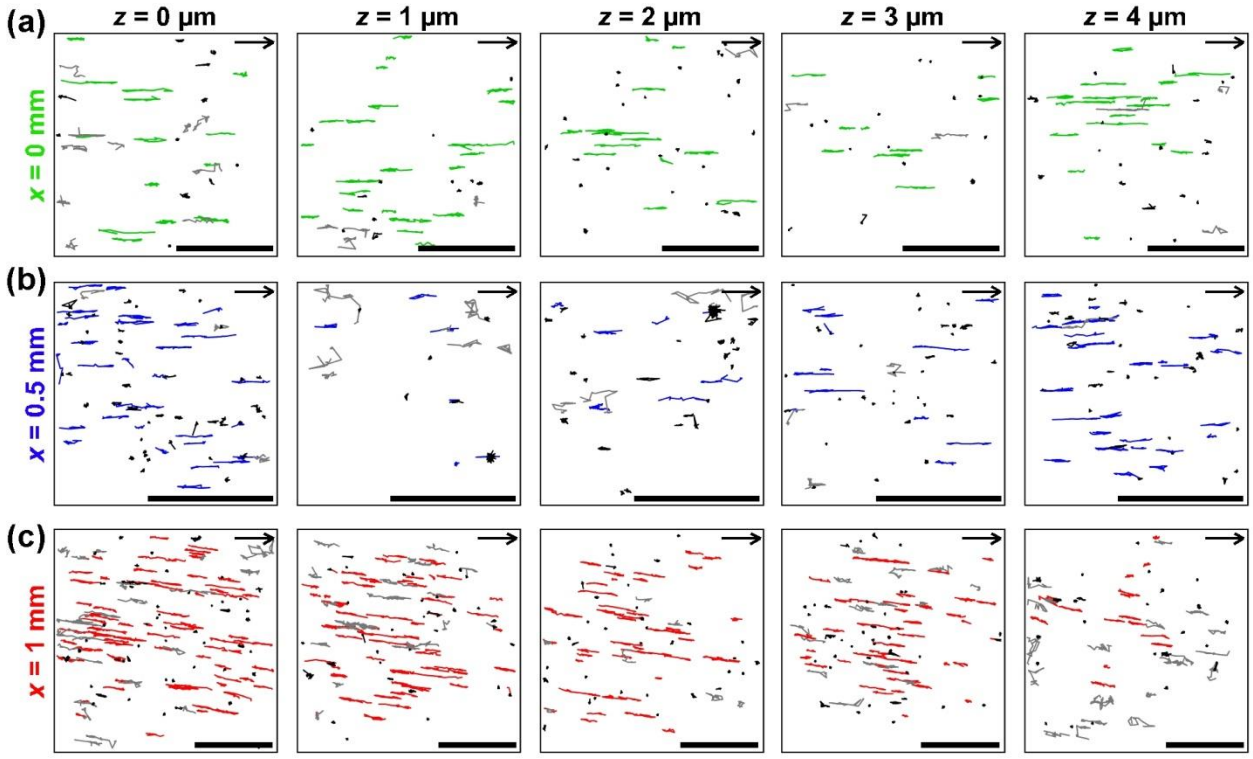

Figure 7.6. Single molecule trajectories, >12 frames in length, measured in a CF-PS-*b*-PEO film from the three identical regions used for the FRAP measurements ((a) x = 0, (b) x = 0.5 and (c) x = 1 mm). At each x, five different SMT data were recorded across the film thickness (z = 0, 1, 2, 3 and 4 μm). Note that z = 0 and 4 μm are near the polymer-glass interfaces. 1D trajectories are shown in green (a), blue (b) and red (c) while 2D and immobile trajectories are depicted in grey and black, respectively. The scale bar represents 5 μm, while the appended arrow depicts the SVP direction. Reprinted with permission from Ref (1). Copyright 2015 American Chemical Society.

Diffusion Direction. **Figure 7.6** exhibits many 1D trajectories (7-47% as the 1D fraction; **Tables 7.2** and **7.3**) regardless of x and z. These 1D trajectories were oriented parallel to the SVP

direction, as indicated by the $\overline{\theta_{SMT}}$ values close to 0° (**Table 7.1**, **Figure 7.7a**), and were highly ordered, as shown by the trajectory order parameter, <*P*>, larger than 0.76 (**Table 7.2** and **7.3**).[22] The average orientation of the individual microdomains ($\overline{\theta_{SMT}}$) at each *x* was very close to the microdomain orientation estimated from the FRAP data ($\overline{\theta_{FRAP}}$), verifying that FRAP afforded the ensemble-averaged diffusion behavior of individual molecules. It should be pointed out that the standard deviations of the $\overline{\theta_{SMT}}$ values reflect the distribution of the microdomain orientation (**Figure 7.7**), whereas the errors of the $\overline{\theta_{FRAP}}$ values primarily reflect the level of measurement precision. Considering that the individual trajectories reflect the morphologies of individual cylindrical microdomains, SMT provides quantitative information on the organization of the microdomains in contrast to FRAP.

Figure 7.6 also shows 2D and immobile trajectories that are attributable to molecules diffusing within short microdomains or to those adsorbed at the polymer-glass interface. The displacement range of the 2D trajectories was usually much shorter (< 1 μm) than that of the 1D trajectories. Thus, these molecules do not significantly contribute to the ensemble diffusion coefficients (D_{FRAP}) that mainly reflect molecular diffusion across larger μm-scale distances. The insignificant contribution of these molecules facilitates a direct comparison between single-molecule and ensemble diffusion coefficients for 1D diffusing molecules (*vide infra*). It should be pointed out that the fractions of the 1D, 2D and immobile trajectories measured with SMT do not reflect those of molecules that were present prior to photobleaching. Indeed, the fraction of 1D trajectories gradually increased upon continuous recording of SMT data due to the diffusion of intact molecules from the unbleached regions, whereas 2D and immobile molecules gradually bleached out, consistent with the mechanism of the FRAP measurements. Thus, there should be no direct correlation between the f_{max} values from FRAP (**Table 7.1**) and the 1D/2D/immobile fractions from SMT (**Table 7.2**). According to the f_{max} values from the FRAP data, the fractions of 2D/immobile molecules in the native film should be fairly low (< 10%).

Single-Molecule Diffusion Coefficients. Single-molecule diffusion coefficients, D_{SMT}, were measured from individual 1D trajectories using Eq. 7.5. **Figure 7.7b** shows the compiled (across *z*) histograms of D_{SMT} obtained from SMT data measured at the different positions. As with the trajectory angles (*vide supra*), SMT provides information on the distribution of D_{SMT}. Thus, the standard deviations of the mean values ($\overline{D_{SMT}}$ in **Table 7.1**) reflect the distribution of individual D_{SMT}, in contrast to the error of D_{FRAP} that mainly originates from the measurement precision. In addition, SMT can be used to measure molecular diffusion behavior at different *z* (**Figure 7.6** and **Table 7.3**), whereas FRAP affords the measurement of averaged diffusion behavior across the entire focal depth (here, the entire film thickness of 4 μm). At x = 1 mm, the larger fraction of 1D-diffusing molecules exhibited larger D_{SMT}, resulting in larger $\overline{D_{SMT}}$ (**Table 7.1**). The same trend was also observed for the ensemble diffusion coefficient (D_{FRAP}; **Table 7.1**). D_{FRAP} and $\overline{D_{SMT}}$ at each x were similar to each other, especially at x = 0 and 0.5 mm, verifying that the former values basically reflected the ensemble average of single-molecule diffusion behavior. The similarity of the D_{FRAP} and $\overline{D_{SMT}}$ values also imply a negligible contribution of probe-probe interactions to probe diffusion, as anticipated from the probe concentration (*vide supra*). The smaller $\overline{D_{SMT}}$ (1.8 $\mu m^2/s$) than D_{FRAP} (4.4 $\mu m^2/s$) at x = 1 mm may reflect the confined diffusion of molecules within short microdomains. Such confined diffusion is difficult to measure using FRAP, as the fluorescence recovery takes place as a result of probe diffusion over fairly long distances (> 10 μm).

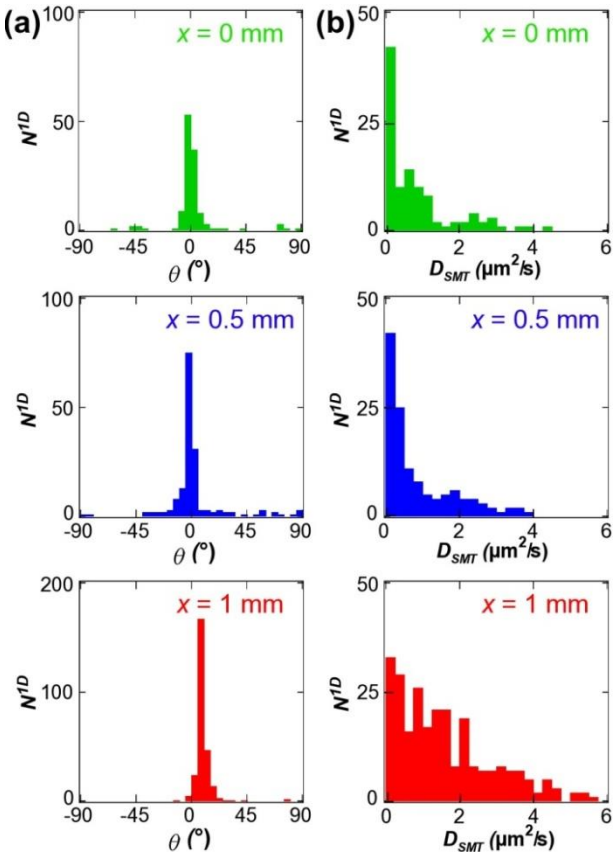

Figure 7.7. Compiled histograms depicting (a) tilt angles and (b) single molecule diffusion coefficients of the 1D trajectories (shown in **Figure 7-6**) that were measured at x = 0, 0.5 and 1 mm. $\theta \approx 0°$ represents the SVP direction. Reprinted with permission from Ref (1). Copyright 2015 American Chemical Society.

Table 7.2. Compiled Results: Total Trajectory Number, Fractions of 1D/2D/Immobile Trajectories and Trajectory Order Parameter Measured by SMT.

x *(mm)*	N [a]	f_{1D} [b]	f_{2D} [b]	$f_{Immobile}$ [b]	<P> [c]
0	207	0.42	0.16	0.42	0.98± 0.13
0.5	332	0.25	0.31	0.45	0.92 ± 0.30
1	653	0.40	0.27	0.33	0.97 ± 0.16

[a] Total number of single molecule trajectories, > 12 frames in length, obtained from five different SMT videos measured at different z (= 0 ~ 4 μm) for fixed x. [b] Fractions of 1D, 2D diffusing and immobile single molecules calculated from SMT data measured at each x. [c] Average and standard

deviation of the order parameters calculated from 1D SMT trajectories. Reprinted with permission from Ref (1). Copyright 2015 American Chemical Society.

Table 7.3. Total Trajectory Number, Fractions of 1D/2D/Immobile Trajectories, Trajectory Angle and Trajectory Order Parameter Measured at Different *z* by SMT.

x *(mm)*	z *(μm)*	N[a]	$\mathbf{f}_{1D}$[b]	$\mathbf{f}_{2D}$[b]	$\mathbf{f}_{Immobile}$[b]	$\overline{\theta_{SMT}}$ *(°)*[c]	<P>[c]
0	0	37	0.40	0.30	0.30	0± 3	1.00± 0.01
0	1	51	0.47	0.12	0.41	0± 4	0.99± 0.01
0	2	40	0.35	0	0.65	-2± 15	0.89± 0.30
0	3	28	0.43	0.43	0.14	-1± 3	1.00± 0.01
0	4	51	0.41	0.10	0.49	-1± 2	1.00± 0.01
0.5	0	94	0.31	0.19	0.50	2± 17	0.90± 0.37
0.5	1	41	0.07	0.64	0.29	-4± 3	1.00± 0.01
0.5	2	73	0.12	0.34	0.54	6± 26	0.76± 0.55
0.5	3	37	0.35	0.35	0.30	-3± 13	0.92± 0.22
0.5	4	87	0.33	0.20	0.47	0± 7	0.96± 0.10
1	0	181	0.43	0.23	0.34	9± 7	0.99± 0.02
1	1	143	0.44	0.21	0.35	11± 13	0.93± 0.30
1	2	114	0.41	0.15	0.44	8± 3	1.00± 0.01
1	3	123	0.41	0.41	0.19	7± 7	0.97± 0.15
1	4	92	0.24	0.42	0.34	10± 10	0.94± 0.10

[a] Total number of single molecule trajectories (> 12 frames in length) obtained from each of the SMT videos measured at different *z* (= 0 ~ 4 μm) and *x*. [b] Fractions of 1D, 2D diffusing and immobile single molecules calculated from each of the SMT videos. [c] Average and standard deviation of the average trajectory angles and order parameters calculated from 1D trajectories of

each of the SMT data. Reprinted with permission from Ref (1). Copyright 2015 American Chemical Society.

7.4 Conclusions

This study has demonstrated that FRAP and subsequent SMT measurements performed at identical locations provide a unique means for obtaining complementary information on molecular transport in nanostructured materials. Importantly, FRAP measurements offered ensemble-averaged data and was suitable to assess longer-range diffusion behavior, reflecting the effective microdomain length of ≥ 100 μm. The estimated effective microdomain connectivity in this study is consistent to the anticipated alignment induced by SVP. The results show that SVP is superior over the flow approach as it can produce microdomain orientation and connectivity over a longer-range. The latter measurements permitted the distribution of mass transport properties of individual molecules to be assessed. The combined FRAP and SMT measurements also offer a direct comparison of ensemble and single-molecule mass transport behavior. The two methods gave similar results on average diffusion direction and diffusion coefficient for fluorescent probe molecules within aligned cylindrical microdomains. FRAP and SMT measurements from identical sample areas provide a unique means to investigate mass transport with negligible influence of material morphological and compositional heterogeneity.

Unfortunately, the method reported here is not applicable to study molecules moving too fast or too slow: FRAP is not well suited to investigations of slowly moving molecules because of the gradual photobleaching within the observation area during fluorescence monitoring, whereas SMT cannot be used to track molecules moving too quickly because of the limited image acquisition speed of current CCD-cameras and the limited trajectory linking ability. It should be noted that, for the latter, the trajectory-profile-guided (TPG) tracking method affords reliable 1D single-molecule trajectories for quickly moving molecules as compared to conventional cost-functional methods.[241] As long as the speed of molecular motion is in the optimum range, serial FRAP and SMT measurements should be applicable for molecular transport studies not only in nanostructured materials but also in biological systems such as on cell surfaces.

Chapter 8 - General Conclusions and Future Directions

This dissertation describes the quantitative characterization of the mass-transport properties and morphologies of 1D nanostructures in STMS and CF-PS-*b*-PEO films of nanometer to micrometer thicknesses using SMT. The technique offers several significant advantages over conventional methods (e.g., AFM, SEM/TEM and SAXS) based on its capabilities to quantitatively assess the local mass-transport and material properties of 1D nanostructures with high spatial resolution. Since these processes are observed at the single molecule and single event levels, SMT offers quantitative information on the temporal and nanoscale spatial heterogeneity of the samples under various environments (e.g., in ambient air, under controlled environments and in solution).[17] Such variations are often obscured by the averaging that occurs when ensemble methods are employed. In SMT, the nanoscale material properties are simultaneously probed and quantitatively assessed by monitoring and following the diffusive motions of individual probe molecules along the cylindrical nanopores and microdomains with high nanometer-scale (*ca.* 50 nm) precision for micron-wide (e.g. 30 x 30 μm^2) sample regions, yielding the trajectories of their confined molecular pathways within the 1D nanostructures.

The quantitative assessment of mass-transport characteristics and morphology of 1D nanostructures requires a detailed analysis of the 1D single-molecule trajectory data using orthogonal regression methods.[22] The methods have provided a wealth of information on the local mass-transport and material characteristics by fitting the single-molecule trajectory data to a best fit line, yielding important parameters as outputs including trajectory angle, the angle error, and the variances of single-molecule positions along and across the trajectory direction. The trajectory angle is a quantitative measure of the in-plane orientation of the 1D nanostructures, whereas the error estimates afford useful means to distinguish 1D diffusing molecules from ones exhibiting 2D diffusion or immobile ones. The assessment of the trajectory angle distribution data permits the orientational order of the nanostructures in the materials to be determined. The orientational order can be quantified via a 2D order parameter, which relates the deviation of individual trajectories from a mean trajectory orientation. The utility of this method was initially demonstrated by its application to the analysis of 1D SMT data recorded in STMS thin films prepared using a well-established sol-gel procedure involving the vertical spin coating of its aged sol on a glass coverslip (Chapter 4).[22] The analysis provided quantitative information on the in-plane orientation of

individual cylindrical mesopores and of micron-size distinct mesopore domains. While the data depicts the presence of mesopore domains exhibiting significant variations in their average in-plane orientation between individual domains, their order parameters (and hence, mesopore order) remain relatively constant. This suggested the absence of shear forces acting on the agglomerated structures during vertical spin coating.

The usefulness of SMT for quantitative assessment of the microscale and nanoscale morphology was further demonstrated for CF-PS-*b*-PEO films prepared by a pressure-driven directional flow of concentrated CF-PS-*b*-PEO solution along a small gap formed between two glass plates (Chapter 5).[24] Directional flow is a simple method previously employed for the fabrication of macroscopically-aligned microdomains. Such a morphology is highly essential for many technological applications using BCP materials.[104] SMT could be used to quantitatively assess the alignment of individual microdomains as well as microdomain order in individual μm-scale grains from 1D single molecule diffusion trajectories. SMT permitted the characterization of microdomain morphologies across the film depth, revealing the depth-profile of microdomain orientation, consistent with a shear-flow mechanism. Interestingly, the fraction of 1D microdomains and microdomain order in individual grains remained constant regardless of the sample preparation conditions, which might reflect microdomain agglomeration morphologies in the relatively concentrated solutions. The presence of μm-scale grains in films prepared from a BCP solution was found as a possible obstacle to fabrication of macroscopically-aligned microdomains. For improving the microdomain alignment without grain structures/boundaries and across the entire film thickness, CF-PS-*b*-PEO thin films were treated by SVP with organic solvent vapors, as successfully demonstrated for cylinder-forming SBS films (Chapter 6).[23] Systematic SMT measurements at different lateral and vertical positions revealed the presence of well-aligned PEO microdomain structures across the thickness over millimeter length scales in the direction of the vapor penetration direction of 1,4-dioxane. SMT data were also employed to determine the PEO domain radius. The value obtained (*ca.* 11 nm) was close to that determined on the film surface by AFM methods (*ca.* 14 nm).[23] Unfortunately, the SMT data provide little information on the continuity of the SVP-aligned microdomains, mainly because of the limited life time of fluorescent probe molecules.

Based on its ability to probe molecular diffusion over a longer-range (>10 μm), FRAP was employed to quantitatively assess the ensemble-averaged mass-transport characteristics within

SVP-aligned microdomains, reflecting the effective microdomain length of ≥ 100 μm (Chapter 7).[1] Subsequent SMT measurements performed at identical locations provide complementary information on the local molecular transport in nanostructured materials, allowing the distribution of mass transport properties of individual nanostructures to be assessed. The combined FRAP and SMT measurements will offer a direct comparison of ensemble and single-molecule mass transport behavior with negligible influence of material heterogeneity.

This dissertation has described the application of SMT for the characterization of the nanoscale microdomain structures of CF-PS-*b*-PEO films. SMT has revealed the orientation and size of individual nanostructures, in addition to the microdomain order in these films.[17,18] A main motivation of this work is for certain the preparation and characterization of BCP materials comprising macroscopically-aligned and organized microdomains, highly essential for potential technological applications.[94] Considering that the majority of BCP applications employ nanoporous BCP films/membranes rather than native microdomain features,[9,67,242] it is clear that these nanoporous materials need to be studied by SMT methods in the near future. There are several possible challenges for the characterization of nanoporous BCP films/membranes using SMT. First, a nanoporous material containing continuous cylindrical pores aligned parallel to the underlying substrate plane has to be fabricated from a BCP precursor under selective etching and dissolution of the cylindrical microdomains.[65] This is more challenging for thicker monolithic films, particularly for materials with shorter-range microdomain alignment. Second, the SMT measurements of molecular diffusion in solution-filled nanopores are technically more challenging because of higher anticipated diffusion coefficients of probe molecules leading to possible difficulties to detect and to link the single molecule data into accurate trajectories.[243] Fortunately, Robben and coworkers have recently developed a trajectory-profile guided method for the linking of fast 1D SMT data into single molecule trajectories with a higher precision as compared to cost-functional linking routines.[241] The results of the present work have set the stage for further exciting investigations of mass-transport and morphology in well-aligned BCP materials with controllable chemistries, shape and sizes.

Chapter 9 - References

(1) Tran-Ba, K.-H.; Higgins, D. A.; Ito, T.: Fluorescence Recovery After Photobleaching and Single-Molecule Tracking Measurements of Anisotropic Diffusion within Identical Regions of a Cylinder-Forming Diblock Copolymer Film. *Anal. Chem.* **2015**, *87*, 5802 - 5809.

(2) Xia, Y. N.; Yang, P. D.; Sun, Y. G.; Wu, Y. Y.; Mayers, B.; Gates, B.; Yin, Y. D.; Kim, F.; Yan, Y. Q. One-dimensional nanostructures: Synthesis, characterization, and applications. *Adv. Mater.* **2003**, *15*, 353-389.

(3) Martin, C. R. Nanomaterials - A Membrane-Based Synthetic Approach. *Science* **1994**, *266*, 1961-1966.

(4) Masuda, H.; Fukuda, K. Ordered Metal Nanogold Arrays Made by A 2-Step Replication of Honeycomb Structures of Anodic Alumina. *Science* **1995**, *268*, 1466-1468.

(5) Bates, F. S.; Fredrickson, G. H. Block Copolymers - Designer Soft Materials. *Phys. Today* **1999**, *52*, 32-38.

(6) Brinker, C. J.; Lu, Y. F.; Sellinger, A.; Fan, H. Y. Evaporation-induced self-assembly: Nanostructures made easy. *Adv. Mater.* **1999**, *11*, 579 - 585.

(7) Baker, L. A.; Jin, P.; Martin, C. R. Biomaterials and biotechnologies based on nanotube membranes. *Crit. Rev. Solid State Mater. Sci.* **2005**, *30*, 183-205.

(8) Su, B.; Wu, Y. C.; Jiang, L. The Art of Aligning One-Dimensional (1D) Nanostructures. *Chem. Soc. Rev.* **2012**, *41*, 7832-7856.

(9) Ito, T. Block Copolymer-Derived Monolithic Polymer Films and Membranes Comprising Self-Organized Cylindrical Nanopores for Chemical Sensing and Separations. *Chem. - Asian J.* **2014**, *9*, 2708-2718.

(10) Nakanishi, K.; Tanaka, N. Sol-gel with phase separation. Hierarchically porous materials optimized for high-performance liquid chromatography separations. *Acc. Chem. Res.* **2007**, *40*, 863-873.

(11) Corma, A. From microporous to mesoporous molecular sieve materials and their use in catalysis. *Chem. Rev.* **1997**, *97*, 2373-2419.

(12) Kameta, N.; Minamikawa, H.; Masuda, M. Supramolecular organic nanotubes: how to utilize the inner nanospace and the outer space. *Soft Matter* **2011**, *7*, 4539-4561.

(13) Long, J. W.; Dunn, B.; Rolison, D. R.; White, H. S. Three-dimensional battery architectures. *Chem. Rev.* **2004**, *104*, 4463-4492.

(14) Kuchibhatla, S.; Karakoti, A. S.; Bera, D.; Seal, S. One dimensional nanostructured materials. *Prog. Mater. Sci.* **2007**, *52*, 699-913.

(15) Toksoz, S.; Acar, H.; Guler, M. O. Self-assembled one-dimensional soft nanostructures. *Soft Matter* **2010**, *6*, 5839-5849.

(16) Karger, J.; Valiullin, R. Mass transfer in mesoporous materials: the benefit of microscopic diffusion measurement. *Chem. Soc. Rev.* **2013**, *42*, 4172-4197.

(17) Higgins, D. A.; Tran-Ba, K.-H.; Ito, T. Following Single Molecules to a Better Understanding of Self-Assembled One-Dimensional Nanostructures. *J. Phys. Chem. Lett.* **2013**, *4*, 3095-3103.

(18) Higgins, D. A.; Park, S. C.; Tran-Ba, K.-H.; Ito, T. Single-Molecule Investigations of Morphology and Mass-Transport Dynamics in Nanostructured Materials. *Annu. Rev. Anal. Chem.* **2015**.

(19) Schmidt, T.; Schutz, G. J.; Baumgartner, W.; Gruber, H. J.; Schindler, H. Imaging of single molecule diffusion. *Proc. Natl. Acad. Sci.* **1996**, *93*, 2926-2929.

(20) Kirstein, J.; Platschek, B.; Jung, C.; Brown, R.; Bein, T.; Brauchle, C. Exploration of nanostructured channel systems with single-molecule probes. *Nat. Mater.* **2007**, *6*, 303-310.

(21) Darling, S. B. Directing the Self-Assembly of Block Copolymers. *Prog. Polym. Sci.* **2007**, *32*, 1152-1204.

(22) Tran Ba, K. H.; Everett, T. A.; Ito, T.; Higgins, D. A. Trajectory Angle Determination in One Dimensional Single Molecule Tracking Data by Orthogonal Regression Analysis. *Phys. Chem. Chem. Phys.* **2011**, *13*, 1827-1835.

(23) Tran-Ba, K.-H.; Finley, J. J.; Higgins, D. A.; Ito, T. Single-Molecule Tracking Studies of Millimeter-Scale Cylindrical Domain Alignment in Polystyrene-Poly(ethylene oxide) Diblock Copolymer Films Induced by Solvent Vapor Penetration. *J. Phys. Chem. Lett.* **2012**, *3*, 1968-1973.

(24) Tran-Ba, K.-H.; Higgins, D. A.; Ito, T. Single-Molecule Tracking Studies of Flow-Induced Microdomain Alignment in Cylinder-Forming Polystyrene-Poly(ethylene oxide) Diblock Copolymer Films. *J. Phys. Chem. B* **2014**, 11406.

(25) Osuji, C. O. Alignment of Self-Assembled Structures in Block Copolymer Films by Solvent Vapor Permeation. *Macromolecules* **2010**, *43*, 3132-3135.

(26) Albalak, R. J.; Thomas, E. L. Microphase Separation of Block Copolymer Solutions in a Flow Field. *J. Polym. Sci. Pol. Phys.* **1993**, *31*, 37-46.

(27) Xia, Y. N.; Yang, P. D.; Sun, Y. G.; Wu, Y. Y.; Mayers, B.; Gates, B.; Yin, Y. D.; Kim, F.; Yan, Y. Q. One-dimensional nanostructures: Synthesis, characterization, and applications. *Adv. Mater.* **2003**, *15*, 353-389.

(28) Gates, B. D.; Xu, Q. B.; Stewart, M.; Ryan, D.; Willson, C. G.; Whitesides, G. M. New approaches to nanofabrication: Molding, printing, and other techniques. *Chem. Rev.* **2005**, *105*, 1171-1196.

(29) Kuchibhatla, S.; Karakoti, A. S.; Bera, D.; Seal, S. One dimensional nanostructured materials. *Prog. Mater. Sci.* **2007**, *52*, 699-913.

(30) Baker, L. A.; Jin, P.; Martin, C. R. Biomaterials and biotechnologies based on nanotube membranes. *Crit. Rev. Solid State Mater. Sci.* **2005**, *30*, 183-205.

(31) Warkiani, M. E.; Bhagat, A. A. S.; Khoo, B. L.; Han, J.; Lim, C. T.; Gong, H. Q.; Fane, A. G. Isoporous Micro/Nanoengineered Membranes. *ACS Nano* **2013**, *7*, 1882-1904.

(32) Brinker, C. J.; Lu, Y. F.; Sellinger, A.; Fan, H. Y. Evaporation-induced self-assembly: Nanostructures made easy. *Adv. Mater.* **1999**, *11*, 579-592.

(33) Hamley, I. W. Nanotechnology with soft materials. *Angew. Chem.-Int. Ed.* **2003**, *42*, 1692-1712.

(34) Lodge, T. P. Block copolymers: Past successes and future challenges. *Macromol. Chem. Phys.* **2003**, *204*, 265-273.

(35) Whitesides, G. M.; Mathias, J. P.; Seto, C. T. Molecular Self-Assembly and Nanochemistry - A Chemical Strategy for the Synthesis of Nanostructures. *Science* **1991**, *254*, 1312-1319.

(36) Ulman, A. Formation and structure of self-assembled monolayers. *Chem. Rev.* **1996**, *96*, 1533-1554.

(37) Fasolka, M. J.; Mayes, A. M. Block copolymer thin films: Physics and applications. *Ann. Rev. Mater. Res.* **2001**, *31*, 323-355.

(38) Davis, M. E. Ordered porous materials for emerging applications. *Nature* **2002**, *417*, 813-821.

(39) Corma, A. From microporous to mesoporous molecular sieve materials and their use in catalysis. *Chem. Rev.* **1997**, *97*, 2373-2419.

(40) Lu, Y. F.; Ganguli, R.; Drewien, C. A.; Anderson, M. T.; Brinker, C. J.; Gong, W. L.; Guo, Y. X.; Soyez, H.; Dunn, B.; Huang, M. H.; Zink, J. I. Continuous formation of supported cubic and hexagonal mesoporous films by sol gel dip-coating. *Nature* **1997**, *389*, 364-368.

(41) Hench, L. L.; West, J. K. The Sol-Gel Process. *Chem. Rev.* **1990**, *90*, 33-72.

(42) Ogawa, M. Formation of Novel Oriented Transparent Films of Layered Silica-Surfactant Nanocomposites. *J. Am. Chem. Soc.* **1994**, *116*, 7941-7942.

(43) Hench, L. L.; West, J. K. The Solg-Gel Process. *Chem. Rev.* **1990**, *90*, 33-72.

(44) Ye, F.; Collinson, M. M.; Higgins, D. A. What can be learned from single molecule spectroscopy? Applications to sol-gel-derived silica materials. *Phys. Chem. Chem. Phys.* **2009**, *11*, 66-82.

(45) Kandimalla, V. B.; Tripathi, V. S.; Ju, H. X. Immobilization of biomolecules in sol-gels: Biological and analytical applications. *Crit. Rev. Anal. Chem.* **2006**, *36*, 73-106.

(46) Huo, Q. S.; Feng, J. L.; Schuth, F.; Stucky, G. D. Preparation of hard mesoporous silica spheres. *Chem. Mater.* **1997**, *9*, 14-&.

(47) Wirnsberger, G.; Scott, B. J.; Stucky, G. D. pH Sensing with mesoporous thin films. *Chem. Comm.* **2001**, 119-120.

(48) Scott, B. J.; Wirnsberger, G.; Stucky, G. D. Mesoporous and mesostructured materials for optical applications. *Chem. Mater.* **2001**, *13*, 3140-3150.

(49) Wirth, M. J.; Swinton, D. J. Single-molecule probing of mixed-mode adsorption at a chromatographic interface. *Anal. Chem.* **1998**, *70*, 5264-5271.

(50) Wirth, M. J.; Legg, M. A.: Single-molecule probing of adsorption and diffusion on silica surfaces. In *Annual Review of Physical Chemistry*; Annual Review of Physical Chemistry; Annual Reviews: Palo Alto, 2007; Vol. 58; pp 489-510.

(51) Tolbert, S. H.; Firouzi, A.; Stucky, G. D.; Chmelka, B. F. Magnetic field alignment of ordered silicate-surfactant composites and mesoporous silica. *Science* **1997**, *278*, 264-268.

(52) Walcarius, A.; Sibottier, E.; Etienne, M.; Ghanbaja, J. Electrochemically assisted self-assembly of mesoporous silica thin films. *Nature Mater.* **2007**, *6*, 602-608.

(53) Miyata, H.; Kuroda, K. Preferred alignment of mesochannels in a mesoporous silica film grown on a silicon (110) surface. *J. Am. Chem. Soc.* **1999**, *121*, 7618-7624.

(54) Wu, C. W.; Ohsuna, T.; Edura, T.; Kuroda, K. Orientational control of hexagonally packed silica mesochannels in lithographically designed confined nanospaces. *Angew. Chem.-Int. Ed.* **2007**, *46*, 5364-5368.

(55) Park, S. C.; Ito, T.; Higgins, D. A. Single Molecule Tracking Studies of Flow-Aligned Mesoporous Silica Monoliths: Aging-Time Dependence of Pore Order. *J. Phys. Chem. B* **2013**, *117*, 4222-4230.

(56) Ruhle, B.; Davies, M.; Lebold, T.; Brauchle, C.; Bein, T. Highly Oriented Mesoporous Silica Channels Synthesized in Microgrooves and Visualized with Single-Molecule Diffusion. *ACS Nano* **2012**, *6*, 1948-1960.

(57) Trau, M.; Yao, N.; Kim, E.; Xia, Y. N.; Whitesides, G. M.; Aksay, I. A. Microscopic Patterning of Orientated Mesoscopic Silica through Guided Growth. *Nature* **1997**, *390*, 674-676.

(58) Melosh, N. A.; Davidson, P.; Feng, P.; Pine, D. J.; Chmelka, B. F. Macroscopic shear alignment of bulk transparent mesostructured silica. *J. Am. Chem. Soc.* **2001**, *123*, 1240-1241.

(59) Yamaguchi, A.; Kaneda, H.; Fu, W. S.; Teramae, N. Structural control of surfactant-templated mesoporous silica formed inside columnar alumina pores. *Adv. Mater.* **2008**, *20*, 1034-+.

(60) Hamley, I. W.: *The Physics of Block Copolymers*; Oxford University Press: Oxford, **1998**. pp. 432.

(61) Bates, F. S.; Fredrickson, G. H. Block Copolymer Thermodynamics - Theory and Experiment. *Ann. Rev. Phys. Chem.* **1990**, *41*, 525-557.

(62) Fredrickson, G. H.; Bates, F. S. Dynamics of block copolymers: Theory and experiment. *Ann. Rev. Mater. Sci.* **1996**, *26*, 501-550.

(63) Szwarc, M.; Levy, M.; Milkovich, R. Polymerization Initiated by Electron Transfer to Monomer - A New Method of Formation of Block Polymers. *J. Am. Chem. Soc.* **1956**, *78*, 2656-2657.

(64) Hamley, I.: Introduction to Block Copolymers. In *Developments in Block Copolymer Science and Technology*; Hamley, I., Ed.; Wiley: West Sussex, 2004; pp 1 - 29.

(65) Hillmyer, M. A. Nanoporous Materials from Block Copolymer Precursors. *Adv. Polym. Sci.* **2005**, *190*, 137-181.

(66) Sinturel, C.; Vayer, M.; Morris, M.; Hillmyer, M. A. Solvent Vapor Annealing of Block Polymer Thin Films. *Macromolecules* **2013**, *46*, 5399-5415.

(67) Bang, J.; Jeong, U.; Ryu, D. Y.; Russell, T. P.; Hawker, C. J. Block Copolymer Nanolithography: Translation of Molecular Level Control to Nanoscale Patterns. *Adv. Mater.* **2009**, *21*, 4769-4792.

(68) Thurn-Albrecht, T.; Schotter, J.; Kastle, C. A.; Emley, N.; Shibauchi, T.; Krusin-Elbaum, L.; Guarini, K.; Black, C. T.; Tuominen, M. T.; Russell, T. P. Ultrahigh-density nanowire arrays grown in self-assembled diblock copolymer templates. *Science* **2000**, *290*, 2126-2129.

(69) Park, M.; Harrison, C.; Chaikin, P. M.; Register, R. A.; Adamson, D. H. Block copolymer lithography: Periodic arrays of similar to 10(11) holes in 1 square centimeter. *Science* **1997**, *276*, 1401-1404.

(70) Park, S.; Lee, D. H.; Xu, J.; Kim, B.; Hong, S. W.; Jeong, U.; Xu, T.; Russell, T. P. Macroscopic 10-Terabit-per-Square- Inch Arrays from Block Copolymers with Lateral Order. *Science* **2009**, *323*, 1030-1033.

(71) Hallinan Jr., D. T.; Balsara, N. P. Polymer Electrolytes. *Annu. Rev. Mater. Res.* **2013**, *43*, 503 -525.

(72) Young, W.-S.; Kuan, W.-F.; Epps III, T. H. Block Copolymer Electrolytes for Rechargeable Lithium Batteries. *J. Polym. Sci., Part B Pol. Phys.* **2014**, *52*, 1-16.

(73) Pandey, B.; Tran-Ba, K.-H.; Li, Y. X.; Diaz, R.; Ito, T. Electrochemical study of the diffusion of cytochrome c within nanoscale pores derived from cylinder-forming polystyrene-poly(methylmethacrylate) diblock copolymers. *Electrochim. Acta* **2011**, *56*, 10185-10190.

(74) Li, Y.; Ito, T. Size-Exclusion Properties of Nanoporous Films Derived from Polystyrene-Poly(methylmethacrylate) Diblock Copolymers Assessed Using Direct Electrochemistry of Ferritin. *Anal. Chem.* **2009**, *81*, 851-855.

(75) Yang, S. Y.; Ryu, I.; Kim, H. Y.; Kim, J. K.; Jang, S. K.; Russell, T. P. Nanoporous membranes with ultrahigh selectivity and flux for the filtration of viruses. *Adv. Mater.* **2006**, *18*, 709-715.

(76) Mao, H.; Hillmyer, M. A. Nanoporous Polystyrene by Chemical Etching of Poly(ethylene oxide) from Ordered Block Copolymers. *Macromolecules* **2005**, *38*, 4038-4039.

(77) Ryu, J. H.; Park, S.; Kim, B.; Klaikherd, A.; Russell, T. P.; Thayumanavan, S. Highly Ordered Gold Nanotubes Using Thiols at a Cleavable Block Copolymer Interface. *J. Am. Chem. Soc.* **2009**, *131*, 9870 - 9871.

(78) Xu, J.; Hong, S. W.; Gu, W. Y.; Lee, K. Y.; Kuo, D. S.; Xiao, S. G.; Russell, T. P. Fabrication of Silicon Oxide Nanodots with an Areal Density Beyond 1 Teradots Inch-2. *Adv. Mater.* **2011**, *23*, 5755-5761.

(79) Hirota, K.; Tajima, K.; Hashimoto, K. Facile preparation of nanoelectrode ensembles using amphiphilic block copolymer film. *Langmuir* **2005**, *21*, 11592-11595.

(80) http://polymersource.com/dataSheet/P4390-SEO.pdf.

(81) Olson, D. A.; Chen, L.; Hillmyer, M. A. Templating Nanoporous Polymers with Ordered Block Copolymers. *Chem. Mater.* **2008**, *20*, 869-890.

(82) Bang, J.; Jeong, U.; Ryu, D. Y.; Russell, T. P.; Hawker, C. J. Block Copolymer Nanolithography: Translation of Molecular Level Control to Nanoscale Patterns. *Adv. Mater.* **2009**, *21*, 4769-4792.

(83) Lefevre, N.; Daoulas, K. C.; Muller, M.; Gohy, J. F.; Fustin, C. A. Self-Assembly in Thin Films of Mixtures of Block Copolymers and Homopolymers Interacting by Hydrogen Bonds. *Macromolecules* **2010**, *43*, 7734-7743.

(84) Zhang, M.; Yang, L.; Yurt, S.; Misner, M. J.; Chen, J.-T.; Coughlin, E. B.; Venkataraman, D.; Russell, T. P. Highly Ordered Nanoporous Thin Films from Cleavable Polystyrene-block-poly(ethylene oxide). *Adv. Mater.* **2007**, *19*, 1571-1576.

(85) Ryu, J. H.; Park, S.; Kim, B.; Klaikherd, A.; Russell, T. P.; Thayumanavan, S. Highly Ordered Gold Nanotubes Using Thiols at a Cleavable Block Copolymer Interface. *J. Am. Chem. Soc.* **2009**, *131*, 9870-9880.

(86) Thurn-Albrecht, T.; Steiner, R.; DeRouchey, J.; Stafford, C. M.; Huang, E.; Bal, M.; Tuominen, M.; Hawker, C. J.; Russell, T. P. Nanoscopic Templates from Oriented Block Copolymer Films. *Adv. Mater.* **2000**, *12*, 787-791.

(87) Kang, M.; Moon, B. Synthesis of Photocleavable Poly(styrene-block-ethylene oxide) and Its Self-Assembly into Nanoporous Thin Films. *Macromolecules* **2009**, *42*, 455-458.

(88) Zhao, H.; Gu, W. Y.; Sterner, E.; Russell, T. P.; Coughlin, E. B.; Theato, P. Highly Ordered Nanoporous Thin Films from Photocleavable Block Copolymers. *Macromolecules* **2011**, *44*, 6433-6440.

(89) Li, X. F.; Fustin, C. A.; Lefevre, N.; Gohy, J. F.; De Feyter, S.; De Baerdemaeker, J.; Egger, W.; Vankelecom, I. F. J. Ordered nanoporous membranes based on diblock copolymers with high chemical stability and tunable separation properties. *J. Mater. Chem.* **2010**, *20*, 4333-4339.

(90) Karunakaran, M.; Nunes, S. P.; Qiu, X. Y.; Yu, H. Z.; Peinemann, K. V. Isoporous PS-b-PEO ultrafiltration membranes via self-assembly and water-induced phase separation. *J. Membrane Sci.* **2014**, *453*, 471-477.

(91) Hahn, J.; Filiz, V.; Rangou, S.; Clodt, J.; Jung, A.; Buhr, K.; Abetz, C.; Abetz, V. Structure formation of integral-asymmetric membranes of polystyrene-block-Poly(ethylene oxide). *J. Polym. Sci. Pol. Phys.* **2013**, *51*, 281-290.

(92) Sun, Z. C.; Kim, D. H.; Wolkenhauer, M.; Bumbu, G. G.; Knoll, W.; Gutmann, J. S. Synthesis and photoluminescence of titania nanoparticle arrays templated by block-copolymer thin films. *Chemphyschem* **2006**, *7*, 370-378.

(93) Meyer, W. H. Polymer electrolytes for lithium-ion batteries. *Adv. Mater.* **1998**, *10*, 439 -448.

(94) Lazzari, M.; De Rosa, C.: Methods for the Alignment and the Large-Scale Ordering of Block Copolymer Morphologies. In *Block Copolymer in Nanoscience*; Lazzari, M., Liu, G., Lecommandoux, S., Eds.; Wiley-VCH: Weinheim, 2006; pp 191-231.

(95) Wang, H.; Newstein, M. C.; Chang, M. Y.; Balsara, N. P.; Garetz, B. A. Birefringence and Depolarized Light Scattering of an Ordered Block Copolymer Melt under Shear Flow. *Macromolecules* **2000**, *33*, 3719-3730.

(96) Chastek, T. Q.; Lodge, T. P. Grain Shapes and Growth Kinetics during Self-Assembly of Block Copolymers. *J. Polym. Sci., Part B Pol. Phys.* **2006**, *44*, 481-491.

(97) Kim, S. H.; Misner, M. J.; Xu, T.; Kimura, M.; Russell, T. P. Highly Oriented and Ordered Arrays from Block Copolymers via Solvent Evaporation. *Adv. Mater.* **2004**, *16*, 226-231.

(98) Kim, S. H.; Misner, M. J.; Russell, T. P. Solvent-induced ordering in thin film diblock copolymer/homopolymer mixtures. *Adv. Mater.* **2004**, *16*, 2119-2125.

(99) Mokarian-Tabari, P.; Collins, T. W.; Holmes, J. D.; Morris, M. A. Cyclical "Flipping" of Morphology in Block Copolymer Thin Films. *ACS Nano* **2011**, *5*, 4617-4623.

(100) Kim, T. H.; Hwang, J.; Hwang, W. S.; Huh, J.; Kim, H.-C.; Kim, S. H.; Hong, J. M.; Thomas, E. L.; Park, C. Hierarchical ordering of block copolymer nanostructures by solvent annealing combined with controlled dewetting. *Adv. Mater.* **2008**, *20*, 522-530.

(101) Peng, J.; Han, Y.; Knoll, W.; Kim, D. H. Development of Nanodomain and Fractal Morphologies in Solvent Annealed Block Copolymer Thin Films. *Macromol. Rapid Comm.* **2007**, *28*, 1422-1428.

(102) Gu, W. Y.; Hong, S. W.; Russell, T. P. Orienting Block Copolymer Microdomains with Block Copolymer Brushes. *ACS Nano* **2012**, *6*, 10250-10257.

(103) Kim, S. H.; Misner, M. J.; Yang, L.; Gang, O.; Ocko, B. M.; Russell, T. P. Salt complexation in block copolymer thin films. *Macromolecules* **2006**, *39*, 8473-8479.

(104) Sakurai, S. Progress in control of microdomain orientation in block copolymers - Efficiencies of various external fields. *Polymer* **2008**, *49*, 2781-2796.

(105) Osuji, C.; Ferreira, P. J.; Mao, G.; Ober, C. K.; Vander Sande, J. B.; Thomas, E. L. Alignment of Self-Assembled Hierarchical Microstructure in Liquid Crystalline Diblock Copolymers Using High Magnetic Fields. *Macromolecules* **2004**, *37*, 9903-9908.

(106) Morkved, T. L.; Lu, M.; Urbas, A. M.; Ehrichs, E. E.; Jaeger, H. M.; Mansky, P.; Russell, T. P. Local Control of Microdomain Orientation in Diblock Copolymer Thin Films with Electric Fields. *Science* **1996**, *273*, 931-933.

(107) Mansky, P.; Liu, Y.; Huang, E.; Russell, T. P.; Hawker, C. Controlling Polymer-Surface Interactions with Random Copolymer Brushes. *Science* **1997**, *275*, 1458-1460.

(108) Kim, S. O.; Solak, H. H.; Stoykovich, M. P.; Ferrier, N. J.; de Pablo, J. J.; Nealey, P. F. Epitaxial Self-Assembly of Block Copolymers on Lithographically Defined Nanopatterned Substrates. *Nature* **2003**, *424*, 411-414.

(109) Scott, D. B.; Waddon, A. J.; Lin, Y. G.; Karasz, F. E.; Winter, H. H. Shear-Induced Orientation Transitions in Triblock Copolymer Styrene-Butadiene-Styrene with Cylindrical Domain Morphology. *Macromolecules* **1992**, *25*, 4175-4181.

(110) Kim, G.; Libera, M. Morphological Development in Solvent-Cast Polystyrene-Polybutadiene-Polystyrene (SBS) Triblock Copolymer Thin Films. *Macromolecules* **1998**, *31*, 2569-2577.

(111) Fukunaga, K.; Elbs, H.; Magerle, R.; Krausch, G. Large-Scale Alignment of ABC Block Copolymer Microdomains via Solvent Vapor Treatment. *Macromolecules* **2000**, *33*, 947-953.

(112) Bang, J.; Kim, S. H.; Drockenmuller, E.; Misner, M. J.; Russell, T. P.; Hawker, C. J. Defect-Free Nanoporous Thin Films from ABC Triblock Copolymers. *J. Am. Chem. Soc.* **2006**, *128*, 7622-7629.

(113) Bang, J.; Kim, B. J.; Stein, G. E.; Russell, T. P.; Li, X.; Wang, J.; Kramer, E. J.; Hawker, C. J. Effect of Humidity on the Ordering of PEO-Based Copolymer Thin Films. *Macromolecules* **2007**, *40*, 7019-7025.

(114) Albert, J. N. L.; Bogart, T. D.; Lewis, R. L.; Beers, K. L.; Fasolka, M. J.; Hutchison, J. B.; Vogt, B. D.; Epps, T. H., III. . Gradient Solvent Vapor Annealing of Block Copolymer Thin Films Using a Microfluidic Mixing Device. *Nano Lett.* **2011**, *11*, 1351-1357.

(115) Hamley, I. W. Structure and Flow Behaviour of Block Copolymers. *J. Phys.-Condens. Mat.* **2001**, *13*, 643-671.

(116) Colby, R. H. Block Copolymer Dynamics. *Curr. Opin. Colloid In.* **1996**, *1*, 454-465.

(117) Keller, A.; Pedemonte, E.; Willmouth, F. M. Macro-lattice from Segregated Amorphous Phases of a Three Block Copolymer. *Nature* **1970**, *225*, 538-540.

(118) Albalak, R. J.; Thomas, E. L. Microphase Separation of Block Copolymer Solutions in a Flow Field. *J. Polym. Sci., Part B Pol. Phys.* **1993**, *31*, 37-46.

(119) Lodge, T. P.; Pudil, B.; Hanley, K. J. The Full Phase Behavior for Block Copolymers in Solvents of Varying Selectivity. *Macromolecules* **2002**, *35*, 4707-4717.

(120) Huang, Y.; Duan, X.; Wei, Q.; Lieber, C. M. Directed Assembly of One-Dimensional Nanostructures into Functional Networks. *Science* **2001**, *291*, 630-633.

(121) Kirkeminde, A. W.; Torres, T.; Ito, T.; Higgins, D. A. Multiple Diffusion Pathways in Pluronic F127 Mesophases Revealed by Single Molecule Tracking and Fluorescence Correlation Spectroscopy. *J. Phys. Chem. B* **2011**, *115*, 12736-12743.

(122) Xu, H.; Minter, C. J.; Nagasaka, S.; Ito, T.; Higgins, D. A. Elongation, Alignment, and Guided Electrophoretic Migration of ds-DNA in Flow-Aligned Hexagonal F127 Gels. *J. Phys. Chem. B* **2014**, *118*, 4151-4159.

(123) Miyata, H.; Kuroda, K. Preferred alignment of mesochannels in a mesoporous silica film grown on a silicon (110) surface. *J. Am. Chem. Soc.* **1999**, *121*, 7618-7624.

(124) Melosh, N. A.; Davidson, P.; Feng, P.; Pine, D. J.; Chmelka, B. F. Macroscopic shear alignment of bulk transparent mesostructured silica. *J. Am. Chem. Soc.* **2001**, *123*, 1240-1241.

(125) Every, H. A.; van der Ham, L.; Picken, S. J.; Mendes, E. Spontaneous homeotropic alignment in films of rigid-flexible polyelectrolyte complexes. *Soft Matter* **2009**, *5*, 342-345.

(126) Magonov, S. N.; Reneker, D. H. Characterization of polymer surfaces with atomic force microscopy. *Annu. Rev. Mater. Sci.* **1997**, *27*, 175-222.

(127) Ito, T. Scanning Probe Microscopy Using Chemically Modified Tips. University of Tokyo, 1997.

(128) Ito, T.; Grabowska, I.; Ibrahim, S. Chemical-force microscopy for materials characterization. *Trac-Tren Anal. Chem.* **2010**, *29*, 225-233.

(129) Vezie, D. L.; Thomas, E. L.; Adams, W. W. Low-Voltage, High-Resolution Scanning Electron-Microscopy - A New Characterization Technique for Polymer Morphology. *Polymer* **1995**, *36*, 1761-1779.

(130) Goodhew, P. J.; Humphreys, J.; Beanland, R.: *Electron Microscopy and Analysis*; Taylor & Francis: London, UK, 2001.

(131) Oss-Ronen, L.; Schmidt, J.; Abetz, V.; Radulescu, A.; Cohen, Y.; Talmon, Y. Characterization of Block Copolymer Self-Assembly: From Solution to Nanoporous Membranes. *Macromolecules* **2012**, *45*, 9631-9642.

(132) Jirage, K. B.; Hulteen, J. C.; Martin, C. R. Effect of thiol chemisorption on the transport properties of gold nanotubule membranes. *Anal. Chem.* **1999**, *71*, 4913-4918.

(133) Jirage, K. B.; Hulteen, J. C.; Martin, C. R. Nanotubule-based molecular-filtration membranes. *Science* **1997**, *278*, 655-658.

(134) Pople, J. A.; Hamley, I. W.; Terrill, N. J.; Fairclough, J. P. A.; Ryan, A. J.; Yu, G.-E.; Booth, C. Shear-Induced Orientational Order in the Hexagonal Phase of Oxyethylene/Oxybutylene Diblock Copolymer Gels. *Polymer* **1998**, *39*, 4891-4896.

(135) Pople, J. A.; Hamley, I. W.; Fairclough, J. P. A.; Ryan, A. J.; Booth, C. Orientational Ordering of a Poly(oxyethylene)-Poly(oxybutylene) Diblock Copolymer Gel under Steady Shear Flow. *Macromolecules* **1998**, *31*, 2952-2956.

(136) Jain, A.; Hall, L. M.; Garcia, C. B. W.; Gruner, S. M.; Wiesner, U. Flow-Induced Alignment of Block Copolymer-Sol Nanoparticle Coassemblies toward Oriented Bulk Polymer-Silica Hybrids. *Macromolecules* **2005**, *38*, 10095-10100.

(137) Shimizu, K.; Yasuda, T.; Saito, H. Perpendicular Orientation of Cylindrical Microdomains in Extruded Triblock Copolymer. *Macromolecules* **2010**, *43*, 2088-2091.

(138) Moerner, W. E.; Fromm, D. P. Methods of Single-Molecule Fluorescence Spectroscopy and Microscopy. *Rev. Sci. Instrum.* **2003**, *74*, 3597-3619.

(139) Schmidt, T.; Schutz, G. J.; Baumgartner, W.; Gruber, H. J.; Schindler, H. Imaging of single molecule diffusion. *Proc. Natl. Acad. Sci.* **1996**, *93*, 2926-2929.

(140) Thompson, R. E.; Larson, D. R.; Webb, W. W. Precise Nanometer Localization Analysis for Individual Fluorescent Probes. *Biophys. J.* **2002**, *82*, 2775-2783.

(141) Sharonov, A.; Hochstrasser, R. M. Wide-field subdiffraction imaging by accumulated binding of diffusing probes. *Proc. Natl. Acad. Sci.* **2006**, *103*, 18911-18916.

(142) Wu, D.; Liu, Z.; Sun, C.; Zhang, X. Super-Resolution Imaging by Random Adsorbed Molecule Probes. *Nano Lett.* **2008**, *8*, 1159-1162.

(143) Betzig, E.; Patterson, G. H.; Sougrat, R.; Lindwasser, O. W.; Olenych, S.; Bonifacino, J. S.; Davidson, M. W.; Lippincott-Schwartz, J.; Hess, H. F. Imaging Intracellular Fluorescent Proteins at Nanometer Resolution. *Science* **2006**, *313*, 1642-1645.

(144) Rust, M. J.; Bates, M.; Zhuang, X. Sub-diffraction-limit imaging by stochastic optical reconstruction microscopy (STORM). *Nature Methods* **2006**, *3*, 793-796.

(145) Hu, D.; Tian, Z.; Wu, W.; Wan, W.; Li, A. D. Q. Photoswitchable Nanoparticles Enable High-Resolution Cell Imaging: PULSAR Microscopy. *J. Am. Chem. Soc.* **2008**, *130*, 15279-15281.

(146) Axelrod, D.; Koppel, D. E.; Schlessinger, J.; Elson, E.; Webb, W. W. Mobility Measurement By Analysis Of Fluorescence Photobleaching Recovery Kinetics. *Biophys. J.* **1976**, 1055.

(147) Zuerner, A.; Kirstein, J.; Doblinger, M.; Braeuchle, C.; Bein, T. Visualizing single-molecule diffusion in mesoporous materials. *Nature* **2007**, *450*, 705-709.

(148) Kirstein, J.; Platschek, B.; Jung, C.; Brown, R.; Bein, T.; Braeuchle, C. Exploration of nanostructured channel systems with single molecule probes. *Nature Mater.* **2007**, *6*, 303-310.

(149) Jung, C.; Kirstein, J.; Platschek, B.; Bein, T.; Budde, M.; Frank, I.; Muellen, K.; Michaelis, J.; Braeuchle, C. Diffusion of Oriented Single Molecules with Switchable Mobility in Networks of Long Unidimensional Nanochannels. *J. Am. Chem. Soc.* **2008**, *130*, 1638-1648.

(150) Ito, S.; Fukuya, S.; Kusumi, T.; Ishibashi, Y.; Miyasaka, H.; Goto, Y.; Ikai, M.; Tani, T.; Inagaki, S. Microscopic Structure and Mobility of Guest Molecules in Mesoporous Hybrid

Organosilica: Evaluation with Single-Molecule Tracking. *J. Phys. Chem. C* **2009**, *113*, 11884-11891.

(151) Hou, Y.; Higgins, D. A. Single Molecule Studies of Dynamics in Polymer Thin Films and at Surfaces: Effect of Ambient Relative Humidity. *J. Phys. Chem. B* **2002**, *106*, 10306-10315.

(152) Honciuc, A.; Harant, A. W.; Schwartz, D. K. Single-Molecule Observations of Surfactant Diffusion at the Solution-Solid Interface. *Langmuir* **2008**, *24*, 6562-6566.

(153) Dickson, R. M.; Norris, D. J.; Tzeng, Y.-L.; Moerner, W. E. Three-Dimensional Imaging of Single Molecules Solvated in Pores of Poly(acrylamide) Gels. *Science* **1996**, *274*, 966-969.

(154) Sonnleitner, A.; Schutz, G. J.; Schmidt, T. Free Brownian Motion of Individual Lipid Molecules in Biomembranes. *Biophys. J.* **1999**, *77*, 2638-2642.

(155) Ke, P. C.; Naumann, C. A. Single Molecule Fluorescence Imaging of Phospholipid Monolayers at the Air-Water Interface. *Langmuir* **2001**, *17*, 3727-3733.

(156) Ke, P. C.; Naumann, C. A. Hindered Diffusion in Polymer-Tethered Phospholipid Monolayers at the Air-Water Interface: A Single Molecule Fluorescence Imaging Study. *Langmuir* **2001**, *17*, 5076-5081.

(157) McCain, K. S.; Hanley, D. C.; Harris, J. M. Single-Molecule Fluorescence Trajectories for Investigating Molecular Transport in Thin Silica Sol-Gel Films. *Anal. Chem.* **2003**, *75*, 4351-4359.

(158) Harms, G. S.; Cognet, L.; Lommerse, P. H. M.; Blab, G. A.; Schmidt, T. Autofluorescent Proteins in Single-Molecule Research: Applications to Live Cell Imaging Microscopy. *Biophys. J.* **2001**, *80*, 2396-2408.

(159) Vrljic, M.; Nishimura, S. Y.; Brasselet, S.; Moerner, W. E.; McConnell, H. M. Translational Diffusion of Individual Class II MHC Membrane Proteins in Cells. *Biophys. J.* **2002**, *83*, 2681-2692.

(160) Nishimura, S. Y.; Lord, S. J.; Klein, L. O.; Willets, K. A.; He, M.; Lu, Z.; Tweig, R. J.; Moerner, W. E. Diffusion of Lipid-Like Single-Molecule Fluorophores in the Cell Membrane. *J. Phys. Chem. B* **2006**, *110*, 8151-8157.

(161) Honciuc, A.; Howard, A. L.; Schwartz, D. K. Single Molecule Observations of Fatty Acid Adsorption at the Silica/Water Interface: Activation Energy of Attachment. *J. Phys. Chem. C* **2009**, *113*, 2078-2081.

(162) Zuerner, A.; Kirstein, J.; Doeblinger, M.; Braeuchle, C.; Bein, T. Visualizing single-molecule diffusion in mesoporous materials. *Nature* **2007**, *450*, 705-709.

(163) Werley, C. A.; Moerner, W. E. Single-molecule nanoprobes explore defects in spin-grown crystals. *J. Phys. Chem. B* **2006**, *110*, 18939-18944.

(164) Jung, C.; Schwaderer, P.; Dethlefsen, M.; Koehn, R.; Michaelis, J.; Braeuchle, C. Visualization of the self-assembly of silica nanochannels reveals growth mechanism. *Nature Nanotech.* **2011**, *6*, 86-91.

(165) Yorulmaz, M.; Kiraz, A.; Demirel, A. L. Motion of Single Terrylene Molecules in Confined Channels of Poly(butadiene)-Poly(ethylene oxide) Diblock Copolymer. *J. Phys. Chem. B* **2009**, *113*, 9640-9643.

(166) Trau, M.; Yao, N.; Kim, E.; Xia, Y.; Whitesides, G. M.; Aksay, I. A. Microscopic patterning of oriented mesoscopic silica through guided growth. *Nature* **1997**, *390*, 674-676.

(167) Tolbert, S. H.; Firouzi, A.; Stucky, G. D.; Chmelka, B. F. Magnetic Field Alignment of Ordered Silicate-Surfactant Composites and Mesoporous Silica. *Science* **1997**, *278*, 264-268.

(168) Miyata, H.; Noma, T.; Watanabe, M.; Kuroda, K. Preparation of Mesoporous Silica Films with Fully Aligned Large Mesochannels Using Nonionic Surfactants. *Chem. Mater.* **2002**, *14*, 766-772.

(169) Fukumoto, H.; Nagano, S.; Kawatsuki, N.; Seki, T. Photo-Alignment Behavior of Mesoporous Silica Thin Films Synthesized on a Photo-Cross-Linkable Polymer Film. *Chem. Mater.* **2006**, *18*, 1226-1234.

(170) Miyata, H. Epitaxial growth of a surfactant-silica mesostructure on oriented polyimide films. *Micropor. Mesopor. Mater.* **2007**, *101*, 296-302.

(171) Kisley, L.; F., L. C. Molecular Approaches to Chromatography Using Single Molecule Spectroscopy. *Anal. Chem.* **2015**, 83.

(172) Axelrod, D. Total internal reflection fluorescence microscopy in cell biology. *Traffic* **2001**, *2*, 764-774.

(173) Lord, S. J.; Lee, H. L. D.; Moerner, W. E. Single-Molecule Spectroscopy and Imaging of Biomolecules in Living Cells. *Anal. Chem.* **2010**, *82*, 2192-2203.

(174) Stender, A. S.; Marchuk, K.; Liu, C.; Sander, S.; Meyer, M. W.; Smith, E. A.; Neupane, B.; Wang, G. F.; Li, J. J.; Cheng, J. X.; Huang, B.; Fang, N. Single Cell Optical Imaging and Spectroscopy. *Chem. Rev.* **2013**, *113*, 2469-2527.

(175) Yildiz, A.; Selvin, P. R. Fluorescence imaging with one manometer accuracy: Application to molecular motors. *Acc. Chem. Res.* **2005**, *38*, 574-582.

(176) Lee, C. H.; Crosby, A. J.; Emrick, T.; Hayward, R. C. Characterization of Heterogeneous Polyacrylamide Hydrogels by Tracking of Single Quantum Dots. *Macromolecules* **2014**, *47*, 741-749.

(177) Ito, S.; Fukuya, S.; Kusumi, T.; Ishibashi, Y.; Miyasaka, H.; Goto, Y.; Ikai, M.; Tani, T.; Inagaki, S. Microscopic Structure and Mobility of Guest Molecules in Mesoporous Hybrid Organosilica: Evaluation with Single-Molecule Tracking. *J. Phys. Chem. C* **2009**, *113*, 11884-11891.

(178) Yan, Y.; Krishnakumar, S.; Yu, H.; Ramishetti, S.; Deng, L. W.; Wang, S. H.; Huang, L.; Huang, D. J. Nickel(II) Dithiocarbamate Complexes Containing Sulforhodamine B as Fluorescent Probes for Selective Detection of Nitrogen Dioxide. *J. Am. Chem. Soc.* **2013**, *135*, 5312-5315.

(179) Davies, M.; Ruhle, B.; Li, C.; Mullen, K.; Bein, T.; Brauchle, C. Insights into Nanoscale Electrophoresis of Single Dye Molecules in Highly Oriented Mesoporous Silica Channels. *J. Phys. Chem. C* **2014**, *118*, 24013-24024.

(180) Pramanik, R.; Ito, T.; Higgins, D. A. Molecular Length Dependence of Single Molecule Wobbling within Surfactant- and Solvent-Filled Silica Mesopores. *J. Phys. Chem. C* **2013**, *117*, 15438-15446.

(181) Hellriegel, C.; Kirstein, J.; Brauchle, C. Tracking of single molecules as a powerful method to characterize diffusivity of organic species in mesoporous materials. *New J. Phys.* **2005**, *7*.

(182) Feil, F.; Brauchle, C. Diffusional and orientational dynamics of various single terylene diimide conjugates in mesoporous materials. *Micropor. Mesopor. Mater.* **2009**, *125*, 70 - 78.

(183) Ratner, M. A.; Shriver, D. F. Ion-Transport in Solvent-Free Polymers. *Chem. Rev.* **1988**, *88*, 109-124.

(184) Sbalzarini, I. F.; Koumoutsakos, P. Feature point tracking and trajectory analysis for video imaging in cell biology. *J. Struct. Biol.* **2005**, *151*, 182-195.

(185) Serge, A.; Bertaux, N.; Rigneault, H.; Marguet, D. Dynamic multiple-target tracking to probe spatiotemporal cartography of cell membranes. *Nature Methods* **2008**, *5*, 687-694.

(186) Claytor, K.; Khatua, S.; Guerrero, J. M.; Tcherniak, A.; Tour, J. M.; Link, S. Accurately determining single molecule trajectories of molecular motion on surfaces. *J. Chem. Phys.* **2009**, *130*, 164710.

(187) Bobroff, N. Position measurement with a resolution and noise-limited instrument. *Rev. Sci. Instrum.* **1986**, *57*, 1152-1157.

(188) Particle Tracker. http://rsb.info.nih.gov/ij/.

(189) Seebacher, C.; Hellriegel, C.; Deeg, F.-W.; Braeuchle, C.; Altmaier, S.; Behrens, P.; Muellen, K. Observation of Translational Diffusion of Single Terrylenediimide Molecules in a Mesostructured Molecular Sieve. *J. Phys. Chem. B* **2002**, *106*, 5591-5595.

(190) Hellriegel, C.; Kirstein, J.; Braeuchle, C.; Latour, V.; Pigot, T.; Olivier, R.; Lacombe, S.; Brown, R.; Guieu, V.; Payrastre, C.; Izquierdo, A.; Mocho, P. Diffusion of Single Streptocyanine Molecules in the Nanoporous Network of Sol-Gel Glasses. *J. Phys. Chem. B* **2004**, *108*, 14699-14709.

(191) Chetverikov, D.; Verestoy, J. Feature Point Tracking for Incomplete Trajectories. *Computing* **1999**, *62*, 321-338.

(192) Qian, H.; Sheetz, M. P.; Elson, E. L. Single Particle Tracking - Analysis of Diffuaion and Flow in Two-Dimensional Systems. *Biophys. J.* **1991**, 910.

(193) Lebold, T.; Muehlstein, L. A.; Blechinger, J.; Riederer, M.; Amenitsch, H.; Koehn, R.; Peneva, K.; Muellen, K.; Michaelis, J.; Braeuchle, C.; Bein, T. Tuning Single-Molecule Dynamics in Functionalized Mesoporous Silica. *Chem.-Euro J.* **2009**, *15*, 1661-1672.

(194) Guo, L.; Chowdhury, P.; Fang, J. Y.; Gai, F. Heterogeneous and Anomalous Diffusion Inside Lipid Tubules. *J. Phys. Chem. B* **2007**, 14244.

(195) Okamoto, K.; Shook, C. J.; Bivona, L.; Lee, S. B.; English, D. S. Direct Observation of Wetting and Diffusion in the Hydrophobic Interior of Silica Nanotubes. *Nano Lett.* **2004**, *4*, 233-239.

(196) Artyukhin, A. B.; Shestakov, A.; Harper, J.; Bakajin, O.; Stroeve, P.; Noy, A. Functional one-dimensional lipid bilayers on carbon nanotube templates. *J. Am. Chem. Soc.* **2005**, *127*, 7538-7542.

(197) Sprague, B. L.; McNally, J. G. FRAP Analysis of Binding: Proper and Fitting. *Trends Cell Biol.* **2005**, *15*, 84 - 91.

(198) Deschout, H.; Raemdonck, K.; Demeester, J.; De Smedt, S. C.; Braeckmans, K. FRAP in Pharmaceutical Research: Practical Guidelines and Applications in Drug Delivery. *Pharm. Res.* **2014**, *31*, 255-270.

(199) Carrero, G.; McDonald, D.; Crawford, E.; de Vries, G.; Hendzel, M. J. Using FRAP and mathematical modeling to determine the in vivo kinetics of nuclear proteins. *Methods* **2003**, *29*, 14-28.

(200) Adcock, R. J. A Problem in Least Squares. *The Analyst* **1878**, *5*, 53-54.

(201) Deming, W. E.: *Statistical Adjustment of Data*; Wiley: New York, 1943.

(202) Hood, K.; Nix, B. A. J.; Iles, T. C. Asymptotic Information and Variance-Covariance Matrices for the Linear Structural Model. *The Statistician* **1999**, *48*, 477-493.

(203) Dunn, G.: *Statistical Evaluation of Measurement Errors: Design and Analysis of Reliability Studies*; Arnold: London, 2004.

(204) Beck, J. S.; Vartuli, J. C.; Roth, W. J.; Leonowicz, M. E.; Kresge, C. T.; Schmitt, K. D.; Chu, C. T.-W.; Olson, D. H.; Sheppard, E. W.; McCullen, S. B.; Higgins, J. B.; Schlenker, J. L. A New Family of Mesoporous Molecular Sieves Prepared with Liquid Crystal Templates. *J. Am. Chem. Soc.* **1992**, *114*, 10834-10843.

(205) Kresge, C. T.; Leonowicz, M. E.; Roth, W. J.; Vartuli, J. C.; Beck, J. S. Ordered Mesoporous Molecular Sieves Synthesized by a Liquid-Crystal Template Mechanism. *Nature* **1992**, *359*, 710-712.

(206) Klotz, M.; Albouy, P.-A.; Ayral, A.; Menager, C.; Grosso, D.; Van der Lee, A.; Cabuil, V.; Babonneau, F.; Guizard, C. The True Structure of Hexagonal Mesophase-Templated Silica Films As Revealed by X-ray Scattering: Effects of Thermal Treatments and of Nanoparticle Seeding. *Chem. Mater.* **2000**, *12*, 1721-1728.

(207) Alberius, P. C. A.; Frindell, K. L.; Hayward, R. C.; Kramer, E. J.; Stucky, G. D.; Chmelka, B. F. General Predictive Syntheses of Cubic, Hexagonal, and Lamellar Silica and Titania Mesostructured Thin Films. *Chem. Mater.* **2002**, *14*, 3284-3294.

(208) Yildiz, A.; Forkey, J. N.; McKinney, S. A.; Ha, T.; Goldman, Y. E.; Selvin, P. R. Myosin V Walks Hand-Over-Hand: Single Fluorophore Imaging with 1.5 nm Localization. *Science* **2003**, *300*, 2061-2065.

(209) Yildiz, A.; Tomishige, M.; Vale, R. D.; Selvin, P. R. Kinesin Walks Hand-Over-Hand. *Science* **2004**, *303*, 676-678.

(210) Chang, T.; Rozkiewicz, D. I.; Ravoo, B. J.; Meijer, E. W.; Reinhoudy, D. N. Directional Movement of Dendritic Macromolecules on Gradient Surfaces. *Nano Lett.* **2007**, *7*, 978-980.

(211) Smith, J. T.; Tomfohr, J. K.; Wells, M. C.; Beebe, T. P.; Kepler, T. B.; Reichert, W. M. Measurement of Cell Migration on Surface-Bound Fibronectin Gradients. *Langmuir* **2004**, *20*, 8279-8286.

(212) Solon, J.; Streicher, P.; Richter, R.; Brochard-Wyart, F.; Bassereau, P. Vesicles surfing on a lipid bilayer: Self-induced haptotactic motion. *Proc. Natl. Acad. Sci. USA* **2006**, *103*, 12382-12387.

(213) Saxton, M. J.; Jacobson, K. Single-Particle Tracking: Applications to Membrane Dynamics. *Annu. Rev. Biophys. Biomol. Struct.* **1997**, *26*, 373-399.

(214) Fu, Y.; Ye, F.; Sanders, W. G.; Collinson, M. M.; Higgins, D. A. Single Molecule Spectroscopy Studies of Diffusion in Mesoporous Silica Thin Films. *J. Phys. Chem. B* **2006**, *110*, 9164-9170.

(215) Ye, F.; Higgins, D. A.; Collinson, M. M. Probing Chemical Interactions at the Single Molecule Level in Mesoporous Silica Thin Films. *J. Phys. Chem. C* **2007**, *111*, 6772-6780.

(216) Everett, T. A.; Twite, A. A.; Xie, A.; Battina, S. K.; Hua, D. H.; Higgins, D. A. Preparation and Characterization of Nanofibrous Perylene-Diimide-Polyelectrolyte Composite Thin Films. *Chem. Mater.* **2006**, *18*, 5937-5943.

(217) Lange, J. J.; Culbertson, C. T.; Higgins, D. A. Single Molecule Studies of Solvent-Dependent Diffusion and Entrapment in Poly(dimethylsiloxane) Thin Films. *Anal. Chem.* **2008**, *80*, 9726-9734.

(218) Misawa, K.; Ono, H.; Minoshima, K.; Kobayashi, T. New Fabrication Method for Highly Oriented J Aggregates Dispersed in Polymer Films. *Appl. Phys. Lett.* **1993**, *63*, 577-579.

(219) de Gennes, P. G.; Prost, J.: *The Physics of Liquid Crystals*; Oxford University Press: New York, 1995.

(220) Kazmaier, P. M.; Hoffmann, R. A Theoretical Study of Crystallochromy. Quantum Interference Effects in the Spectra of Perylene Pigments. *J. Am. Chem. Soc.* **1994**, *116*, 9684-9691.

(221) Adachi, M.; Murata, Y.; Nakamura, S. Spectral Similarity and Difference of Naphthalenetetracarboxylic Dianhydride, Perylenetetracarboxylic Dianhydride and Their Derivatives. *J. Phys. Chem.* **1995**, *99*, 14240-14246.

(222) Hellriegel, C.; Kirstein, J.; Braeuchle, C. Tracking of single molecules as a powerful method to characterize diffusivity of organic species in mesoporous materials. *New J. Phys.* **2005**, *7*, 1-14.

(223) Brinker, C. J.; Lu, Y.; Sellinger, A.; H., F. Evaporation-Induced Self-Assembly: Nanostructures Made Easy. *Adv. Mater.* **1999**, *11*, 579-585.

(224) Whitesides, G. M.; Stroock, A. D. Flexible Methods for Microfluidics. *Phys. Today* **2001**, *54*, 42-48.

(225) Chintapalli, M.; Chen, X. C.; Thelen, J. L.; Teran, A. A.; Wang, X.; Garetz, B. A.; Balsara, N. P. Effect of Grain Size on the Ionic Conductivity of a Block Copolymer Electrolyte. *Macromolecules* **2014**, *47*, 5424-5431.

(226) Nikoubashman, A.; Register, R. A.; Panagiotopoulos, A. Z. Simulations of Shear-Induced Morphological Transitions in Block Copolymers. *Soft Matter* **2013**, *9*, 9960-9971.

(227) Hu, H. Q.; Gopinadhan, M.; Osuji, C. O. Directed self-assembly of block copolymers: a tutorial review of strategies for enabling nanotechnology with soft matter. *Soft Matter* **2014**, *10*, 3867-3889.

(228) Ratner, M. A.; Shriver, D. F. Ion Transport in Solvent-Free Polymers. *Chem. Rev.* **1988**, *88*, 109-124.

(229) Flier, B. M. I.; Baier, M. C.; Huber, J.; Mullen, K.; Mecking, S.; Zumbusch, A.; Woll, D. Heterogeneous Diffusion in Thin Polymer Films As Observed by High-Temperature Single-Molecule Fluorescence Microscopy. *J. Am. Chem. Soc.* **2012**, *134*, 480-488.

(230) Brandrup, J.; Immergut, E. H.; Grulke, E. A.; Abe, A.; Bloch, D. R.: *Polymer Handbook, 4th Ed.*; John Wiley & Sons: New York, 2005.

(231) Jain, A.; Hall, L. M.; Garcia, C. B. W.; Gruner, S., M.; Wiesner, U. Flow-Induced Alignment of Block Copolymer-Sol Nanoparticle Coassemblies toward Oriented Bulk Polymer-Silica Hybrids. *Macromolecules* **2005**, *38*, 10095-10100.

(232) Anthony, S.; Granick, S. Image Analysis with Rapid and Accurate Two-Dimensional Gaussian Fitting. *Langmuir* **2009**, *25*, 8152-8160.

(233) Carrero, G.; McDonald, D.; Crawford, E.; de Vries, G.; Hendzel, M. Using FRAP and mathematical modeling to determine the in vivo kinetics of nuclear proteins. *Methods* **2003**, *29*, 14-28.

(234) Guo, L.; Har, J.; Sankaran, J.; Hong, Y.; Kannan, B.; Wohland, T. Molecular diffusion measurement in lipid Bilayers over wide concentration ranges: A comparative study. *Chemphyschem* **2008**, *9*, 721-728.

(235) Feder, T. J.; BrustMascher, I.; Slattery, J. P.; Baird, B.; Webb, W. W. Constrained diffusion or immobile fraction on cell surfaces: A new interpretation. *Biophys. J.* **1996**, 2767.

(236) Roder, F.; Waichman, S.; Paterok, D.; Schubert, R.; Richter, C.; Liedberg, B.; Piehler, J. Reconstitution of Membrane Proteins into Polymer-Supported Membranes for Probing Diffusion and Interactions by Single Molecule Techniques. *Anal. Chem.* **2011**, 6792.

(237) Braeckmans, K.; Deschout, H.; Demeester, J.; De Smedt, S. C.: Measuring Molecular Dynamics by FRAP, FCS, and SPT. In *Optical Fluorescence Microscopy*; Diaspro, A., Ed.; Springer-Verlag Berlin Heidelberg: Heidelberg, New York, 2011; pp 153-163.

(238) Klein, C.; Waharte, F.: Analysis of Molecular Mobility by Fluorescence Recovery After Photobleaching in Living Cells. In *Microscopy: Science, Technology, Applications and Education*; Mendez-Vilas, A., Diaz, J., Eds.; Formatex Research Center: Badajoz, 2010; pp 772-783.

(239) Kubitscheck, U.; Wedekind, P.; Peters, R. Lateral Diffusion Measurement at High-Spatial-Resolution by Scanning Microphotolysis in a Confocal Microscope. *Biophys. J.* **1994**, 948.

(240) Mullineaux, C.; Tobin, M.; Jones, G. Mobility of photosynthetic complexes in thylakoid membranes. *Nature* **1997**, *390*, 421-424.

(241) Robben, K. C.; Tran-Ba, K. H.; Ito, T.; Higgins, D. A. Trajectory-Profile-Guided Single Molecule Tracking for Assignment of One-Dimensional Diffusion Trajectories. *Anal. Chem.* **2014**, *86*, 10820-10827.

(242) Jackson, E. A.; Hillmyer, M. A. Nanoporous Membranes Derived from Block Copolymers: From Drug Delivery to Water Filtration. *ACS Nano* **2010**, *4*, 3548-3553.

(243) Shuang, B.; Chen, J. X.; Kisley, L.; Landes, C. F. Troika of single particle tracking programing: SNR enhancement, particle identification, and mapping. *Phys. Chem. Chem. Phys.* **2014**, *16*, 624-634.

Appendix of Dissertation

1) Equation for rotated 2D Gaussian function

In this section, Eq (1) of the main text is derived from the well-known theoretical expression for the elliptical 2D Gaussian function.[5]

$$f(x,y) = z_0 - A\exp\left(-\left(\frac{x'}{(\sqrt{2}/4)w_{//}}\right)^2 + \left(\frac{y'}{(\sqrt{2}/4)w_{\perp}}\right)^2\right) \quad (1)$$

Where x' is the major ($L_{//}$) and y' is the minor ($L_{\perp}$) axis of the elliptical Gaussian function. Other parameters shown in the equation are described in the main text.

Next, x' and y' can be analytically expressed in the Cartesian coordinates (see Scheme below) as:

$$x' = (x - x_0)\cos\theta + (y - y_0)\sin\theta \quad (2)$$

$$y' = -(x - x_0)\sin\theta + (y - y_0)\cos\theta \quad (3)$$

Where α is the angle between the x-axis (SVP-direction) and the main axis ($L_{//}$) of the elliptical Gaussian function (see scheme). Using equations (2) and (3), equation (1) can be written as

$$f(x,y) = z_0 - A\exp\left(-\left(\frac{(x - x_0)\cos\theta + (y - y_0)\sin\theta}{(\sqrt{2}/4)w_{//}}\right)^2 - \left(\frac{-(x - x_0)\sin\theta + (y - y_0)\cos\theta}{(\sqrt{2}/4)w_{\perp}}\right)^2\right) \quad (4)$$

This is equation 1 in the main text used for theoretical fitting of the fluorescence data of FRAP.

Scheme

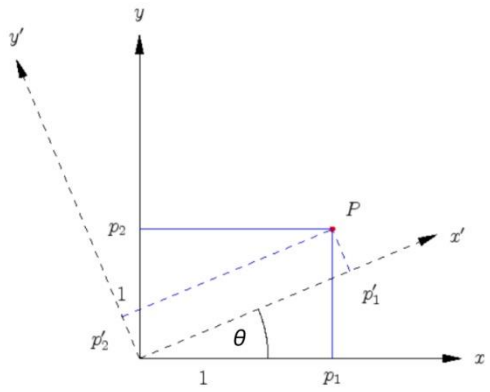

2) Matlab Codes.

Main Code

```
clc; clear all; close all;

%------------------------------ReferenceData-------------------------------------------------------------------
fID = fopen('FRAP_S3-0.raw');
I_BG = fread(fID,[64,64], 'int16=>int16', 'b');
Iread = fread(fID,[64,2*64], 'int16=>int16', 'b');
IBG=transpose(I_BG);
I1=transpose(Iread);
zRaw=double(I1);
zBG=double(IBG);
zData=zRaw./zBG;
Noise=std2(zData);

frames_no1=49;
frames_no2=9;

%-------------Experimental data, first part (< 5 mins)-----------------------------------------------------
for k = 1:frames_no1
fID = fopen('FRAP_S3.raw');
I_BG = fread(fID,[64,64], 'int16=>int16', 'b');
Iread = fread(fID,[64,(k+1)*64], 'int16=>int16', 'b');
IBG=transpose(I_BG);
I1=transpose(Iread);
I1(1:k*64,:)=[]; %delete unnecessary loaded images

%% Conversion and Normalizing
[sx,sy]=size(I1);
[X,Y]=meshgrid(1:sy,1:sx);
xData=double(X);
yData=double(Y);
zRaw=double(I1);
zBG=double(IBG);
zData=zRaw./zBG;
xyData = {xData,yData};

%% Set up the startpoint
[amp, ind] = min(zData);
[amp_row, ind_x] = min(amp);
[amp_col, ind_y] = min(zData(:, ind_x));% amp is the amplitude.
xo = 33; % guess that it is at the maximum
yo = 33; % guess that it is at the maximum
ang = 1; % angle in degrees.
sy = 5;
```

```
sx = 5;
zo = median(zData(:))-std(zData(:));
xmax = 64;
ymax = 64;
xmin = 0;
ymin = 0;

%% Set up fittype and options----------------------------------------------------------------------
LB = [0 -45 0 0 2020 0];
UB = [Inf 45 Inf Inf 4545 Inf]; % angles greater than 90 are redundant
StartPoint = [amp_col ang sx sy xo yo zo];%[amp, sx, sxy, sy, xo, yo, zo];
tols = 1e-12;
options = optimset('Algorithm','active-
set','Display','off','MaxFunEvals',1000,'MaxIter',1000,'TolX',tols,'TolFun',tols,'TolCon',tols,
'UseParallel','always', 'MaxFunEvals', 1000);

z_guess = gaussian2D(StartPoint, xyData);
slide_y=z_guess(33,:);
slide_x=z_guess(:,33);
y=1:1:64;
x=1:1:64;

%perform the fitting-----------------------------------------------------------------------------------
[fitresult,resnorm,residual,exitflag,output,lambda,jacobian] =
lsqcurvefit(@gaussian2D,StartPoint,xyData,zData,LB,UB,options);
zo_out1(k) = fitresult(1,7);
angle_out1(k) = fitresult(1,2);
fit_out = gaussian2D(fitresult,xyData);
Ampl1(k)=-min(fit_out(33,:))+zo_out1(k);

figure(4)
plot(y, fit_out(:,33), y, zData(:,33), 'or');
hold on;


results_out(k, :)=fitresult;
zData_BG(1:20,1)=zData(1:20,33);
zData_BG(21:40,1)=zData(45:64,33);
Noise_data(k)=std2(zData_BG);
End

Amplitude1=transpose(Ampl1);
Zo_out1=transpose(zo_out1);
Angle_out1=transpose(angle_out1);

%-------------Experimental data, second part (> 5 mins)-----------------------------------------------
```

```
for k = 1:frames_no2
fID2 = fopen('FRAP_S3-2.raw');
Iread2 = fread(fID2,[64,(k+1)*64], 'int16=>int16', 'b');
I2=transpose(Iread2);
I2(1:k*64,:)=[]; %delete unnecessary loaded images

%% Conversion and Normalizing
zRaw2=double(I2);
zData2=zRaw2./zBG;

% 2D Gaussian Fitting--------------------------------------------------------------------------------
[amp, ind] = min(zData);
[amp_row, ind_x] = min(amp);
[amp_col, ind_y] = min(zData(:, ind_x));% amp is the amplitude.
xo = 33; % guess that it is at the maximum
yo = 33; % guess that it is at the maximum
ang = 1; % angle in degrees.
sy = 5;
sx = 5;
zo = median(zData(:))-std(zData(:));
xmax = 64;
ymax = 64;
xmin = 0;
ymin = 0;

%Set up fittype and options-------------------------------------------------------------------------
LB = [0 -45 0 0 32 32 0];
UB = [Inf 45 Inf Inf 34 34 Inf]; % angles greater than 90 are redundant
StartPoint = [amp_col ang sx sy xo yo zo];%[amp, sx, sxy, sy, xo, yo, zo];
tols = 1e-12;
options = optimset('Algorithm','active-
set','Display','off','MaxFunEvals',1000,'MaxIter',1000,'TolX',tols,'TolFun',tols,'TolCon',tols,
'UseParallel','always', 'MaxFunEvals', 1000);

z_guess = gaussian2D(StartPoint, xyData);
slide_y=z_guess(33,:);
slide_x=z_guess(:,33);
y=1:1:64;
x=1:1:64;

%% perform the fitting--------------------------------------------------------------------------------
[fitresult,resnorm,residual,exitflag,output,lambda,jacobian] =
lsqcurvefit(@gaussian2D,StartPoint,xyData,zData2,LB,UB,options);
fit_out2 = gaussian2D(fitresult,xyData);
zo_out2(k) = fitresult(1,7);
angle_out2(k) = fitresult(1,2);
```

```
Ampl2(k)=-min(fit_out(33,:))+zo_out2(k);

figure(4)
plot(y, fit_out2(:,33), y, zData2(:,33), 'or');
hold on;

results_out2(k, :)=fitresult;
zData_BG(1:20,1)=zData(1:20,33);
zData_BG(21:40,1)=zData(45:64,33);
Noise_data2(k)=std2(zData_BG);
end

%-------------Converting all Data (pixel to length----------------------------------------------------
Amplitude2=transpose(Ampl2);
Zo_out2=transpose(zo_out2);
Angle_out2=transpose(angle_out2);

Width_x = 0.75*results_out(:,3);
Width_x2 = 0.75*results_out2(:,3);
Width_y = 0.75*results_out(:,4);
Width_y2 = 0.75*results_out2(:,4);
xWidth = transpose(Width_x);
xWidth2 = transpose(Width_x2);
yWidth = transpose(Width_y);
yWidth2 = transpose(Width_y2);
t_bin=5;
t_bin2=60;
x_data=0:t_bin:frames_no1*t_bin-5; %t_end is t_bin*k_end
x_data2=285:t_bin2:285+(frames_no2*t_bin2-60); %t_end is t_bin*k_end

y_data1=xWidth;
y_data2=xWidth2;
y_data=[y_data1, y_data2];
Y_Data=transpose(y_data);
x_data_all=[x_data, x_data2];

%-------------Data Fitting to Numerical Solution-----------------------------------------------------
D=1; %diffusion coefficient
P=800;
xo = 50;
R = 100;
%w = 10;
guess=[D P xo R];
lowerbound = [0 0 0 0];
upperbound = [10 5000 500 500];
```

```
%-------------Plot of parameters guess-----------------------------------------------------------------------
data_fit_guess = profilefit(guess, x_data_all);
dataFitGuess=transpose(data_fit_guess);
figure(6)
plot(x_data_all,y_data,'or',x_data_all,data_fit_guess,'--g');
%plot(x_data2,y_data2,'or',x_data2,data_fit_guess2,'--g');
title('Numerical fitting of FRAP data')
legend('Data','Fit (Guess)', 'location', 'southeast')
hold on;
pause

%-------------Fitting procedures-----------------------------------------------------------------------------
options=optimset('MaxIter',1000,'TolX',1e-1,'TolFun',1e-1, 'MaxFunEvals',500);
[param,resnorm,residual,exitflag,output,lambda,jacobian] =
lsqcurvefit(@profilefit,guess,x_data_all,y_data,lowerbound ,upperbound ,options);

%------------- Plot of fitting-------------------------------------------------------------------------------
Data_fit_out = profilefit(param, x_data_all);
DataFitOut=transpose(Data_fit_out);
figure(7)
plot(x_data_all,y_data,'o',x_data_all,DataFitOut,'-x')
title('Numerical fitting of FRAP data')
legend('Data','Fit','location', 'southeast')

%---------------Output of results-----------------------------------------------------------------------------
ci = nlparci(param,residual,'Jacobian',jacobian);
CI_D=ci(1,2)-param(1)
CI_P=ci(2,2)-param(2)
CI_xo=ci(3,2)-param(3)
CI_R=ci(3,2)-param(4)

fprintf('\r\rFit parameters:\r');
fprintf('\r\rD +/- 0.95-C.I. in um2/s:\r');disp(param(1));
fprintf('\r\rP +/- 0.95-C.I.:\r');disp(param(2));
fprintf('\r\rxo +/- 0.95-C.I.:\r');disp(param(3));
fprintf('\r\rR +/- 0.95-C.I.:\r');disp(param(4));
```

Code of 'profilefit' Function

```
function [width_out] = profilefit(Vars_in, x_in)

% fitting parameters%----------------------------------------------------------------------------------------

D = Vars_in(1);%diffusion coefficient in m^2/s
xo= Vars_in(3);%bleach position in um
R = Vars_in(4);%right edge of domain in um
P = Vars_in(2);% laser power W
w = 7;% width of bleach at 1/e^2 in um
t_end = max(x_in); % time scale of simulation in s
time_bin=numel(x_in);%time resolution, needs to be adjusted based on frame number!!!

%Constants of PDE-------------------------------------------------------------------------------------------
Co = 1; % concentration in uM
K = 1.5; %maximum recovery
L=2;%left edge of domain
space=R-L; %domain length in um
space_bin=500;%space resolution

% Geometric / time considerations
x = linspace(L,R,space_bin);
t = linspace(0,t_end,time_bin);
t_start=0;%starting time


% Solution of PDE with pdepe solver - First data set---------------------------------------------------
m = 0; %0 for cartesian coordinates
sol = pdepe(m,@pdex1pde,@pdex1ic,@pdex1bc,x,t);
u1 = sol(1:t_end,:,1);


[xm, ym] = meshgrid(x, t);
fxy =u1.*(P/(pi*space.^2)) ;% Probe beam is uniform not Gaussian!
fxy_norm1=-1*u1+1;

for k=1:t_end;
 [sigma_out1,mu_out1,y_norm1] = gaussfit(x,fxy_norm1(k,:));
 width_out(k)=4*sigma_out1;
 yp = 1/(sqrt(2*pi)*sigma_out1)*exp(-(x-mu_out1).^2/(2*sigma_out1.^2));
end

figure(6)
 t1 = linspace(0,t_end,t_bin);
plot (t1,width_out,'-o');
```

Code of 'gaussfit' Function

```
function [sigma_out, mu_out, y] = gaussfit( x, y, mu0, sigma0)
% adapted from  Przemyslaw Baranski, Gaussian Fit, 16. Feb. 2012, Matlab Central File
Exchange

% Maximum number of iterations
Nmax = 200;

if( length( x ) ~= length( y ))
   fprintf( 'x and y should be of equal length\n\r' );
   exit;
end

n = length( x );
x = reshape( x, n, 1 );
y = reshape( y, n, 1 );

%sort according to x
X = [x,y];
X = sortrows( X );
x = X(:,1);
y = X(:,2);

%Checking if the data is normalized
dx = diff( x );
dy = 0.5*(y(1:length(y)-1) + y(2:length(y)));
s = sum( dx .* dy );
if( s > 1 | s < 0.5 )
%fprintf( 'Data is not normalized! The pdf sums to: %f. Normalizing...\n\r', s );
   y = y ./ s;
end

X = zeros( n, 3 );
X(:,1) = 1;
X(:,2) = x;
X(:,3) = (x.*x);


% try to estimate mean mu from the location of the maximum
[ymax,index]=max(y);
mu = x(index);


%estimate sigma
sigma = 1/(sqrt(2*pi)*ymax);
```

```
if( nargin == 4 )
   sigma = sigma0;
end

if( nargin == 3 )
    mu = mu0;
end

%xp = linspace( min(x), max(x) );

% iterations
for i=1:Nmax
%yp = 1/(sqrt(2*pi)*sigma) * exp( -(xp - mu).^2 / (2*sigma^2));
%plot( x, y, 'o', xp, yp, '-' );

    dfdsigma = -1/(sqrt(2*pi)*sigma^2)*exp(-((x-mu).^2) / (2*sigma^2));
    dfdsigma = dfdsigma + 1/(sqrt(2*pi)*sigma).*exp(-((x-mu).^2) / (2*sigma^2)).*((x-
mu).^2/sigma^3);

    dfdmu = 1/(sqrt(2*pi)*sigma)*exp(-((x-mu).^2)/(2*sigma^2)).*(x-mu)/(sigma^2);

    F = [ dfdsigma dfdmu ];
    a0 = [sigma;mu];
    f0 = 1/(sqrt(2*pi)*sigma).*exp( -(x-mu).^2 /(2*sigma^2));
    a = (F'*F)^(-1)*F'*(y-f0) + a0;
    sigma = a(1);
    mu = a(2);
 sigma_out=sigma;
 mu_out=mu;

if( sigma < 0 )
        sigma = abs( sigma );
        fprintf( 'Instability detected! Rerun with initial values sigma0 and mu0! \n\r' );
        fprintf( 'Check if your data is properly scaled! p.d.f should approx. sum up to \n\r' );
return;
end
 end
 end
```

Codes of 'pdepe' Functions

```
function [c,f,s] = pdex1pde(x,t,u,DuDx);
    c = 1;
    f = D*(DuDx);
    s = 0; % no source
end

function u0 = pdex1ic(x)
   u0 = Co*exp(-K*((8*P)/(pi*w^2))*exp(-8*((x-xo)/w)^2));
end

function [pl, ql, pr, qr]= pdex1bc(xl,ul,xr,ur,t)
    pl = 0;
    ql = L; % First derivative of u is 0.
    pr = 0;
    qr = R; % First derivative of u is 0.
end
end
```

Code of 'gaussian2D' Function

```
function z = gaussian2D(par,xy)
% compute 2D gaussian
z = par(7) - par(1)*exp(-(8*((xy{1}-par(5)).*cosd(par(2))+(xy{2}-
par(6)).*sind(par(2)))./par(3)).^2-(8*(-(xy{1}-par(5)).*sind(par(2))+(xy{2}-
par(6)).*cosd(par(2)))./par(4)).^2);
end
```